

SUB-TUMOR DISTRIBUTION OF PRINT NANOPARTICLES AND ITS APPLICATION FOR NUCLEIC  
ACID DELIVERY

Luke Edgar Roode

A thesis submitted to the faculty at the University of North Carolina at Chapel Hill in partial fulfillment of the requirements for the degree of Doctor of Philosophy in the Eshelman School of Pharmacy (Molecular Pharmaceutics).

Chapel Hill  
2014

Approved by:

Ian J. Davis

Joseph DeSimone

Rudolph Juliano

Leaf Huang

Andrew Wang

© 2014  
Luke Edgar Roode  
ALL RIGHTS RESERVED

## **ABSTRACT**

Luke Edgar Roode: Sub-tumor distribution of PRINT nanoparticles and its application for nucleic acid delivery  
(Under the direction Ian Davis and Joseph DeSimone)

Nanoparticle accumulation is typically measured at the organ level. However, much basic in vitro and in vivo research points to differences in nanoparticle internalization and interaction among cell types. This is a particularly significant point when considering solid tumor drug delivery with nanoparticles where there is a significant interplay between the pathophysiology and physical forces present within the tumor, the nanoparticle itself, and the milieu of cell types present.

Unlike other nanoparticle fabrication systems, PRINT affords the exquisite ability to control size and shape of a given nanoparticle. Particles fabricated with this method are highly uniform, allowing for easy control and dissection of the interplay between nanoparticle properties and resulting effects.

Herein we describe an approach to examining the distribution of particles within the tumor. This approach accounts for 98.6% of all live cells that were dissociated from the tumor. Analysis of the particle association of the sub-populations present reveals that the nanoparticle dose administered shows dose-independent cancer cell association at high doses using 80x320nm PRINT hydrogel nanoparticles. Moreover, this maximal association seen with this approach is roughly 7%. Notably, other immune cells like macrophages and neutrophils show significant association with particles. Quantification of the mean fluorescence intensity of particle-positive cells reveals that macrophages associate with significantly more particles per cell than any other cell type, perhaps suggesting that macrophages may be a significant target of nanoparticles within the tumor. Overall, however, the data shows that cancer cells are still the main cell type of accumulation due to the fact that in this model, macrophages make up roughly 1% of the tumor.

In vivo imaging using two photon microscopy supports the flow cytometry data, with host cells showing the brightest fluorescence and Td Tomato-expressing cells showing low-level fluorescence.

Normal mouse dermis shows little diffusion of particles outside the normal vasculature suggesting that the vasculature surrounding the tumor is uniquely permeable to nanoparticles like as in the EPR effect.

Other nanoparticle factors like size and route of administration were similarly examined. Smaller nanoparticle size seemed to play a significant role in increasing cancer cell association as well as increasing the accumulation of particles to cancer cells. When administering particles intratumorally, cancer cell association was increased along with significant increases in the mean fluorescence intensity.

Combined, these results suggest a need for analysis of particle distribution and association at the cellular level.

*To the veterans of the armed services of the United States of America, past, present, and future, for  
allowing me the freedom and security to pursue my scientific pursuits*

## **ACKNOWLEDGEMENTS**

I would like to acknowledge some of the people that have helped make this possible. Firstly, to Dr. Jim Bear for being an advocate of just doing good science and allowing me to use his animal model. To Dr. Keefe Chan, Ms. Tao Bo, Dr. Stephen Jones, and Ms. Hailey Brighton for helping me with constructs, procedures, cells, reagents, injections, and their friendship, without which I would not be in a position to conduct my research. The UNC animal studies core, especially Charlene Santos and Mark Ross, without which tail vein injections would not be done and quick access to animals would not be possible. I would be remiss not to thank Dr. Greg Robbins for his instruction on the LSRII and his early flow cytometry teaching. The UNC flow cytometry core also deserves my thanks for ensuring good operation of the cytometers.

I would also like to thank my advisors for their support, especially Ian for being the first to agree to take me as a student; quite a leap of faith on his part. And I want to thank Dr. Rudy Juliano for being supportive in my transition to work for these advisors.

The great many colleagues: Ms. Cathy Fromen, Dr. Kevin Chu, Mr. Marc Kai, Dr. Jillian Perry, Ms. Tammy Shen, Ms. Ashley Johnson, Mr. Kevin Reuter, Ms. Sarah Mueller, Ms. Katie Moga, Ms. Aminah Wali, Mr. Andy McFadden, Dr. Jeremy Simon, Mr. Nick Gomez, Ms. Catherine Fahey, Ms. Mariesa Slaughter, Mr. Austin Hepperla, I thank you for making coming to lab each day not so terrible and sometimes fun.

To my friends: Mr. Trent Waugh, Dr. Neal Rasmussen, and soon-to-be Dr. Kayla Jean Knilans, without you to offer your emotional and psychological support (i.e. listening to me bitch and complain), I may have never made it through my darkest periods. Especially Kayla to whom my enduring friendship is forever guaranteed.

I also do not want to forget to thank my wife's friends: Jess, Andrew, and Eliana Capretto, Hillary Kosnac and Bret Silvis, for making me happy by making my wife happy at the sound of their voice or a few keystrokes. Hopefully the gang will have lots of fun in Pittsburgh, PA, in the years to come.

Lastly, I want to thank my family. Specifically, my brother Matt and sister-in-law Molly for their understanding and quiet support. And my in-laws, Rick & Sue Culver for accepting me into their family with open arms. I need to thank my parents, though they know not what I do and could not begin to help me, they did what they could and would do anything they could. Not least, I want to thank my 4-legged children, Maxine & Gilligan, for their unconditional love and acceptance, even though they piss me off sometimes. Eternally, I want to thank my wife; I could not have ultimately done it with your smile, support, encouragement, stern discipline, and love. You and our future are all my reasons...

## **PREFACE**

I want to implore the readers of this dissertation that only by examining problems with complimentary techniques and with an open mind can one fully comprehend the complex interactions between nanomaterials and biological systems. The more clearly understood those aspects are, the closer the field becomes to unleashing the power of nanomedicine and avoiding clinical failure.



## TABLE OF CONTENTS

ABSTRACT .....	iii
ACKNOWLEDGEMENTS .....	vi
PREFACE .....	viii
TABLE OF CONTENTS .....	ix
LIST OF FIGURES.....	xiv
LIST OF ABBREVIATIONS.....	xvi
CHAPTER I: INTRODUCTION TO NUCLEIC ACID DRUG DELIVERY AND FLOW CYTOMETRY .....	1
1.1 Nucleic acids in and gene therapy .....	1
1.11 Nucleic acids.....	1
1.12 RNAi.....	2
1.13 Nucleic Acid therapies.....	2
1.14 Barriers to nucleic acid therapy in vivo.....	3
1.15 Viral vectors for gene therapy .....	4
1.16 Non-viral methods for gene therapy .....	5
1.2 Nanoparticles .....	7

1.21 Basic information and fabrication methods.....	7
1.22 Particle Replication in Non-wetting Templates (PRINT).....	7
1.23 PRINT systems for siRNA delivery.....	8
1.3 Nanomedicine in oncology .....	9
1.31 The EPR effect and circulation time .....	9
1.32 The biodistribution of nanoparticles.....	12
1.33 Methods for measuring accumulation of particles in organs .....	13
1.4 Flow cytometry .....	14
1.5 Two photon microscopy .....	19
1.6 References.....	22
 CHAPTER II: IN VITRO ANALYSIS OF PRINT NANOPARTICLE FACTORS INFLUENCING CELL ASSOCIATION WITH EWING SARCOMA SPHEROIDS REVEALS A CHARGE AND DOSE DEPENDENCY.....	
2.1 Overview .....	33
2.2 Introduction .....	33
2.3 Experimental Methods .....	34
2.3.1 Materials.....	34
2.3.2 PRINT Nanoparticle Fabrication.....	35
2.3.3 Nanoparticle Characterization .....	36
2.3.4 PEGylation and Acetylation.....	36

2.3.5 Cells, cell culture, and particle dosing .....	37
2.3.6 Flow cytometry of spheroids.....	37
2.3.7 Imaging of spheroid growth .....	38
2.3.8 Confocal imaging .....	38
2.4 Results .....	38
2.4.1 PRINT fabrication of Hydrogels.....	38
2.4.2 Spheroid formation of Ewing Sarcoma cell lines .....	39
2.4.3 Effect of particle charge and dose .....	39
2.4.4 Confocal imaging of spheroid association .....	39
2.5 Discussion.....	40
2.6 Conclusions.....	40
2.7 References.....	45
CHAPTER III: ANALYSIS OF PRINT NANOPARTICLE DISTRIBUTION WITHIN TUMORS REVEALS A CELL TYPE, SIZE, AND ROUTE OF ADMINISTRATION DEPENDENCY .....	49
3.1 Overview .....	49
3.2 Introduction .....	49
3.3 Experimental Methods .....	50
3.3.1 Materials.....	50
3.3.2 PRINT Nanoparticle Fabrication.....	51

3.3.3 Nanoparticle Characterization .....	52
3.3.4 PEGylation and Acetylation for in vitro and in vivo studies.....	52
3.3.5 Cells, cell culture, and spheroid injections.....	53
3.3.6 Mice and Particle Injections.....	54
3.3.7 Tumor Dissociation and Flow Cytometry.....	54
3.3.8 Calculating the relative intratumoral distribution of particles by fluorescence.....	55
3.3.9 Radiation .....	56
3.3.10 Two-photon Microscopy .....	56
3.3.11 Statistics.....	56
3.4 Results .....	57
3.4.1 PRINT fabrication.....	57
3.4.2 Accumulation of particles in whole organ .....	57
3.4.3 Sub-organ Particle Accumulation by Flow Cytometry and the Effect of Dose .....	57
3.4.4 Effect of Particle Size on Association.....	59
3.4.5 Effect of Route of Administration on Association.....	60
3.4.6 In vivo two photon microscopy .....	60
3.5 Discussion.....	61
3.6 Conclusions.....	63

3.7 References.....	81
CHAPTER IV: CONCLUSIONS AND FUTURE DIRECTIONS .....	84
4.1 References.....	89

## LIST OF FIGURES

Figure 2.1 SEM and DLS characterization of 80x320nm Hydrogel nanoparticles.....	41
Figure 2.2 Demonstration of spheroid formation ability of Ewing Sarcoma cells.....	42
Figure 2.3 Association of 80x320nm Hydrogel particles by dose, charge, and cell line in spheroids.....	43
Figure 2.4 Confocal imaging of Ewing Sarcoma spheroids.....	44
Figure 3.1 SEM and DLS of 80x320nm Hydrogel particles conjugated with DOTA .....	64
Figure 3.2 Accumulation of particles in tumors as measured by <sup>64</sup> Cu radioactivity .....	65
Figure 3.3 Flow cytometry gating scheme for analysis .....	66
Figure 3.4 Resulting proportion of cell populations detected from gating scheme .....	67
Figure 3.5 Particle association as a function of dose .....	68
Figure 3.6 Mean fluorescence intensity when different particle doses are administered .....	69
Figure 3.7 Distribution of cell-associated particles as a function of particle dose.....	70
Figure 3.8 SEM of 55x70nm particles.....	71
Figure 3.9 Quantification of the particle association for differently sized particles .....	72
Figure 3.10 Mean fluorescence intensity when administering differently sized particles.....	73
Figure 3.11 Distribution of cell-associated particles as a function of particle size .....	74
Figure 3.12 Particle association as a function of route of administration .....	75
Figure 3.13 Mean fluorescence in each sub-population as a function of route of administration .....	76

Figure 3.14 Distribution of cell-associated particles as a function of route of administration .....	77
Figure 3.15 Two photon imaging of normal mouse dermis .....	78
Figure 3.16 Two photon imaging of tumors.....	79

## LIST OF ABBREVIATIONS

AEM	Amino-ethyl methacrylate
Ago2	Argonaute 2 protein
ANOVA	Analysis of variance
CFTR	Cystic fibrosis transmembrane conductance regulator
CPP	Cell penetrating peptide
DLS	Dynamic light scattering
DMEM	Dulbecco's modification of eagle's medium
DMEF-12	1:1 mixture of DMEM and Ham's F-12 media
DMF	Dimethyl formamide
DNA	Deoxyribonucleic acid
DOPC	1,2-Dioleoyl-sn-glycero-3-Phosphatidylcholine
DOTA	1,4,7,10-tetraazacyclododecane-1,4,7,10-tetraacetic acid
DOTAP	1,2 dioleoyl-3-trimethylammonium propane
dsRNA	Double-stranded ribonucleic acid
EC <sub>50</sub>	Effective concentration at which 50% of maximal effect is seen
EDTA	Ethylenediaminetetraacetic acid
EPR	Enhanced permeation and retention
ETS	V-ets avian erythroblastosis virus E26 oncogene homolog 1
EWS	Ewing Sarcoma family
FBS	Fetal bovine serum
FDA	Food and Drug administration
FLI	Friend leukemia integration 1 transcription factor
FMO	Fluorescence minus one
FSC	Forward scatter
GRAS	Generally regarded as safe
HBSS	Hank's balanced salt solution
HIV	Human immunodeficiency virus



HP4A	Hydroxy-(PEG) <sub>4</sub> acrylate
IACUC	Institutional animal care and use
IC <sub>50</sub>	Inhibitory concentration at 50% of maximal inhibition
ICP-MS	Inductively coupled plasma mass spectrometry
IgG	Immunoglobulin G
IT	Intratumoral
LCP	Lipid coated calcium phosphate
LNA	Locked nucleic acid
MFI	Mean fluorescence intensity
miRNA	micro-ribonucleic acid
mPEG5k-SCM	methoxy-polyethylene glycol 5000 dalton molecular weight
MPS	Mono-nuclear phagocyte system
mRNA	Messenger ribonucleic acid
MW	Molecular weight
NPs	Nanoparticles
nt	Nucleotide
PBS	Phosphate buffered saline
PDI	Polydispersity index
PDMS	Polydimethyl siloxane
PEG	Polyethylene glycol
PEI	Poly(ethylenimine)
PET	Polyethylene terephthalate
PFPE	Perfluoropolyether
PLGA	Poly(lactide-co-glycolide)
PMT	Photomultiplier tube
PRINT	Particle replication in non-wetting templates
PSI	Pounds per square inch
PVOH	Polyvinyl alcohol

RISC	RNA-induced silencing complex
RNA	Ribonucleic acid
RNAi	RNA interference
shRNA	Short-harpin RNA
siRNA	Silencing RNA
SSC	Side scatter
SEM	Scanning electron microscopy
ssDNA	Single-stranded DNA
ssRNA	Single-stranded RNA
TAT	Trans-activator of transcription
TCA	Tri-carboxylic acid cycle
TEA	Triethylamine
TGA	Thermogravimetric analysis
TLR	Toll-like receptor
TPO	Diphenyl (2,4,6-trimethylbenzoyl)-phosphine oxide
tRNA	Transfer RNA
UNA	Unlocked nucleic acid
UV-LED	Ultraviolet-light emitting diode
VEGF	Vascular endothelial growth factor

## **CHAPTER I: INTRODUCTION TO NUCLEIC ACID DRUG DELIVERY AND FLOW CYTOMETRY**

### **1.1 Nucleic acids in and gene therapy**

#### **1.11 Nucleic acids**

Cells are a complex mixture of macromolecules and chemicals that must all work in synchronous harmony to allow for the cell to survive and thrive. This is not done in isolation, but as part of a surrounding environment. Mammalian cells must be capable of creating new copies of themselves during mitosis, as well as adapting to external stimuli from this environment. Therefore, an instruction set must be contained within the cell's nucleus to provide the means and guidelines to do so. Nucleic acids are the chemical building blocks for the cell's instruction set. This instruction set is made of 5 types of nucleic acids: adenosine, cytosine, guanine, thymine, and uracil, which form a polymeric chain of nucleotides linked by phosphodiester bonds. Two forms of nucleic acids exist: DNA and RNA, with the difference being that a polynucleotide structure of DNA does not contain uracil, while RNA does not contain thymine. DNA is conventionally double-stranded in nature and with the discovery of the structure of DNA in 1953 by Watson and Crick[1], it was determined to form an alpha helix. This allows adenosine-thymine, or in the case of RNA adenosine-uracil, and cytosine-guanine base pairing between the strands due to hydrogen bonding between the pairs. DNA plays a critical role in mammalian cells by acting as an information storage unit due to its superior stability as compared to RNA. Due to the instability of RNA, the cell has evolved to use it as a single-stranded messenger. The "Central Dogma" asserts that DNA is transcribed into RNA. This ssRNA then moves from the nucleus of the cell into the cytoplasm. It is here where the cell's ribosomes read or translate every 3 bases, termed a codon, and uses tRNAs to connect each amino acid together to form polypeptides, proteins, and other biofunctional molecules. These biofunctional molecules perform specific roles as receptors to sense the external environment, signaling proteins to transmit those sensations, and enzymes to convert chemicals to one form to another.

### **1.12 RNAi**

Discovered in 1998 and being deemed Nobel prize worthy in 2006[2], RNAi is thought to be a holdover from early in evolution as a response to foreign nucleic acid entry into mammalian cells. Where DNA and RNA work to express genes and create macromolecules, it was found that dsRNA could prompt the opposite response by decreasing the expression level of a gene. This was demonstrated to be a sequence-specific mechanism, with the specificity coming from nucleotides 3-17 of the 5' to 3' guide strand. It is suggested that even one nucleotide difference may abolish siRNA activity, though specific design parameters are not well understood[3]. The dsRNA is clipped by Dicer into 22nt strands with a 2nt overhang at each 3' end. This guide strand is unwound from its complementary strand and loaded into the RISC complex. Ago2 then cleaves the passenger RNA strand, leaving only the guide strand, and by that action activates the RISC complex. This loaded guide strand in an activated RISC complex then finds a complimentary mRNA strand to base pair with, which is then cleaved by the RISC complex resulting in a decrease in mRNA levels and consequently, protein levels. The RNAi phenomenon works not only for foreign RNA, but also is used endogenously by the cell as a way to regulate translation of proteins via mRNA levels. When DNA is being transcribed in the nucleus, hairpins in the RNA sequence can be formed by shRNAs or miRNAs and recognized by Dicer or Drosha and processed like an siRNA, resulting in cleavage of the target mRNA[4,5].

An alternative to RNAi gene knockdown is a similar phenomenon seen with antisense oligonucleotides, first described in 1977[6]. Typically, this is ssRNA or ssDNA and is of a complimentary sequence to the target sequence. Upon reaching the cytoplasm, Watson-Crick base-pairing allows for binding between the antisense oligo and the target mRNA. Then, the mRNA is either cleaved by RNase H or the oligo acts as a steric blocker and prevents translation of the mRNA[7-9].

### **1.13 Nucleic Acid therapies**

With the ability to increase or decrease the levels of genes seemingly by just adding different types of nucleic acids to cells, nucleic acids have the promise of solving many of man's heretofore difficult-to-treat diseases. The simplest of these would be the monogenic diseases, where one gene or one certain factor is missing. Replacement or inhibition of a single gene or factor corrects the defect and cures the disease. Well-characterized examples of this are hemophilia, muscular dystrophy, cystic fibrosis

and alpha-1-antitrypsin[10,11]. In each of these diseases a single gene: factor VIII, IX, or XI, dystrophin, CFTR, or alpha-1-antitrypsin respectively, are mutated so as to be non-functional. Clinical trials using various nucleic acid delivery approaches have been described in the literature. On the other hand, polygenic diseases such as cancer, type I diabetes, multiple sclerosis, asthma, celiac disease, and heart disease, are not the result of a single causative agent. Rather, these are a composite of the influence of genetics and environment (diet, exposure, etc.) and as such are more difficult to precisely target. Nevertheless, much research has been done on these diseases using nucleic acids.

#### **1.14 Barriers to nucleic acid therapy in vivo**

However, some basic biology and properties of nucleic acids limit their application in non-culture systems (i.e. animals). Firstly, nucleic acids are by their nature very hydrophilic polymers. They contain a sugar residue along with hydrogen-bonding groups and ionizable anionic phosphate groups connecting each nucleoside to one another. This makes nucleic acids unable to penetrate the lipid bilayer found on mammalian cells. In vitro this can be overcome by complexation with cationic polymers or lipids to form poly or lipoplexes, however these complexes are not stable when diluted upon administration. Many additional barriers exist for nucleic acid delivery in vivo. Upon systemic administration, nucleic acids encounter significant amounts of nucleases in the bloodstream. Thus, the pharmacokinetic half-life of injected nucleic acids is extremely short at less than 17 minutes[12]. Since this is an enzymatic degradation reaction, chemical modification of the nucleic acid, particularly siRNA, can be taken to inhibit the degradation. These include 2'-O-methyl or 2'-fluoro modifications of the sugar base or replacement of the phosphodiester with phosphothioate linkers. Phosphorodiamidate, LNA, or UNA modifications can also be used to enhance the stability of nucleic acids[13,14]. Beyond the plasma stability issue, the next barrier encountered is the endothelial cell lining of blood vessels. Nucleic acids must either transverse these cells or pass between them through the tight junctions linking them together. Due to the hydrophilic nature of the nucleic acids mentioned previously, transcellular pathways are inefficient and thus the nucleic acids must pass paracellularly. Once to the cells of interest, once again the cell membrane presents a challenge by not allowing passive diffusion of the nucleic acid. Assuming our nucleic acid is fortunate enough to be internalized by the cell by an endocytotic mechanism, the endosome itself now presents a challenge. Endosomes are slowly acidified by a proton ATPase going from a pH of 7.4 to 6-

6.5, and with further acidification to a pH of 4.5-5. At this later stage the vesicle is referred to as a lysosome and the low pH environment there destroys most biological components due to the high acid content. Therefore, to avoid acidic destruction of our nucleic acid, it must escape the endosome. There are a variety of means to achieve endosomal escape, however, alone our nucleic acid does not have the means to do so. Once free, the nucleic acid can either be active in the cytosol as in the case of siRNA or mRNA or encounter the additional hurdle of nuclear trafficking and import as in the case of DNA. It should also be noted that nucleic acids have the ability to stimulate the immune system via activation of TLR receptors[15]. This fact can be somewhat controlled by the sequence of the siRNA, but can be of benefit or a hindrance depending on the downstream application. Hence, protection and delivery of nucleic acids is the key challenge in translating success in culture systems to animal systems.

### **1.15 Viral vectors for gene therapy**

One way of addressing the delivery challenges is to package nucleic acids into viruses. Viruses have evolved to solve many of the delivery challenges presented above. Viruses are a kind of self-assembled biological nanoparticle, with sizes ranging from 20nm to a few hundred nm[16-18]. Depending on the type, viruses protect the nucleic acid cargo with either a protein capsid and/or a lipid bilayer known as an envelope. Viruses have evolved to transcytose the endothelial cell lining, reaching cells. Once there, there are usually multiple receptors and co-receptors that bind to a given virus, allowing for efficient internalization of the virus into the cell. In the endosome, viruses have evolved elegant escape mechanisms, ranging from lipases to conformational switches of the capsid proteins to expose cationic charges. Whatever the mechanism, efficient endosomal escape of the virus allows for either depositing its nucleic acid cargo in the cytoplasm or trafficking to the nucleus. However, three main drawbacks to viral vectors exist. First, viral vectors always require nucleic acids trafficking to the nucleus resulting in slower kinetics of gene expression or knockdown. Second, viruses are not well suited to mass production. Being a biological entity, this requires humans to manipulate cells into creating, assembling, and packaging the virus. While these requirements are not insurmountable, culturing cells and purifying the virus from them can be very time consuming and labor-intensive processes not amenable to high throughput scale-up. Third and most importantly, naturally present immunity to the viruses and/or the ability to elicit high inflammatory responses and immune cell activation after administration requires that careful monitoring

be performed for signs of toxicity after administration of viral vectors[19]. These drawbacks notwithstanding, viral vectors have entered phase I and phase II trials for both therapeutic and vaccine applications[20,21]. These trials demonstrate that viral vectors can be tolerated, however, as these reports note, significant immune response to the virus is observed[22].

### **1.16 Non-viral methods for gene therapy**

Non-viral delivery systems possess the advantages of low immunogenicity, low cost and exquisite control over the composition. These come in a variety of forms and materials. These forms can be a mode of administration like the gene gun or hydrodynamic delivery or a physical carrier/protective coating such as inorganic metals, lipoplexes, polyplexes, cell penetrating peptides, or polymeric nanoparticles.

Hydrodynamic delivery of nucleic acids is a non-viral concept first reported in 1999[23]. This concept involves injecting a large volume of fluid in a short time span. This sudden rise in blood fluid volume in a sense stretches the endothelial cell barrier, creating large fenestrations. This allows naked nucleic acids or carriers in this solution to circumvent the blood and endothelial barriers. When systemically performed, most nucleic acid concentrates in the hepatocytes of the liver. However, this method is optimal at 1mL of solution per gram of animal weight; an easy enough volume to work with in a mouse, but not practical for a human. This is especially true since it has many dangerous side effects like high blood pressure, low heart rate, and possibly death. One could possibly use this technique in isolated limbs. The gene gun is another form of physical delivery that has been used successfully for plasmid DNA vaccine applications. The gene gun was originally shown to work by coating metallic particles with plasmid DNA and then propelling them into an object, specifically the skin of an animal. The large force from the shot helps the metal-DNA particles penetrate the outer layers of skin to reach the dermis. Electroporation is another physical method of gene delivery that uses a voltage potential to force the lipid molecules in the cell membrane to shift position slightly, creating nm-sized pores for large macromolecules like nucleic acids to enter the cell. However, this can lead to a large amount of cell death and damage. Ultrasound and applied magnetic fields represent gentler methods to generate reversible pores in cell membranes for gene delivery[24].

Beyond specific methods, nucleic acid carriers come in a few different forms defined by the mechanism by which they interact with the nucleic acid. Due to the many negative charges present on the

phosphodiester backbone of nucleic acids, complexes with cationic molecules are easily formed. This kind of complex based on electrostatic interactions is termed a polyplex or lipoplex, depending on whether the nucleic acid binding partner is a polymer or a lipid. The N:P ratio, that is the molar amount of cationic nitrogen groups to phosphate groups present on the nucleic acid, helps determine how tightly the poly/lipoplex binds the nucleic acid. Common lipids for this include DOTAP, PEI, and DOPC. The cationic nature of the lipids is both a blessing and curse. A blessing in the sense that this allows for tight binding of the lipid to the nucleic acid, affording protection and perhaps some compaction of the nucleic acid. A curse in the sense that enhanced binding to the nucleic acid also hinders release of the nucleic acid, resulting in a lack of available nucleic acid to elicit an effect. Moreover, the cationic groups can interact with the cell membrane, causing toxicity. PEI is notable for its toxicity, whereas DOTAP and DOPC are much less toxic[25-30]. Common polymers for the formation of polyplexes include chitosan[31], cyclodextrins[32,33], or dendrimers[34,35]. Chitosan and cyclodextrin are naturally-occurring polysaccharides that are cationic, whereas a dendrimer is a highly branched, symmetrical, synthetic polymer. These polymers all show relatively low toxicity, however they are variable in their ability to create a successful delivery vehicle. Chitosan has been shown to have poor endosomal escape of the nucleic acid, but a cyclodextrin-based polyplex has been advanced to clinical trials where it showed the first RNAi effects from systemic administration in humans[36]. An alternative to polymers and lipids are cell penetrating peptides. These are typically 10-30 amino acids in length with a stretch of cationic amino acids like lysine and arginine. The first reported discovery was the HIV-1 TAT peptide that demonstrated cell penetration and activation of the HIV-1 promoter. CPPs can either be attached to a nucleic acid chemically or form a complex directly. Both chemical attachment and electrostatic complexation have been shown to be effective in cell culture systems[37-42]. In addition to electrostatic interactions, various polymers have been used to entrap siRNA within them. For example, PLGA can effectively entrap siRNA and be used for successful pre-clinical gene therapy[43-46]. Inorganic elements can also be used to directly conjugate nucleic acids to a delivery vehicle. Colloidal gold has been used by Mirkin and others to demonstrate successful nucleic acid delivery[47]. Other heavy-metal elements such as those contained in quantum dots have demonstrated successful delivery in culture systems although concerns remain about their toxicity, similar to the literature surrounding carbon nanotubes. LCP particles use calcium to form



complexes with nucleic acids, which can then be coated with lipids. This recent development in particle composition has shown promising pre-clinical results for the delivery of nucleic acids[48,49]. In whatever form nucleic acids are interacting with a material, these mixtures generally form what is known as nanoparticles.

## **1.2 Nanoparticles**

### **1.21 Basic information and fabrication methods**

Nanoparticles can range in size from 1-10,000nm, with at least one dimension <100nm. This puts these objects in a size range similar to bacteria and viruses. These particles are invisible to the naked eye, but can be viewed with the aid of light or electron microscopes. Nanoparticle carriers can be made by various methods, but generally fall into two categories of fabrication: bottom-up and top-down. Bottom-up approaches for nanoparticle fabrication typically rely on emulsions or inverse microemulsions to direct self-assembly of spherical particles, requiring energy to create particles in the 10-100nm range[50]. These types of approaches can be used with many different materials, but also produce significant variation in particle size. In contrast, top-down fabrication approaches use patterns and templates to confer the advantage of uniform size[51]. These fabrication techniques rely on photolithography or imprint lithography, common techniques in the microelectronics industry. Photolithography involves using lasers to etch a design or cavity into a given surface. The drawback to photolithography is that fabrication of nano-scale templates requires shorter and shorter wavelengths of light (e.g. 157nm F<sub>2</sub> lasers) and thus become technically complex and expensive to operate at small particle dimensions. On the other hand, imprint lithography uses a mold containing cavities and a curable liquid to create objects on small size ranges. This approach should be more cost-effective as compared to photolithography, however, the small features created by this process are generally interconnected by “scum” layers. In the microelectronics industry, these scum layers would be dissolved with harsh chemicals or processes. Sensitive biological samples, however, would not survive such harsh treatment therefore making this approach impractical for creating nanoparticle carriers for biological cargo.

### **1.22 Particle Replication in Non-wetting Templates (PRINT)**

PRINT is a nanofabrication technique similar to imprint lithography, using a patterned mold and curable liquids[52]. However, it has a decided advantage against other forms of imprint lithography. In the

PRINT process, the mold is made of PFPE. Due to the high fluorine content, these molds have roughly half as much surface energy as other common materials molds are made of such as PDMS (12 dynes  $\text{cm}^{-1}$  vs 20 dynes  $\text{cm}^{-1}$ )[53]. Due to this property, this makes molds made of PFPE non-wetting and non-swelling. This means that the curable materials will not stick to the non-cavity portions of the mold, thereby avoiding the “scum” problem inherent to conventional imprint lithography. The cavities can be filled through capillary action or melt filling, depending on the material used for fabricating the particles. Once filled, the mold can be laminated to a sacrificial harvesting layer. The harvesting layer is then dissolved, leaving free particles in solution. This approach allows for monodisperse nanoparticles, made in a scalable fashion, giving PRINT a decisive advantage over other forms of nanoparticle manufacture. Moreover, this process is amenable to sensitive biological cargoes such as protein and nucleic acids[52,54].

### **1.23 PRINT systems for siRNA delivery**

The first reported use of nucleic acids in PRINT was using siRNA duplexes and the material PLGA[55]. PLGA is a co-polymer composed of lactide and glycolide. Both lactide and glycolide are considered GRAS by the FDA due to their use as excipients in numerous pharmaceutical products and the fact that they are components of the TCA cycle and would thus be broken down naturally by the body. The FDA accepted nature of a degradable particle is attractive when designing a particle delivery system for future translational use. When using a luciferase-expressing HeLa cell line, it was found that cationic lipid-coated 80x320nm PLGA particles had comparable  $\text{IC}_{50}$  knockdown values as lipofectamine, with minimal toxicity of the particles seen. Moreover, the loading of the particles was influenced by the molecular weight and lactide: glycolide ratio of the PLGA, with shorter, higher lactide-containing PLGA resulting in higher loading of siRNA.

A separate particle matrix was also tested for its ability to carry siRNA. This matrix was a hydrogel particle composed of hydroxy-PEG acrylate, PEG diacrylate to crosslink the acrylate monomers, and amino-ethylmethacrylate to provide a functional handle for amine surface chemistry. The acrylate groups are then photopolymerized to create a covalently crosslinked particle. Due to the covalent bonds present these particles show very slow degradation. This resistance to degradation gives the advantage of preventing premature release of the siRNA. At first, siRNA was simply complexed to the 200x200nm

particles via electrostatic interactions. However, in salt solutions and other biological fluids, significant siRNA release was observed. This release problem led to the creation of a conjugated siRNA approach where siRNA was conjugated to an acrylate group through a disulfide bond[56]. The thinking here was that the disulfide bond would be stable in biological fluids until entering the endosome. Upon entry into the endosome, the reducing environment in the endosome would cause release of the siRNA. Good in vitro knockdown in luciferase-expressing HeLa cells was observed with a maximum  $EC_{50}$  of 15.1nM. However, these particles were fabricated with 50wt% of AEM and showed significant toxicity. The amount of AEM contained in these particles could be reduced to 30wt% AEM without loss of knockdown efficiency. Lower amounts of AEM could be used, such as 20wt%, but the  $EC_{50}$  increased to 69.4nM.

In vivo results have not been published to date for either the PLGA or Hydrogel matrix, but are an area of active investigation.

### **1.3 Nanomedicine in oncology**

#### **1.31 The EPR effect and circulation time**

Nanoparticle applications in oncology typically focus on systemic injection of particles for the treatment of solid tumors. The prevailing wisdom is that once tumors reach a critical size, the blood vessels originally supplying the tumor can no longer support all the cells present. Once some of the cells start to die, angiogenic factors such as VEGF are secreted[57]. This stimulates the formation of new blood vessels. However, proper blood vessel formation requires the correct balance of growth factors. Due to the imbalance of factors, the newly forming blood vessels seem to have large fenestrations present[58,59]. The size of these fenestrations is dependent upon the tumor type, location, and microenvironment, estimated to be between 200-2000nm[60,61]. And while there is residual lymphatic draining and a little neolymphangiogenesis, it is thought that the bulk of the tumor has an overall lack of lymphatic drainage[62]. This creates a situation where macromolecular species such as proteins, antibodies, and nanoparticles penetrate the endothelial barrier through the fenestrations, but are then trapped there by a lack of convective forces to carry it back to the bloodstream. This effect is dependent upon the size of the macromolecule as objects 4-5nm in hydrodynamic radius can diffuse easily back to circulation[63]. Thus, an object between 5nm and the size of the endothelial fenestrations can be effectively trapped between blood vessels and cancer cells. This so-called EPR effect, discovered by Matsumura & Maeda in the

1986, is the main justification for the application of nanomedicines for cancer drug delivery[64]. In their experiments,  $^{51}\text{Cr}$  was used to radiolabel 6 different proteins ranging in molecular weight from 12,000-150,000. Due to the radiolabeling, the authors were able to track the blood pharmacokinetics and tissue accumulation of the proteins over time in outbred ddY mice bearing sarcoma 180 tumors on their backs. Albumin and IgG had very long half-lives of about 35 hours and also had the greatest amount of accumulation in tumors at around 7.5% of the injected dose. From the other proteins injected, a rough correlation between circulation time and accumulation was found. Hence, the EPR effect postulates that the longer a macromolecule can circulate, the greater accumulation within a tumor it will have. This reasoning has led to a focus on two things: increasing the circulation time of particles following systemic administration and thusly increasing the accumulation of nanoparticles in tumors.

It should be noted that while the EPR effect has seemingly been demonstrated in animal models, there is inconclusive evidence that the EPR effect exists in humans. During the evaluation of liposomal doxorubicin (Doxil), doxorubicin concentrations were measured in tumor biopsies directly or the tumors were imaged using radionuclide labeled liposomes. The general results were that in 3-7 days a 4-16-fold higher concentrations of doxorubicin or particle were seen in the tumor as compared to the blood[65,66]. This was postulated as evidence of the EPR effect, however, the half-life of doxorubicin and doxil are strikingly different at 10.5 vs 45.9 hours. This confounds the experiment and results in an unclear conclusion. Review of the available literature suggests that only sarcomas show a tumor: surrounding tissue/blood signal greater than 1, indicating preferential accumulation. Brain metastases, bone metastases, glioblastomas, breast, lung, and ovarian cancers show a ratio less than 1[65-70]. However, these are quantitated by a mixture of methodologies, all of them less optimal than the approaches that have been performed in pre-clinical studies (i.e. organ harvest and direct quantitation). There is also a lack of efficacy data to evaluate the relationship between accumulation and efficacy. Moreover, the majority of current clinical data is with liposomes, specifically Doxil. It is therefore unknown what effects particle properties like size, shape, or drug release kinetics may have on accumulation or therapeutic effect. It must also be noted that patients able to be enrolled in phase I clinical oncology studies are most likely refractory to standard of care therapy, usually various chemotherapies. These patients may represent a sub-set of difficult to treat patients or the environment of the tumor may have changed

substantially following treatment. It is therefore difficult to determine whether the animal models are of predictive value except by efficacious outcome and there is seemingly little predictive value of the clinical utility and outcome in humans when using the typical xenograft mouse model[71-73].

Circulation time of nanoparticles was thought to be a function of non-specific protein adsorption on the surface of the particle, leading to internalization by resident macrophages in the liver and spleen. However, recent work by Jones, et. al. used intravital microscopy to examine the circulation time of various PRINT Hydrogel particles[74]. In the course of this work, it was discovered that monocytes and neutrophils in the bloodstream are primarily responsible for circulating particle clearance. Moreover, the background strain of mice used also significantly influenced the resulting circulation time of the particles. It was found that more Th1-prone strains such as C57BL/6 and B10D2 had longer particle circulation time as compared to more Th2-prone strains such as BALB/c and DBA2. This was hypothesized to be due to differences in macrophage polarization, with Th1 biased towards M1 macrophages and Th2 biased towards M2 macrophages. M1 macrophages are thought to be more inflammatory and active in the destruction of pathogens, whereas M2 macrophages are thought to be more anti-inflammatory[75]. Paradoxically, M2 macrophages are also thought to have greater rates of endocytosis due to enhanced expression of scavenger and lectin receptors[76]. Previous work had implicated various receptors such as the scavenger receptor, Fc receptors, and complement, based on in vitro studies using cultured cell lines[77-79].

Particle internalization by cells of the MPS system can be discouraged by having the surface of the particle be hydrophilic. This is most commonly accomplished by making “stealth” particles by the attachment of a PEG polymer on the surface of the particle (PEGylation). Quantification of the amount of PEGylation on particles needed to significantly extend circulation time has been shown to be 0.1 PEG/nm<sup>2</sup>[80]. This quantification ensures that  $R_f/D > 1$ , where  $R_f$  is the Flory radius, and  $D$  is the distance between the PEG polymers attached at the particle surface. The Flory radius is calculated as  $R_f = 3/5 \cdot n \alpha$  where  $\alpha$  is the length of the monomer unit in angstroms (equal to 3.5 Å for PEG) and  $n$  is the number of repeat units of the monomer (equal to 50 for PEG of 2k MW). When  $R_f/D > 1$  it is thought that PEG is in a “brush” conformation where each polymer chain is extended from the surface of the nanoparticle. This provides the benefit of inhibiting MPS cell internalization, thereby extending circulation time[81]. Maximal

benefits of a reduction in MPS cell internalization and extension of circulation time is seen at  $R_f/D > 2$ , a state termed a “dense brush” of PEGylation[82]. When  $R_f/D < 1$ , PEG is thought to adopt a “mushroom” conformation where the PEG is not extended, but collapsed to the surface of the particle. When this occurs, no benefit in preventing MPS internalization and circulation time extension time is seen[81]. A recent study by Yang et. al. demonstrated with in vitro assays for MPS cell uptake and circulation time screening by intravital microscopy that polystyrene particles required an  $R_f/D > 2.8$ , or 1 PEG/nm<sup>2</sup>, to show any reduction in cell internalization and extension of circulation time[83]. Whether this discrepancy in the requirement for PEG density can be attributed to the particle size, particle matrix, or attachment chemistries is unclear.

### **1.32 The biodistribution of nanoparticles**

Upon systemic injection of nanoparticles, there are four possible routes for elimination. The first is filtration by the kidneys. This only applies for nanoparticles <20nm in size and does not seem to be affected by the type of material the particle is made of[84,85]. The second route of elimination is filtration by the lungs. Converse to the kidneys, the lungs will only entrap larger, micron-sized particles as the small blood vessels used to collect oxygen from the air are not large enough to allow free flow of larger particles. Unlike the kidney, aggregation of particles here leads directly to catastrophic event: asphyxiation of an animal. Thus, aggregation of particles and high accumulation in lung is a serious issue. The bloodstream represents a third possible route of elimination. Nanoparticle internalization by monocytes, neutrophils, dendritic cells, and other leukocytes present within the blood stream[74,86-88] represents a major factor in circulation time of the particles. Other cells present in the bloodstream, such as red blood cells and platelets may also play a role in interacting with the particles, but only serve as effectors to cause toxicity or uptake by the previously mentioned cell types. The fourth possible route of elimination is by resident phagocytic cells present within tissue. In practice, this refers to the specialized macrophage cells present in the liver, the Kupffer cells, and the high concentration of B cells present within the spleen[89,90].

Generally, the major organs of particle accumulation are the spleen and liver, usually with 20-40% of the injected dose present in each organ[91-93]. This is thought to be due to particle internalization by the Kupffer cells of the liver and a combined cell/mechanical clearance by the spleen. This balance

somewhat shifts to favor splenic accumulation, depending on the circulation time of the particle with longer-circulating particles showing greater spleen accumulation[94]. All other organs generally contain only a small fraction (<5%) of the injected dose. Tumor accumulation of particles has ranged from 1-15%, depending on the particle size, material, deformability, stability, surface charge, degree of PEGylation, dose administered, and the animal model used.

### **1.33 Methods for measuring accumulation of particles in organs**

Methods for calculating the percent injected dose can vary in the details, but fall into 3 main detection methods: radionuclides, metals & inductively coupled plasma mass spectrometry, and fluorescence. This is compounded by one of two main data collection methods: either whole body imaging or by individual organ collection.

Radionuclides come in a large variety of properties. The half-life of the radioactivity may be short like the 2 hours of  $^{18}\text{F}$  or longer such as 13 hours using  $^{64}\text{Cu}$ , 2.8 days using  $^{111}\text{In}$ , or 4.2 days like  $^{124}\text{I}$ . Some are best used for PET imaging such as  $^{18}\text{F}$  and  $^{64}\text{Cu}$ , whereas others offer economical benefits for the budget-conscious researcher like  $^{111}\text{In}$ . Various forms of radioactivity exist like alpha, beta, and gamma emissions and the specific radioactive particle measured is specific to the decay of each radionuclide. In any case, the main benefit of using of radionuclides is the extremely sensitive detection and quantitation limits possible when using radioactivity[95,96]. However, the obvious limitation of radionuclides is the extreme caution and hazard when using a silent killer such as radioactivity.

Inductively coupled plasma mass spectrometry creates droplets of a liquid solution and introduces it to argon plasma, heating with a plasma torch. By mixing the plasma with liquid droplets, this creates a gas that is consequently ionized. These ions can then be focused and analyzed on a mass spectrometer. In this way, elemental analysis on a sample can be performed. By using a standard curve it is possible to quantitate the actual amount present in a given sample. With a sensitivity in parts per trillion and a working range of 9 orders of magnitude, this technique can be easily and highly quantitative[97]. It is also much safer than using radionuclides. However, unlike radionuclides, it is only highly quantitative when using something with low background in biological samples such as rare metals. Often, this technique is used to quantitate the amount of Cu, Fe, Pt, or other rare metals[98]. Applying this technique in the context of nanoparticle distribution usually requires that the particle be loaded with a specific metal

or created entirely out of it[99]. Moreover, this is only useful in the context of harvesting individual organs and cannot be used for imaging.

Fluorescence on the other hand is a safe method that allows for detection of nanoparticles either with whole-animal imaging or individual organs. This comes from a chemical, a “fluorochrome”, that absorbs a particular wavelength or range of wavelengths of light. This wavelength excites an electron found in that fluorochrome to a higher energy state. Once the electron falls back to its ground state, the energy given off is in the form of photons. Depending on how large of a difference there is between the excited and ground state, this will determine the energy and thus, the wavelength of the photons given off. Fluorochromes exist across the entire UV, visible and near-IR electromagnetic spectrum. Near-IR dyes are exquisitely useful for whole-animal imaging because of the natural autofluorescence of biological tissue in the green and yellow/orange spectrums of visible light. This occurs because of various flavin and porphyrin chemicals found within the cells. In addition, elastin, collagen, and lipofuscin also add to autofluorescence found in tissues[100,101]. Each tissue will have its own particular amount of autofluorescence due to the slight variances in the amount of autofluorescent chemicals and proteins present[102]. This method is sensitive, though not nearly as sensitive as radionuclides or ICP-MS. However, this method is also amenable to sectioning and visualization of the tissue itself to examine microscopic architecture[103,104], giving it an advantage over the other two main forms of detection.

#### **1.4 Flow cytometry**

Flow cytometry is essentially a way of analyzing a sample at the level of an individual cell. It requires the blending of fluidics, light/optics, photodetectors and filters, and computers to correlate and process the light-based signals into visually pleasing formats. In essence, single cells flow past a light source such as a laser, the cells are thus stimulated to scatter and emit light (fluorescence) which is captured by photodetectors/multipliers at various wavelengths determined by the optical filters. The beauty of this is that each cell may have a specific fluorescence pattern. With computers it is possible to record and organize each individual cell's fluorescent pattern, allowing for complex analyses of cells to take place using fluorescent marking methods such as fluorescently-conjugated antibodies.

It is acknowledged that the first prototype was described in 1934 by Andrew Moldavan[105]. More or less, it was a microscope with a capillary tube across the light source such that cells were illuminated



as they passed through the light source. A photodetector attached to where the eye piece of a microscope would normally be then captured the light. Some follow up work by Coulter, Kametsky and Melamed, and others[106-109], provided a basis for which the modern cytometer design was implemented from the work of Fulwyler, Dittrich and Göhde, Van Dilla, and Herzenberg[110-112].

Due to the requirement for single cell suspensions, at first only blood cells were analyzed with this technique as there was no need for manipulation of the cells[113]. This has expanded from blood to tissue with the aid of enzymes and physical methods to dissociate the cells from the interconnected, complex mixture of cells that make up tissue, and other types of cells such as bacteria[114], sperm[115], and plankton[116]. In a sense, anything can be run on a flow cytometer so long as it meets the basic technical requirements that it can be run in a narrow stream of fluid and is between 1-30 $\mu$ m in size. However, those boundaries are being pushed as cytometers have been demonstrated to be capable of analyzing latex beads[117], cell nuclei[118], chromosomes[119], DNA fragments[120], viruses[121], and micron-sized nanoparticles[122]. These can be scanned at a rapid rate by the cytometer, approaching 100-5,000 events per second. The limiting factor in analysis speed is ensuring that single cells are flowed past the light source. This is accomplished by either confining cells to a narrow, optically clear chamber or through the beam of a nozzle with a small hole. Due to the confined nature of this passage it is critical that large aggregates or chunks not be present in solution. Many a cytometer and experiment have been broken by something as simple as a clogged cytometer. Also, to prevent once individual cells from clogging, cytometers have evolved to injecting the cell suspension into the center of wide, quickly flowing stream (the sheath fluid). In a sense, hydrodynamic properties ensure this design creates the laminar flow seen by blood vessels where most objects are confined to the middle of the stream (hydrodynamic focusing). Due to these same hydrodynamic properties, the flow rate will directly impact how wide a stream the cells are confined to.

Cells naturally both scatter and emit light. In modern cytometers, lasers are used to stimulate cells due to the narrow, intense beams of light that lasers emit. Currently, these lasers are usually gas lasers such as argon ion, helium-neon, krypton ion or solid-state lasers such as a diode. Each laser has a specific wavelength of light that is emitted by the laser. This allows for specific stimulation of various chemicals or residues of certain proteins known as fluorochromes. Ideally a fluorochrome is only

stimulated at maximum intensity at precisely one wavelength. In reality, a fluorochrome is stimulated at different intensities over a range of wavelengths. This stimulation is represented by electrons from a molecule excited to a higher orbital. When the electrons fall back to a ground state, longer wavelength light is emitted. (e.g. stimulation with 488nm light may allow for emission of >500nm light) Similar to absorption, emission also occurs at different intensities over a range of wavelengths.

In modern cytometers, cells are passed through a 488nm laser and 488nm light is scattered in both a “forward” and “side” direction. “Forward” meaning along the path of the laser and “side” meaning orthogonal to the laser (along the path the cell is traveling). Collection of the “forward scatter” (FSC) light is colloquially taken as a reference to the volume or size of a cell passing through. In reality, it is a little more complex as it is a measure of the 3-dimensional angles at which light has been refracted by an object. Objects (cells) with a larger cross sectional area will give larger FSC values. However, a similarly large object with a refractory index similar to the medium the objects are in (e.g. dead cells) will give a seemingly smaller FSC. “Side scatter” (SSC) light will be refracted by irregularities or texture on the surface or in the cytoplasm of the cell, colloquially referred to as cell “granularity”. In this way, cell types and live/dead status can be differentiated with these measurements. For example, granulocytes with irregular nuclei will have higher SSC than lymphocytes and their spherical nuclei. The velocity of the cells through a cytometer can approach 5-50 m/s, meaning that cells will only spend roughly 0.2-4  $\mu$ s in the laser beam. Since fluorochromes absorb and emit light on the nanoseconds time scale, basic division suggests that absorb and emit 100-1000 times while in the laser.

Fluorochromes, as discussed previously, require specific excitation laser and emit as specific wavelengths. Cells have natural fluorescence, termed “autofluorescence”. This can come from pyridine or flavin-type molecules present in mammalian cells or chlorophyll present in plant cells. Moreover, this can be worsened with the use of various cell fixatives such as formaldehyde, which crosslink proteins through amine groups particularly lysine residues. Beyond autofluorescence, most applications of cytometry seek to quantify or detect various markers, usually proteins. These markers can be on the surface or intracellular. Typically, an antibody, either directly conjugated to a fluorophore or not, is added to the cell suspension and incubated for some time, usually 30-60 minutes on ice. After that time, the cells are washed and if a directly conjugated antibody is not used, a secondary antibody that is directly conjugated

is used to detect the first antibody. For intracellular antigens, gentle detergents such as saponin are used to allow for antibody penetration into the cell without destroying the membrane.

However the fluorochromes are detected on or in a cell, the emission of these fluorochromes are detected in a similar manner as the SSC. While passing through a given laser, orthogonal emission of fluorochromes, like the scatter from SSC, are directed towards various dichroic mirrors. These mirrors reflect a given range of wavelengths of light and let all others pass through them. In this manner, a series of dichroic mirrors can serve to partition the emitted light. From there, filters specifically aligned with the light coming from the dichroic mirrors narrow the specific wavelengths of light further. After this process, the filtered light is detected by photomultiplier tubes (PMT). This example system contains only 1 laser, but more than 1 laser is ideal due to the plethora of fluorochromes that are available today and the various excitation wavelengths needed. For multiple lasers, the cells will pass by each laser individually, with the time between each laser on the  $\mu\text{s}$  time scale.

Practically speaking, a massless, chargeless photon of light strikes the photomultiplier tube. The photoelectric effect is then harnessed so that the photon creates a current by transferring its energy to the electrons in the PMT. The electrons move to a cathode thereby creating a current. This current is then converted into a voltage. This voltage can be amplified either linearly or logarithmically. Other conversions may be done to these values (e.g. compensation). This signal is then converted into a digital signal and reported on 1,024 channel (10-bit) scale. Signals are typically “binned” to fit into one of the channels. Logarithmic amplification can thus detect a larger range of fluorescent signal as the log amplified voltage is binned onto the 10-bit scale, allowing for greater discrimination between relative fluorescent intensities. Newer flow cytometers automatically convert the voltage into a digital signal and then amplify and process the signal. The immediate digitization of the voltage values increases the speed of the signal processing and removes the need for logarithmic amplification, avoiding the non-linearity of logarithmic amplification.

The signal detected from an individual cell will have a beginning (as it first passes into the laser) and an end (as it finishes passing through the laser), and an intensity over time. This can be integrated into a simple area measurement or simplified as a “height” (the highest amount of intensity recorded).

Some cytometers also have the ability to record the signal detected 10 million times a second, with those readings averaged to give the area or “height” measurements.

The signal detected from a cell will also vary with the abundance of fluorochrome there. The abundance of fluorochrome present, aka the fluorescence intensity or “brightness” will be a function of both the amount of thing being detected and the inherent “brightness” of the fluorochrome, as in the inherent intensity of light emitted from a fluorochrome. Some antigens are more highly expressed than others (e.g. CD45 vs. CD31 on leukocytes), which can vary for a given cell type, and certain fluorochromes are very bright (e.g. Phycoerytherin and Allophycocanin) and some are very dim (e.g. Pacific Blue).

These factors don’t play much of a role when analyzing single color fluorescence by flow cytometry. However, when multiple colors are used, this may become an important issue. This is because of two things: 1) In a sense, photomultipliers are “dumb” in that it detects whatever photons come near it. If you’re using more than one fluorochrome (fluorochrome A and B), 2) reality dictates that fluorochromes emit across a range of wavelengths as discussed previously. This wouldn’t be a problem except that if a cytometer has the appropriate filters linked to PMTs the emission from both fluorochrome A and B will be detected by the same PMT. This means that fluorescence will be detected and unable to be attributed to an individual color. Not to fear, math to the rescue! One can “compensate” for this by measuring the emission from each fluorochrome individually and detecting the ratio of the detected light in that PMT attributable to each color. Then the fluorochrome emission that is undesirably detected by a given PMT can be “subtracted” to give a truer level of the fluorescence emission. This is obviously more mathematically complex than conceptually described herein, involving linear algebra and other higher mathematical operations, but is essentially what the software on the computer is doing “behind the curtain” without the user being obvious to its doings. The drawback to using this mathematical normalization is that usually “spreading” is observed for cells that are compensated and have significant spillover/interaction from the fluorochrome[123,124]. Fluorescence measurements and detection on cytometers generally have a probabilistic nature to them. Due to this, the observed spillover will also have a stochastic nature to it. In a sense, some cells will show spillover and some won’t. Hence, when the mathematical “subtraction” is applied, the ones without spillover look negative, making the population as a

whole seem to be more variable than it really is. This is referred to as “spreading”. The best course of action is to use combinations of fluorophores that do not have “spillover” and other compensation issues. In certain cases this is unavoidable, but best practice dictates that this be minimized.

Most modern flow cytometry data can be easily manipulated with software used to perform all calculations. This allows for visual display of the data and quantification of the relative fluorescence. Data can be represented as single fluorescence histograms or fluorescence vs fluorescence plots for more in-depth analysis.

Another feature of flow cytometry software is the “gating” that can be done with the software. This is a term used for selecting a group of cells and sub-analyzing only that population (e.g. fluorescence of other colors, FSC, SSC, etc.). Gating can be a useful tool for cleanly analyzing sub-populations of cells present in a mixture of cell types (e.g. different cell types within a tumor).

Flow cytometry is a powerful technique to analyze single cells. With any technique there are benefits and drawbacks. Correct application of flow cytometry can assist in analyzing therapeutics at a molecular level in complex cell mixtures (i.e. in vivo).

### **1.5 Two photon microscopy**

In fluorescence microscopy, one photon of light is absorbed by a fluorophore causing excitation of the electrons. This excited state is unstable, lasting only  $10^{-8}$ - $10^{-9}$  seconds, and when the electrons return to their natural lower energy state, one photon of lower energy (longer wavelength) fluorescence is emitted[125]. Thus, fluorescence has traditionally been a linear process as if the power of excitation increases equally so does the emission.

In two photon microscopy, a non-linear absorption occurs whereby two photons of light are absorbed in a similar time frame (less than  $10^{-18}$  seconds) to generate a fluorescent photon[125]. These photons are of roughly half the energy needed for traditional fluorescence excitation, however, due to quantum mechanics, the actual excitation wavelengths/spectra will vary slightly from this theoretical value. The emitting photons, however, behave as expected and show an emission spectra exactly as if excited by linear microscopy.

In her 1931 doctoral dissertation, Maria Göppert-Mayer predicted the possibility of two-photon absorption[126]. However, the simultaneous absorption of two low energy photons is a rare event,

requiring a high flux of photons of  $10^{20}$ - $10^{30}$  photons/(cm<sup>2</sup>s ). This presented a technical challenge as most available arc lamps and other light sources were not able to generate the high flux required without simultaneously destroying the sample. It was not until the development of the subpicosecond ( $10^{-12}$ s) pulse mode-locked laser and its demonstration of practical applicability in 1990[127]. This laser is able to generate ultrashort femtosecond ( $10^{-15}$ s) pulses every nanosecond. Thus, a low average power can be used as the laser is not active 10,000 times more than it is active. In essence, the laser allows photons to be compressed in small units of time. A high numerical aperture allows for compression of the laser pulse into a small space, thus a coupling of the mode-locked laser and the appropriate aperture generates an extremely high photon flux in a small area, drastically increasing the probability of a two-photon excitation event.

The probability of an excitation event is related to the square of the instantaneous laser intensity (Probability  $\propto$  Intensity<sup>2</sup>). Due to this relationship, two photon excitation decreases dramatically away from the focal point. Thus, there is a lack of fluorescent photon emission that is out-of-focus, making two photon microscopy an inherently confocal-type of system not requiring a pinhole to filter out extraneous fluorescence as in linear confocal fluorescent microscopy. The pinhole needed in linear confocal microscopy also filters out a percentage of in-focus fluorescent photons. The deeper into a specimen imaging takes place, a greater percentage of photons filtered out would be in-focus fluorescent photons, creating an imaging depth limit to conventional linear microscopy of about 100 $\mu$ m. Thus, two photon microscopy has a superior imaging depth as compared to linear confocal microscopy ranging up to 1mm in ideal conditions, but roughly 6-fold better in most practical circumstances[128]. This is also aided by the fact that in biological samples, the longer wavelengths used by two photon imaging are less absorbed and affected by scattering as compared to conventional confocal microscopy.

From a theoretical perspective, the spatial resolution of two photon microscopy should be roughly half that as compared to linear confocal microscopy. Practically speaking, the only way to increase resolution can only be increased by increasing signal, requiring that linear confocal systems increase the pinhole size, resulting in more out-of-focus detection and thereby lowering resolution. Thus, in a practical setting the spatial resolution of two photon microscopy is nearly identical to linear confocal microscopy[125].

One secondary benefit to two photon imaging is the second harmonic generation that occurs. This phenomenon is different than true two photon absorption as it is based on scattering rather than absorption of photons. When scattered, the photons combine to form photons roughly twice the energy of the incident photons. Generation of secondary harmonics requires that molecules lack inversion symmetry and are spatially ordered. Biologically, ordered structures like collagen fibers or microtubules create this phenomenon[129]. Thus, two photon imaging can incidentally also image collagen fibers while simultaneously causing fluorescence emission of a desired fluorophore.

Two photon microscopy has two main drawbacks at this time: cost and accelerated photobleaching. Photobleaching in confocal microscopy has a somewhat linear relationship with the excitation power. In two photon microscopy, photobleaching is accelerated as more photobleaching pathways are activated in addition to the observed higher order photobleaching. Though this only occurs in the focal plane, thinner samples ( $<10\mu\text{m}$ ) are more prone to this issue[130,131].

In sum, the use and application of two photon microscopy is gaining in widespread use. It has great potential and capabilities for in vivo imaging. The depth, resolution, inherent confocal nature, and automatic imaging of extracellular structures makes two photon microscopy extremely useful for understanding in vivo biology.

## 1.6 REFERENCES

1. Watson JD, Crick FH (1953) Molecular structure of nucleic acids; a structure for deoxyribose nucleic acid. *Nature* 171: 737-738.
2. Fire A, Xu S, Montgomery MK, Kostas SA, Driver SE, et al. (1998) Potent and specific genetic interference by double-stranded RNA in *Caenorhabditis elegans*. *Nature* 391: 806-811.
3. Chalk AM, Sonnhammer EL (2008) siRNA specificity searching incorporating mismatch tolerance data. *Bioinformatics* 24: 1316-1317.
4. Dalmay T (2013) Mechanism of miRNA-mediated repression of mRNA translation. *Essays Biochem* 54: 29-38.
5. Edeleva EV, Shcherbata HR (2013) Stress-induced ECM alteration modulates cellular microRNAs that feedback to readjust the extracellular environment and cell behavior. *Front Genet* 4: 305.
6. Paterson BM, Roberts BE, Kuff EL (1977) Structural gene identification and mapping by DNA-mRNA hybrid-arrested cell-free translation. *Proc Natl Acad Sci U S A* 74: 4370-4374.
7. Lennox KA, Behlke MA (2011) Chemical modification and design of anti-miRNA oligonucleotides. *Gene Ther* 18: 1111-1120.
8. Lapidot M, Pilpel Y (2006) Genome-wide natural antisense transcription: coupling its regulation to its different regulatory mechanisms. *EMBO Rep* 7: 1216-1222.
9. Dias N, Stein CA (2002) Antisense oligonucleotides: basic concepts and mechanisms. *Mol Cancer Ther* 1: 347-355.
10. Flotte TR, Trapnell BC, Humphries M, Carey B, Calcedo R, et al. (2011) Phase 2 clinical trial of a recombinant adeno-associated viral vector expressing alpha1-antitrypsin: interim results. *Hum Gene Ther* 22: 1239-1247.
11. Flanigan KM, Voit T, Rosales XQ, Servais L, Kraus JE, et al. (2014) Pharmacokinetics and safety of single doses of drisapersen in non-ambulant subjects with Duchenne muscular dystrophy: results of a double-blind randomized clinical trial. *Neuromuscul Disord* 24: 16-24.
12. McMahon BM, Mays D, Lipsky J, Stewart JA, Fauq A, et al. (2002) Pharmacokinetics and tissue distribution of a peptide nucleic acid after intravenous administration. *Antisense Nucleic Acid Drug Dev* 12: 65-70.



13. Kim BH (2005) Chemical modification from nucleosides to nucleic acid systems. *Nucleic Acids Symp Ser (Oxf)*: 13-14.
14. Sproat BS (1993) Chemical nucleic acid synthesis, modification and labelling. *Curr Opin Biotechnol* 4: 20-28.
15. Lin Y, Zhang L, Cai AX, Lee M, Zhang W, et al. (2011) Effective posttransplant antitumor immunity is associated with TLR-stimulating nucleic acid-immunoglobulin complexes in humans. *J Clin Invest* 121: 1574-1584.
16. Park K (2010) Safe and efficient gene delivery by hybrid polymer-virus vectors. *J Control Release* 144: 1.
17. Ramsey JD, Vu HN, Pack DW (2010) A top-down approach for construction of hybrid polymer-virus gene delivery vectors. *J Control Release* 144: 39-45.
18. Boeckle S, Wagner E (2006) Optimizing targeted gene delivery: chemical modification of viral vectors and synthesis of artificial virus vector systems. *AAPS J* 8: E731-742.
19. Morse MA, Chaudhry A, Gabitzsch ES, Hobeika AC, Osada T, et al. (2013) Novel adenoviral vector induces T-cell responses despite anti-adenoviral neutralizing antibodies in colorectal cancer patients. *Cancer Immunol Immunother* 62: 1293-1301.
20. Kalams SA, Parker SD, Elizaga M, Metch B, Edupuganti S, et al. (2013) Safety and comparative immunogenicity of an HIV-1 DNA vaccine in combination with plasmid interleukin 12 and impact of intramuscular electroporation for delivery. *J Infect Dis* 208: 818-829.
21. Hooper JW, Moon JE, Paolino KM, Newcomer R, McLain DE, et al. (2014) A Phase 1 clinical trial of Hantaan virus and Puumala virus M-segment DNA vaccines for haemorrhagic fever with renal syndrome delivered by intramuscular electroporation. *Clin Microbiol Infect*.
22. Enama ME, Ledgerwood JE, Novik L, Nason MC, Gordon IJ, et al. (2014) Phase I Randomized Clinical Trial of VRC DNA and rAd5 HIV-1 Vaccine Delivery by Intramuscular (IM), Subcutaneous (SC) and Intradermal (ID) Administration (VRC 011). *PLoS ONE* 9: e91366.
23. Liu F, Song Y, Liu D (1999) Hydrodynamics-based transfection in animals by systemic administration of plasmid DNA. *Gene Ther* 6: 1258-1266.
24. Wells DJ (2004) Gene therapy progress and prospects: electroporation and other physical methods. *Gene Ther* 11: 1363-1369.

25. Yamano S, Dai J, Hanatani S, Haku K, Yamanaka T, et al. (2014) Efficient in vivo gene delivery using modified Tat peptide with cationic lipids. *Biotechnol Lett*.
26. Zhi D, Zhang S, Cui S, Zhao Y, Wang Y, et al. (2013) The headgroup evolution of cationic lipids for gene delivery. *Bioconjug Chem* 24: 487-519.
27. Bhattacharya S, Bajaj A (2009) Advances in gene delivery through molecular design of cationic lipids. *Chem Commun (Camb)*: 4632-4656.
28. Uhl RG, 2nd, Stevenson A, Sidorov V (2007) Towards improved gene delivery: Flip of cationic lipids in highly polarized liposomes. *Chem Commun (Camb)*: 383-385.
29. Ilies MA, Seitz WA, Balaban AT (2002) Cationic lipids in gene delivery: principles, vector design and therapeutical applications. *Curr Pharm Des* 8: 2441-2473.
30. Bragonzi A, Boletta A, Biffi A, Muggia A, Sersale G, et al. (1999) Comparison between cationic polymers and lipids in mediating systemic gene delivery to the lungs. *Gene Ther* 6: 1995-2004.
31. Raftery R, O'Brien FJ, Cryan SA (2013) Chitosan for gene delivery and orthopedic tissue engineering applications. *Molecules* 18: 5611-5647.
32. Duval RE, Clarot I, Dumarcay-Charbonnier F, Fontanay S, Marsura A (2012) Interest of designed cyclodextrin-tools in gene delivery. *Ann Pharm Fr* 70: 360-369.
33. Bartlett DW, Davis ME (2006) Insights into the kinetics of siRNA-mediated gene silencing from live-cell and live-animal bioluminescent imaging. *Nucleic Acids Res* 34: 322-333.
34. Shcharbin D, Shakhbazau A, Bryszewska M (2013) Poly(amidoamine) dendrimer complexes as a platform for gene delivery. *Expert Opin Drug Deliv* 10: 1687-1698.
35. Daneshvar N, Abdullah R, Shamsabadi FT, How CW, Mh MA, et al. (2013) PAMAM dendrimer roles in gene delivery methods and stem cell research. *Cell Biol Int* 37: 415-419.
36. Davis ME, Zuckerman JE, Choi CH, Seligson D, Tolcher A, et al. (2010) Evidence of RNAi in humans from systemically administered siRNA via targeted nanoparticles. *Nature* 464: 1067-1070.
37. Silhol M, Tyagi M, Giacca M, Lebleu B, Vives E (2002) Different mechanisms for cellular internalization of the HIV-1 Tat-derived cell penetrating peptide and recombinant proteins fused to Tat. *Eur J Biochem* 269: 494-501.

38. Hallbrink M, Oehlke J, Papsdorf G, Bienert M (2004) Uptake of cell-penetrating peptides is dependent on peptide-to-cell ratio rather than on peptide concentration. *Biochim Biophys Acta* 1667: 222-228.
39. Kilk K, Langel U (2005) Cellular delivery of peptide nucleic acid by cell-penetrating peptides. *Methods Mol Biol* 298: 131-141.
40. Mae M, Langel U (2006) Cell-penetrating peptides as vectors for peptide, protein and oligonucleotide delivery. *Curr Opin Pharmacol* 6: 509-514.
41. Amantana A, Moulton HM, Cate ML, Reddy MT, Whitehead T, et al. (2007) Pharmacokinetics, biodistribution, stability and toxicity of a cell-penetrating peptide-morpholino oligomer conjugate. *Bioconjug Chem* 18: 1325-1331.
42. Ward B, Seal BL, Brophy CM, Panitch A (2009) Design of a bioactive cell-penetrating peptide: when a transduction domain does more than transduce. *J Pept Sci* 15: 668-674.
43. Du J, Sun Y, Shi QS, Liu PF, Zhu MJ, et al. (2012) Biodegradable Nanoparticles of mPEG-PLGA-PLL Triblock Copolymers as Novel Non-Viral Vectors for Improving siRNA Delivery and Gene Silencing. *Int J Mol Sci* 13: 516-533.
44. Zhou J, Patel TR, Fu M, Bertram JP, Saltzman WM (2012) Octa-functional PLGA nanoparticles for targeted and efficient siRNA delivery to tumors. *Biomaterials* 33: 583-591.
45. Lee SH, Mok H, Lee Y, Park TG (2011) Self-assembled siRNA-PLGA conjugate micelles for gene silencing. *J Control Release* 152: 152-158.
46. Cun D, Jensen DK, Maltesen MJ, Bunker M, Whiteside P, et al. (2011) High loading efficiency and sustained release of siRNA encapsulated in PLGA nanoparticles: quality by design optimization and characterization. *Eur J Pharm Biopharm* 77: 26-35.
47. Mirkin CA, Stegh AH (2014) Spherical nucleic acids for precision medicine. *Oncotarget* 5: 9-10.
48. Zhang Y, Kim WY, Huang L (2013) Systemic delivery of gemcitabine triphosphate via LCP nanoparticles for NSCLC and pancreatic cancer therapy. *Biomaterials* 34: 3447-3458.
49. Yang Y, Li J, Liu F, Huang L (2012) Systemic delivery of siRNA via LCP nanoparticle efficiently inhibits lung metastasis. *Mol Ther* 20: 609-615.
50. Sinha B, Muller RH, Moschwitz JP (2013) Bottom-up approaches for preparing drug nanocrystals: formulations and factors affecting particle size. *Int J Pharm* 453: 126-141.

51. Canelas DA, Herlihy KP, DeSimone JM (2009) Top-down particle fabrication: control of size and shape for diagnostic imaging and drug delivery. *Wiley Interdiscip Rev Nanomed Nanobiotechnol* 1: 391-404.
52. Rolland JP, Maynor BW, Euliss LE, Exner AE, Denison GM, et al. (2005) Direct fabrication and harvesting of monodisperse, shape-specific nanobiomaterials. *J Am Chem Soc* 127: 10096-10100.
53. Rolland JP, Van Dam RM, Schorzman DA, Quake SR, DeSimone JM (2004) Solvent-resistant photocurable liquid fluoropolymers for microfluidic device fabrication [corrected]. *J Am Chem Soc* 126: 2322-2323.
54. Xu J, Luft JC, Yi X, Tian S, Owens G, et al. (2013) RNA replicon delivery via lipid-complexed PRINT protein particles. *Mol Pharm* 10: 3366-3374.
55. Hasan W, Chu K, Gullapalli A, Dunn SS, Enlow EM, et al. (2012) Delivery of multiple siRNAs using lipid-coated PLGA nanoparticles for treatment of prostate cancer. *Nano Lett* 12: 287-292.
56. Dunn SS, Tian S, Blake S, Wang J, Galloway AL, et al. (2012) Reductively responsive siRNA-conjugated hydrogel nanoparticles for gene silencing. *J Am Chem Soc* 134: 7423-7430.
57. Bates DO, Hillman NJ, Williams B, Neal CR, Pocock TM (2002) Regulation of microvascular permeability by vascular endothelial growth factors. *J Anat* 200: 581-597.
58. Prabhakar U, Maeda H, Jain RK, Sevic-Muraca EM, Zamboni W, et al. (2013) Challenges and key considerations of the enhanced permeability and retention effect for nanomedicine drug delivery in oncology. *Cancer Res* 73: 2412-2417.
59. Jain RK, Stylianopoulos T (2010) Delivering nanomedicine to solid tumors. *Nat Rev Clin Oncol* 7: 653-664.
60. Hashizume H, Baluk P, Morikawa S, McLean JW, Thurston G, et al. (2000) Openings between defective endothelial cells explain tumor vessel leakiness. *Am J Pathol* 156: 1363-1380.
61. Hobbs SK, Monsky WL, Yuan F, Roberts WG, Griffith L, et al. (1998) Regulation of transport pathways in tumor vessels: role of tumor type and microenvironment. *Proc Natl Acad Sci U S A* 95: 4607-4612.
62. Padera TP, Stoll BR, Tooredman JB, Capen D, di Tomaso E, et al. (2004) Pathology: cancer cells compress intratumour vessels. *Nature* 427: 695.

63. Noguchi Y, Wu J, Duncan R, Strohal J, Ulbrich K, et al. (1998) Early phase tumor accumulation of macromolecules: a great difference in clearance rate between tumor and normal tissues. *Jpn J Cancer Res* 89: 307-314.
64. Matsumura Y, Maeda H (1986) A new concept for macromolecular therapeutics in cancer chemotherapy: mechanism of tumoritropic accumulation of proteins and the antitumor agent smancs. *Cancer Res* 46: 6387-6392.
65. Gabizon A, Catane R, Uziely B, Kaufman B, Safra T, et al. (1994) Prolonged circulation time and enhanced accumulation in malignant exudates of doxorubicin encapsulated in polyethylene-glycol coated liposomes. *Cancer Res* 54: 987-992.
66. Northfelt DW, Martin FJ, Working P, Volberding PA, Russell J, et al. (1996) Doxorubicin encapsulated in liposomes containing surface-bound polyethylene glycol: pharmacokinetics, tumor localization, and safety in patients with AIDS-related Kaposi's sarcoma. *J Clin Pharmacol* 36: 55-63.
67. Symon Z, Peyser A, Tzemach D, Lyass O, Sucher E, et al. (1999) Selective delivery of doxorubicin to patients with breast carcinoma metastases by stealth liposomes. *Cancer* 86: 72-78.
68. Harrington KJ, Mohammadtaghi S, Uster PS, Glass D, Peters AM, et al. (2001) Effective targeting of solid tumors in patients with locally advanced cancers by radiolabeled pegylated liposomes. *Clin Cancer Res* 7: 243-254.
69. Koukourakis MI, Koukouraki S, Fezoulidis I, Kelekis N, Kyrias G, et al. (2000) High intratumoural accumulation of stealth liposomal doxorubicin (Caelyx) in glioblastomas and in metastatic brain tumours. *Br J Cancer* 83: 1281-1286.
70. Koukourakis MI, Koukouraki S, Giatromanolaki A, Kakolyris S, Georgoulas V, et al. (2000) High intratumoral accumulation of stealth liposomal doxorubicin in sarcomas--rationale for combination with radiotherapy. *Acta Oncol* 39: 207-211.
71. Johnson JI, Decker S, Zaharevitz D, Rubinstein LV, Venditti JM, et al. (2001) Relationships between drug activity in NCI preclinical in vitro and in vivo models and early clinical trials. *Br J Cancer* 84: 1424-1431.
72. Usary J, Zhao W, Darr D, Roberts PJ, Liu M, et al. (2013) Predicting drug responsiveness in human cancers using genetically engineered mice. *Clin Cancer Res* 19: 4889-4899.
73. Combest AJ, Roberts PJ, Dillon PM, Sandison K, Hanna SK, et al. (2012) Genetically engineered cancer models, but not xenografts, faithfully predict anticancer drug exposure in melanoma tumors. *Oncologist* 17: 1303-1316.

74. Jones SW, Roberts RA, Robbins GR, Perry JL, Kai MP, et al. (2013) Nanoparticle clearance is governed by Th1/Th2 immunity and strain background. *Journal of Clinical Investigation* 123: 3061-3073.
75. Gordon S, Martinez FO (2010) Alternative activation of macrophages: mechanism and functions. *Immunity* 32: 593-604.
76. Martinez FO, Gordon S, Locati M, Mantovani A (2006) Transcriptional profiling of the human monocyte-to-macrophage differentiation and polarization: new molecules and patterns of gene expression. *J Immunol* 177: 7303-7311.
77. Patel PC, Giljohann DA, Daniel WL, Zheng D, Prigodich AE, et al. (2010) Scavenger receptors mediate cellular uptake of polyvalent oligonucleotide-functionalized gold nanoparticles. *Bioconjug Chem* 21: 2250-2256.
78. Sahay G, Alakhova DY, Kabanov AV (2010) Endocytosis of nanomedicines. *J Control Release* 145: 182-195.
79. Yang A, Liu W, Li Z, Jiang L, Xu H, et al. (2010) Influence of polyethyleneglycol modification on phagocytic uptake of polymeric nanoparticles mediated by immunoglobulin G and complement activation. *J Nanosci Nanotechnol* 10: 622-628.
80. Perry JL, Reuter KG, Kai MP, Herlihy KP, Jones SW, et al. (2012) PEGylated PRINT nanoparticles: the impact of PEG density on protein binding, macrophage association, biodistribution, and pharmacokinetics. *Nano Lett* 12: 5304-5310.
81. Steinmetz NF, Manchester M (2009) PEGylated viral nanoparticles for biomedicine: the impact of PEG chain length on VNP cell interactions in vitro and ex vivo. *Biomacromolecules* 10: 784-792.
82. Damodaran VB, Fee CJ, Ruckh T, Papat KC (2010) Conformational studies of covalently grafted poly(ethylene glycol) on modified solid matrices using X-ray photoelectron spectroscopy. *Langmuir* 26: 7299-7306.
83. Yang Q, Jones SW, Parker CL, Zamboni WC, Bear JE, et al. (2014) Evading Immune Cell Uptake and Clearance Requires PEG Grafting at Densities Substantially Exceeding the Minimum for Brush Conformation. *Molecular Pharmaceutics*: 140325070655007.
84. Choi HS, Liu W, Misra P, Tanaka E, Zimmer JP, et al. (2007) Renal clearance of quantum dots. *Nat Biotechnol* 25: 1165-1170.
85. Deen WM, Lazzara MJ, Myers BD (2001) Structural determinants of glomerular permeability. *Am J Physiol Renal Physiol* 281: F579-596.

86. Caron WP, Lay JC, Fong AM, La-Beck NM, Kumar P, et al. (2013) Translational studies of phenotypic probes for the mononuclear phagocyte system and liposomal pharmacology. *J Pharmacol Exp Ther* 347: 599-606.
87. Caron WP, Song G, Kumar P, Rawal S, Zamboni WC (2012) Interpatient pharmacokinetic and pharmacodynamic variability of carrier-mediated anticancer agents. *Clin Pharmacol Ther* 91: 802-812.
88. Caron WP, Clewell H, Dedrick R, Ramanathan RK, Davis WL, et al. (2011) Allometric scaling of pegylated liposomal anticancer drugs. *J Pharmacokinet Pharmacodyn* 38: 653-669.
89. Paciotti GF, Myer L, Weinreich D, Goia D, Pavel N, et al. (2004) Colloidal gold: a novel nanoparticle vector for tumor directed drug delivery. *Drug Deliv* 11: 169-183.
90. Almeida JP, Lin AY, Langsner RJ, Eckels P, Foster AE, et al. (2014) In vivo immune cell distribution of gold nanoparticles in naive and tumor bearing mice. *Small* 10: 812-819.
91. Gao H, Liu J, Yang C, Cheng T, Chu L, et al. (2013) The impact of PEGylation patterns on the in vivo biodistribution of mixed shell micelles. *Int J Nanomedicine* 8: 4229-4246.
92. Gratton SE, Pohlhaus PD, Lee J, Guo J, Cho MJ, et al. (2007) Nanofabricated particles for engineered drug therapies: a preliminary biodistribution study of PRINT nanoparticles. *J Control Release* 121: 10-18.
93. Klibanov AL, Maruyama K, Torchilin VP, Huang L (1990) Amphipathic polyethyleneglycols effectively prolong the circulation time of liposomes. *FEBS Lett* 268: 235-237.
94. Huang M, Wu W, Qian J, Wan DJ, Wei XL, et al. (2005) Body distribution and in situ evading of phagocytic uptake by macrophages of long-circulating poly (ethylene glycol) cyanoacrylate-co-n-hexadecyl cyanoacrylate nanoparticles. *Acta Pharmacol Sin* 26: 1512-1518.
95. Guo Y, Aweda T, Black KC, Liu Y (2013) Chemistry and theranostic applications of radiolabeled nanoparticles for cardiovascular, oncological, and pulmonary research. *Curr Top Med Chem* 13: 470-478.
96. Stojanov K, Zuhorn IS, Dierckx RA, de Vries EF (2012) Imaging of cells and nanoparticles: implications for drug delivery to the brain. *Pharm Res* 29: 3213-3234.
97. Becker JS, Jakubowski N (2009) The synergy of elemental and biomolecular mass spectrometry: new analytical strategies in life sciences. *Chem Soc Rev* 38: 1969-1983.

98. Ganesh S, Iyer AK, Gattacceca F, Morrissey DV, Amiji MM (2013) In vivo biodistribution of siRNA and cisplatin administered using CD44-targeted hyaluronic acid nanoparticles. *J Control Release* 172: 699-706.
99. Crayton SH, Elias DR, Al Zaki A, Cheng Z, Tsourkas A (2012) ICP-MS analysis of lanthanide-doped nanoparticles as a non-radiative, multiplex approach to quantify biodistribution and blood clearance. *Biomaterials* 33: 1509-1519.
100. Billinton N, Knight AW (2001) Seeing the wood through the trees: a review of techniques for distinguishing green fluorescent protein from endogenous autofluorescence. *Anal Biochem* 291: 175-197.
101. Deyl Z, Macek K, Adam M, Vancikova O (1980) Studies on the chemical nature of elastin fluorescence. *Biochim Biophys Acta* 625: 248-254.
102. Liu Y, Tseng YC, Huang L (2012) Biodistribution studies of nanoparticles using fluorescence imaging: a qualitative or quantitative method? *Pharm Res* 29: 3273-3277.
103. Patel DV, McGhee CN (2013) Quantitative analysis of in vivo confocal microscopy images: a review. *Surv Ophthalmol* 58: 466-475.
104. Stender AS, Marchuk K, Liu C, Sander S, Meyer MW, et al. (2013) Single cell optical imaging and spectroscopy. *Chem Rev* 113: 2469-2527.
105. Moldavan A (1934) Photo-Electric Technique for the Counting of Microscopical Cells. *Science* 80: 188-189.
106. Gucker FT, Jr., O'Konski CT, et al. (1947) A photoelectronic counter for colloidal particles. *J Am Chem Soc* 69: 2422-2431.
107. Kamentsky LA, Melamed MR, Derman H (1965) Spectrophotometer: new instrument for ultrarapid cell analysis. *Science* 150: 630-631.
108. Kamentsky LA, Melamed MR (1967) Spectrophotometric cell sorter. *Science* 156: 1364-1365.
109. Coulter WH (1956) High speed automatic blood cell counter and analyzer. *Proc Natl Electron Conf* 12: 1034-1040.
110. Fulwyler MJ (1965) Electronic separation of biological cells by volume. *Science* 150: 910-911.



111. Dittrich W, Gohde W (1969) [Impulse fluorometry of single cells in suspension]. *Z Naturforsch B* 24: 360-361.
112. Van Dilla MA, Trujillo TT, Mullaney PF, Coulter JR (1969) Cell microfluorometry: a method for rapid fluorescence measurement. *Science* 163: 1213-1214.
113. Drapkin RL, Adreeff M, Koziner B, Strife A, Wisniewski D, et al. (1979) Subpopulations of human peripheral blood cells: analysis of granulocytic progenitor cells by flow cytometry and immunologic surface markers. *Am J Hematol* 7: 163-172.
114. Steen HB, Boye E, Skarstad K, Bloom B, Godal T, et al. (1982) Applications of flow cytometry on bacteria: cell cycle kinetics, drug effects, and quantitation of antibody binding. *Cytometry* 2: 249-257.
115. Pinkel D, Dean P, Lake S, Peters D, Mendelsohn M, et al. (1979) Flow cytometry of mammalian sperm: progress in DNA and morphology measurement. *J Histochem Cytochem* 27: 353-358.
116. Trask BJ, van den Engh GJ, Elgershuizen JH (1982) Analysis of phytoplankton by flow cytometry. *Cytometry* 2: 258-264.
117. Dunn PA, Tyrer HW (1981) Quantitation of neutrophil phagocytosis, using fluorescent latex beads. Correlation of microscopy and flow cytometry. *J Lab Clin Med* 98: 374-381.
118. Hedley DW (1989) Flow cytometry using paraffin-embedded tissue: five years on. *Cytometry* 10: 229-241.
119. Young BD, Ferguson-Smith MA, Sillar R, Boyd E (1981) High-resolution analysis of human peripheral lymphocyte chromosomes by flow cytometry. *Proc Natl Acad Sci U S A* 78: 7727-7731.
120. Goodwin PM, Johnson ME, Martin JC, Ambrose WP, Marrone BL, et al. (1993) Rapid sizing of individual fluorescently stained DNA fragments by flow cytometry. *Nucleic Acids Res* 21: 803-806.
121. Hercher M, Mueller W, Shapiro HM (1979) Detection and discrimination of individual viruses by flow cytometry. *J Histochem Cytochem* 27: 350-352.
122. Mathaes R, Winter G, Engert J, Besheer A (2013) Application of different analytical methods for the characterization of non-spherical micro- and nanoparticles. *Int J Pharm* 453: 620-629.
123. Nguyen R, Perfetto S, Mahnke YD, Chattopadhyay P, Roederer M (2013) Quantifying spillover spreading for comparing instrument performance and aiding in multicolor panel design. *Cytometry A* 83: 306-315.

124. Roederer M (2001) Spectral compensation for flow cytometry: visualization artifacts, limitations, and caveats. *Cytometry* 45: 194-205.
125. Williams RM, Piston DW, Webb WW (1994) Two-photon molecular excitation provides intrinsic 3-dimensional resolution for laser-based microscopy and microphotochemistry. *FASEB J* 8: 804-813.
126. Göppert-Mayer M (1931) Über Elementarakte mit zwei Quantensprüngen. *Annalen der Physik* 401: 273-294.
127. Denk W, Strickler JH, Webb WW (1990) Two-photon laser scanning fluorescence microscopy. *Science* 248: 73-76.
128. Helmchen F, Denk W (2005) Deep tissue two-photon microscopy. *Nat Methods* 2: 932-940.
129. Wang BG, König K, Halbhauer KJ (2010) Two-photon microscopy of deep intravital tissues and its merits in clinical research. *J Microsc* 238: 1-20.
130. Patterson GH, Piston DW (2000) Photobleaching in two-photon excitation microscopy. *Biophys J* 78: 2159-2162.
131. Kalies S, Kuertemeyer K, Heisterkamp A (2011) Mechanisms of high-order photobleaching and its relationship to intracellular ablation. *Biomed Opt Express* 2: 805-816.

## **CHAPTER II: IN VITRO ANALYSIS OF PRINT NANOPARTICLE FACTORS INFLUENCING CELL ASSOCIATION WITH EWING SARCOMA SPHEROIDS REVEALS A CHARGE AND DOSE DEPENDENCY**

### **2.1 Overview**

The signature of Ewing Sarcoma is the fusion protein EWS-FLI1. It has been shown that siRNA mediated knockdown can cause beneficial therapeutic effects in cell culture systems. However, delivery of siRNA in vivo presents unique challenges, requiring the use of a carrier. PRINT fabricated nanoparticles were examined for their suitability as an siRNA carrier in vitro. A spheroid culture model was used to mimic the 3-dimensional environment of a tumor. It was found that particle charge played a key role in determining the magnitude of cell association with particles, as determined by flow cytometry. Moreover, association was observed to plateau at higher doses of particles. However, confocal imaging suggests that the particles experience limited penetration into the spheroid. This implies that there may be a limit on particle association with cancer cells in vivo.

### **2.2 Introduction**

Ewing Sarcoma is characterized as a small round blue cell tumor, predominantly found in the axial skeleton regions. This cancer is identified by a signature genetic translocation resulting in a fusion protein between EWS and an ETS family protein[1-3]. Roughly 85% of all cases specifically contain an EWS-FLI-1 fusion, with the N-terminus of EWS and the C-terminal half of FLI-1. EWS is thought to be a protein involved in RNA processing, though its specific function is not well understood. FLI-1 is known to be a transcription factor, with an ETS domain in its C-terminus binding to the GGAA consensus sequence. Due to the presence of the ETS DNA binding domain in the fusion protein, the function of EWS-FLI is thought to be as a master regulator required for oncogenic transformation of the cells.

In a sense, Ewing Sarcoma is addicted to the EWS-FLI oncogene. Targeting this protein by siRNA-mediated knockdown results in growth inhibition of ewing sarcoma cell lines[4-9]. Based on this

result, EWS-FLI presents a very specific target with which to selectively inhibit ewing sarcoma cell growth as the translocation would only be found in the cancer cells. Other groups have tried using various types of nanoparticles to deliver siRNA against EWS-FLI[10-15]. These have shown effectiveness at knocking down EWS-FLI in culture and some success at slowing or delaying tumor growth in vivo.

PRINT particles have the ability to carry an siRNA cargo. This can be done using a PLGA-based matrix coated or fabricated with cationic lipids such as DOTA or DOTAP[16]. Without these cationic lipids it is difficult to prevent the siRNA from leeching out of the particle. Alternatively, PEG hydrogel particles can be fabricated to carry siRNA cargoes[17]. The siRNA can be carried by the particle either by electrostatic interactions or by direct conjugation. Electrostatic binding is not suitable for in vivo conditions as physiologic salt conditions interfere with the electrostatic interaction and cause release of the siRNA. Direct conjugation is accomplished by attaching a sulfhydryl group to the siRNA and creating a disulfide bonded siRNA covalently attached to the particle. This allows for release of the siRNA in the reducing conditions of the endosome, helping prevent premature release. Due to the presence of a plausible delivery system, it was decided to pursue PRINT siRNA delivery for Ewing Sarcoma. In vitro testing was undertaken to ascertain the optimal characteristics for PRINT particle delivery to Ewing Sarcoma cells. For these in vitro tests, a 3D culture system was used for evaluation. Essentially, a ball of cells was created to simulate the 3D nature of a tumor in vivo, termed a spheroid. This is in contrast to the conventional 2D culture system where cells are seeded on a flat surface. Spheroid models contain similar nutrient gradients found in tissue and have been shown to be more predictive of in vivo success than standard cultures[18-21]. In the experiments below, in vitro spheroid culture systems were used to probe for the optimal PRINT particle characteristics needed for successful siRNA delivery to Ewing Sarcoma cells.

## **2.3 Experimental Methods**

### **2.3.1 Materials**

Poly(ethylene glycol) diacrylate (MW 700) (PEG700DA), 2-aminoethyl methacrylate hydrochloride (AEM), diphenyl (2,4,6-trimethylbenzoyl)-phosphine oxide (TPO), and sucrose were purchased from Sigma-Aldrich. Thermo Scientific Dylight 488 maleimide, dimethylformamide (DMF), triethylamine (TEA),

pyridine, borate buffer (pH 8.6), acetic anhydride, and methanol were obtained from Fisher Scientific. Conventional filters (2  $\mu$ m) were purchased from Agilent and polyvinyl alcohol (MW 2000) (PVOH) was purchased from Acros Organics. PRINT molds (80 nm x 80 nm x 320 nm) were obtained from Liquidia Technologies. Tetraethylene glycolmonoacrylate (HP4A) was synthesized in-house as previously described[22]. Methoxy-PEG(5k)-succinimidyl carboxy methyl ester (mPEG5k-SCM) was purchased from Creative PEGWorks. Trypsin, DPBS, and cell culture media were purchased from Gibco. Fetal bovine serum was purchased from Cellgro.

### **2.3.2 PRINT Nanoparticle Fabrication**

The PRINT particle fabrication technique has been described previously in detail[23,24]. The preparticle solution was prepared by dissolving 3.5 wt% of the various reactive monomers in methanol. The reactive monomers included: a crosslinker made of an oligomeric PEG with a nominal molar mass of 700 g/mol terminally functionalized on both end groups with an acryloxy functionality (PEG700DA); a 4 repeat PEG chain containing a hydroxyl and an acrylate functional group (HP4A); an amine containing monomer (AEM) which served to provide the amine functionality used to conjugate PEG onto the surface of the PRINT particles; and in some cases a polymerizable fluorescent tag. In all cases a photoinitiator, TPO, was also added. The pre-particle solution was comprised of 68 wt% HP4A, 20 wt% AEM, 10 wt% PEG700DA, 1 wt% TPO and 1 wt% Dylight 488 maleimide or Dylight 650 maleimide. Using a # 3 Mayer rod (R.D. Specialties), a thin film of the pre-particles solution was drawn onto a roll of freshly corona treated PET, using a custom-made roll-to-roll lab line (Liquidia Technologies) running at 12 ft/min. The solvent was evaporated from this delivery sheet by exposing the film to a hot air dam derived from heat guns. The delivery sheet was laminated (80 PSI, 12 ft/min) to the patterned side of the mold, followed by delamination at the nip. Particles were cured by passing the filled mold through a UV-LED (Phoseon, 395 nm, 3 SCFM N<sub>2</sub>, 12 ft/min). A PVOH harvesting sheet was hot laminated to the filled mold (140°C, 80 PSI, 12 ft/min). Upon cooling to room temperature, particles were removed from the mold by splitting the PVOH harvesting sheet from the mold.

Particles were then harvested by dissolving the PVOH in a bead of water (1 mL of water per 3 ft of harvesting sheet). The particle suspension was passed through a 2 $\mu$ m filter (Agilent) to remove any

large particulates. To remove the excess PVOH, particles were centrifuged (Eppendorf Centrifuge 5417R) at ca. 21,000 g for 15 min, the supernatant was removed and the particles were re-suspended in sterile water. This purification process was repeated 4 times.

### **2.3.3 Nanoparticle Characterization**

Stock particle concentrations were determined by thermogravimetric analysis (TGA) using a TA Instruments Q5000 TGA. TGA analysis was conducted by pipetting 20 $\mu$ L of the stock nanoparticle solution into a tared aluminum sample pan. Samples suspended in water were heated at 30  $^{\circ}$ C/min to 130  $^{\circ}$ C, followed by a 10 minute isotherm at 130 $^{\circ}$ C. Samples suspended in DMF were heated at 30  $^{\circ}$ C/min to 170  $^{\circ}$ C, followed by a 10 minute isotherm at 170  $^{\circ}$ C. All samples were then cooled at 30  $^{\circ}$ C/min to 30  $^{\circ}$ C, followed by a 2 minute isotherm at 30  $^{\circ}$ C. TGA was also performed on a 20 $\mu$ L aliquot of supernatant from a centrifuged sample of the stock nanoparticle solution to account for the mass of any stabilizer remaining in each sample. The concentration of stabilizer was subtracted from the concentration of stock particle solution to determine the actual particle concentration. Particles were visualized by scanning electron microscopy (SEM) using a Hitachi S-4700 SEM. Prior to imaging, SEM samples were coated with 1.5 nm of gold-palladium alloy using a Cressington 108 auto sputter coater. Particle size and zeta potential were measured by dynamic light scattering (DLS) on a Zetasizer Nano ZS (Malvern Instruments, Ltd.).

### **2.3.4 PEGylation and Acetylation**

After purification, the particles were reconstituted in DMF following the centrifugation technique outlined above and the concentration of particles in DMF was determined by TGA. The particles fabricated contain free primary amine groups which were used as functional handles to react with mPEG5k-SCM. The particles (1 mg NPs in 1 mL DMF) were reacted with TEA (100  $\mu$ L) for 10 min at room temperature on a shaker plate (Eppendorf, 1400 rpm). The mPEG5k-SCM was dissolved in DMF(48mg/mL) and added to the reaction mixture (14 mg per mg NPs). The reaction mixture was shaken overnight and then quenched with borate buffer (100  $\mu$ L). The nanoparticle solution was then washed 3 times with DMF via centrifugation. Following PEGylation, particles were acetylated with acetic anhydride

to quench any unreacted amines and to yield a negative zeta potential. For acetylation, nanoparticles (1 mg NP in 1 mL DMF) were reacted with an excess (10 $\mu$ l) of pyridine and acetic anhydride (7 $\mu$ l). The reaction was carried out in a sonicator bath (Branson Ultrasonic Cleaner 1.4 A, 160 W) for 15 min, after which a second addition of acetic anhydride (7 $\mu$ l) was added and the suspension was sonicated for another 15 min. Following acetylation, the particles were washed by centrifugation one time in DMF, followed by a borate buffer wash to neutralize any acetic acid side product, and then 3 washes with sterile water. Post-acetylation, particles were analyzed by TGA, DLS and SEM and stored at 4°C.

### **2.3.5 Cells, cell culture, and particle dosing**

Cells were cultured in cell specific medium for each Ewing Sarcoma cell line. Each media mixture included 1% Penicillin/Streptomycin (Gibco). EWS502 and EWS894 cells required 15% FBS (Gemini Bio-products) in RPMI 1640 media (Gibco). A673 and MHH cells required 10% FBS in RPMI 1640. SKN-MC cells required Dulbecco's minimum essential medium (Gibco) with 10% FBS, 1mM L-Glutamine (Gibco), and 1x Non-essential amino acids (Gibco). RD-ES cells use RPMI 1640 with 10% FBS and L-Glutamine and SK-ES were cultured with McCoy's 5A (Gibco) with 15% FBS L-Glutamine. Hanging droplet spheroids were generated by trypsinization of the cells and resuspension to 20x10<sup>5</sup> cells/mL or a concentration such that twenty microliters would give a pre-determined amount of cells. Twenty microliters of the cell suspension was pipetted into a Nunc 60-well minitray (Thermofisher scientific cat# 12-565-155). The minitray was inverted and placed in a 150mm dish containing three 35mm dishes filled with water (without lid) to provide local humidity and prevent evaporation of the liquid in the minitray. Cells were incubated at 37°C and 5% CO<sub>2</sub> for 4-6 days to allow spheroid formation. Following spheroid formation, a maximum of 1-2ul of particles in water or water only was pipetted into each well used for experimentation. At least 10 wells per sample with 3 samples per group were used to quantify association.

### **2.3.6 Flow cytometry of spheroids**

Individual spheroids comprising one sample were collected into a single eppendorf tube and centrifuged. Spheroids were washed with PBS and then exposed to 100ul of 0.25% Trypsin (Gibco) at

room temperature for 3-5 minutes. FACS buffer (PBS with 2% FBS) was then added. The samples were analyzed with the Beckman-Coulter (Dako) Cyan ADP using the 488nm laser and the FITC emission filter (530/40). After forward and side scatter gating, particle association was determined by comparison of particle-dosed samples to the water only (0 $\mu$ g/mL) samples.

### **2.3.7 Imaging of spheroid growth**

Spheroids were imaged in the minitray under brightfield with a Zeiss Axiovert 200, a 10x objective, and camera. Images were taken of multiple spheroids 4 days after plating, with representative images shown here.

### **2.3.8 Confocal imaging**

After incubation with particles, multiple spheroids were fixed in 4% paraformaldehyde and contained on a slide. A triangular chamber was constructed on a glass slide using broken coverslips and sealed with nail polish. The fixed spheroids were washed with 1xPBS and put in the chamber in solution. Excess solution was then carefully pipetted away and the chamber covered with a coverslip and sealed with nail polish. Spheroids were easily visible under the brightfield of a microscope and imaged. Images were obtained using an Olympus microscope. Both the 633 and 488nm lasers were used for excitation and emission was captured with an Alexa 647 and GFP filter, respectively.

## **2.4 Results**

### **2.4.1 PRINT fabrication of Hydrogels**

Nanoparticles were fabricated using the Particle Replication in Non-Wetting Templates (PRINT) technique.[1–3]. This method generates nanoparticles of highly consistent and precise size, shape, and composition. PRINT hydrogel nanoparticles composed of a covalently cross-linked hydrogel matrix. These were modified with various surface charges: either cationic, anionic, or PEGylated anionic. These particles were characterized by DLS and SEM and demonstrated a range of positive and negative zeta potentials and narrow size distributions (Figure 2.1).



#### **2.4.2 Spheroid formation of Ewing Sarcoma cell lines**

To explore the in vitro influence of particle characteristics on nanoparticle association, we wanted to use a spheroid cell culture model to represent the three dimensional nature of a tumor. It was unknown whether the Ewing Sarcoma cell lines available to me would form spheroids. The first experiment was to determine which cell lines would form a spheroid and what cell density was needed. The EWS502, EWS894, SK-N-MC, SK-ES, MHH, and RD-ES cell lines were tested at 500, 1000, and 2000 cells per well. The cells were incubated for 4 days and spheroid formation assessed. Images were obtained of the cultures and they definitively show that all Ewing Sarcoma cell lines tested formed spheroids (Figure 2.2).

#### **2.4.3 Effect of particle charge and dose**

The next set of experiments examined the effects of particle charge and dose on the association of particles with cells using this spheroid model. This experiment examined the association of different surface charges of 80 x 80 x 320 nm hydrogel particles. A striking difference in association was observed for the differently charged particles (Figure 2.3). As a function of dose, association was dose-dependent until a plateau was reached. However, the dose at which the particles reached the plateau was strikingly different between differently charged particles. Cationic particles showed 70% association at 7.5µg/mL, whereas anionic particles show 70% association only at 30µg/mL. PEGylated anionic particles showed the least association as the maximum association of 40% was reached at 60µg/mL. These trends and relative amount of association was similar between two separate cell lines, EWS502 and A673.

#### **2.4.4 Confocal imaging of spheroid association**

Spheroids were incubated with hydrogel nanoparticles and confocal imaging was performed to ascertain whether the particles were penetrating the spheroid. Images were taken of a Z-stack through the spheroid and collected into a montage. The spheroids expressed GFP, with the nanoparticle being fluorescently labeled with Dylight 650. From the images it is clear that the particles show minimal penetration to the middle of the spheroid (Figure 2.4).

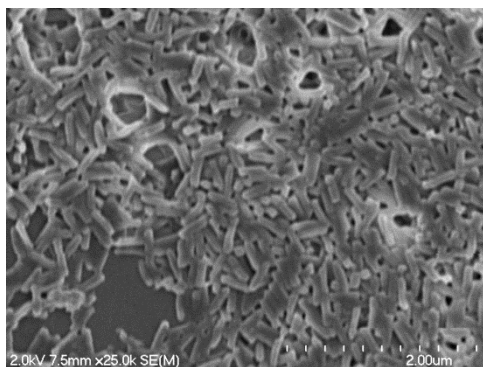
## 2.5 Discussion

Spheroid formation is a suggestive measure of the ability of cells to form cancers in vivo due to the anchorage-independent growth it requires. However, this is not a property found in all cancer cell lines[25,26]. It is therefore surprising that all Ewing Sarcoma cell lines studied readily formed multicellular tumor spheroids.

It is well known that cationic particles efficiently associate with cells in vitro[27-32]. That PRINT particle charge dominates the resulting association or that cationic particles perform best is not surprising. However, the lack of penetrance of the spheroid is an intriguing observation. These data would suggest that in vivo the limiting factor for delivery of particles would be penetrating the tumor. This hypothesis has been investigated previously[33-35] and it does seem to play a role in particle diffusion into the tumor, however these studies tend to be more qualitative and image-based. Therefore, quantification of the fraction of cells receiving particles seem to lacking and could be an important piece of supporting data. Moreover, these studies focus on cancer cells. Tumors are a complex mixture of cell types[36-38] and further examination of particle distribution on a cellular level may be informative, especially in vivo.

## 2.6 Conclusions

In a spheroid culture system, modeling the 3-dimensional nature of solid tumors, particle association was shown to be dependent upon the surface charge. Association was also shown to plateau at a level depending on the surface charge. Confocal imaging suggests that the particles fail to penetrate the entirety of the spheroid, which is the most likely explanation for the association plateau.



	Cationic	Acetylated	PEGylated
Z-average	260.3	207.7	235.0
PDI	0.107	0.045	0.104
Zeta potential	15.9±6.49	-25.3±10.8	-16.4±7.29

**Figure 2.1 SEM and DLS characterization of 80x320nm Hydrogel nanoparticles**

SEM image of Dylight 650 particles with DLS data in table at right.

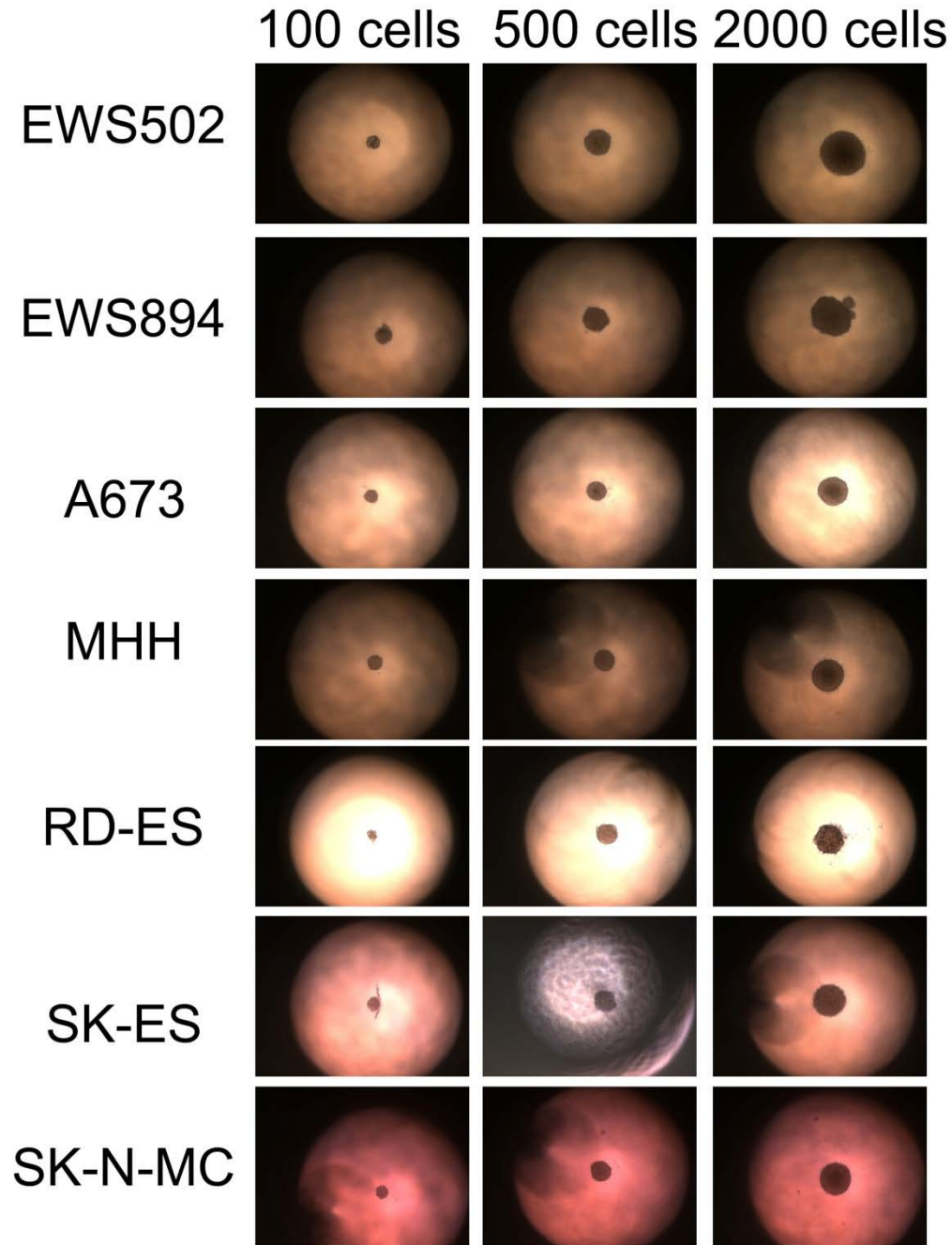


**Figure 2.2 Demonstration of spheroid formation ability of Ewing Sarcoma cells**

Various Ewing Sarcoma cell lines were counted, trypsinized and plated to form spheroids. Four days post plating the cells were imaged for spheroid formation. Each sample was created in duplicate with a representative image shown here.

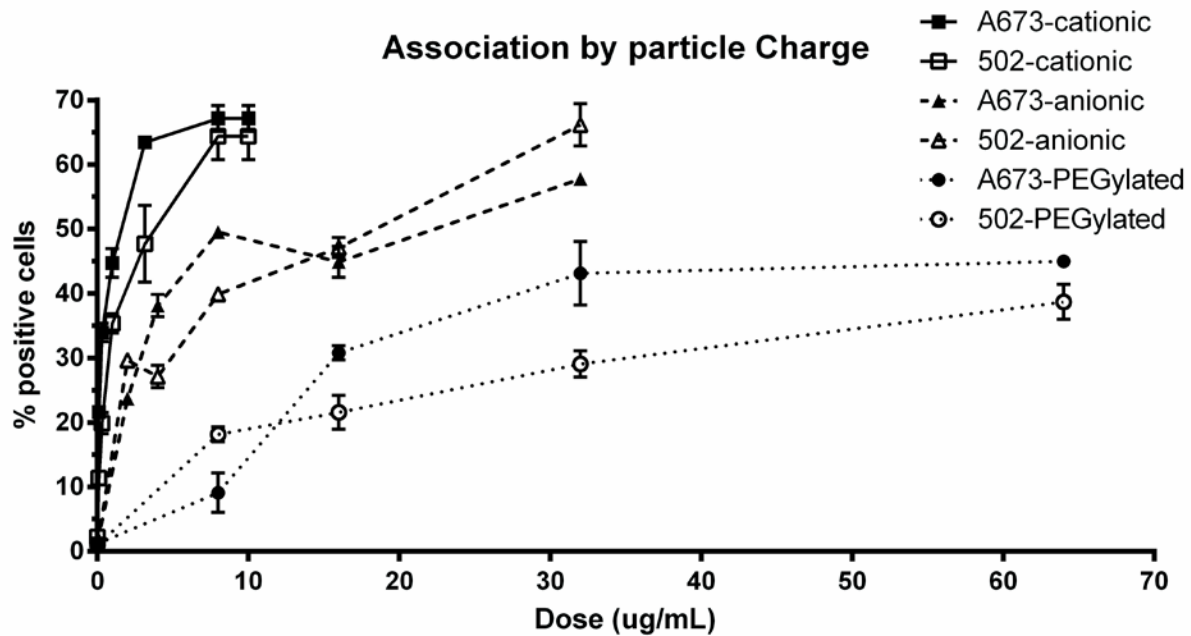


**Figure 2.3 Association of 80x320nm Hydrogel particles by dose, charge, and cell line in spheroids**

Various Ewing Sarcoma spheroids were incubated for 4 hours with 80x320nm Hydrogel PRINT particles of different surface charges. Flow cytometry was used to determine the percentage of cells associating with particles. Multiple spheroids (N=10) for each sample were used, with multiple samples (N=3) at each dose for each type of particle. The 0 $\mu$ g/mL dose was used to set a gate to determine the particle-positive cells. All error shown is  $\pm$  SD (N=3 samples).

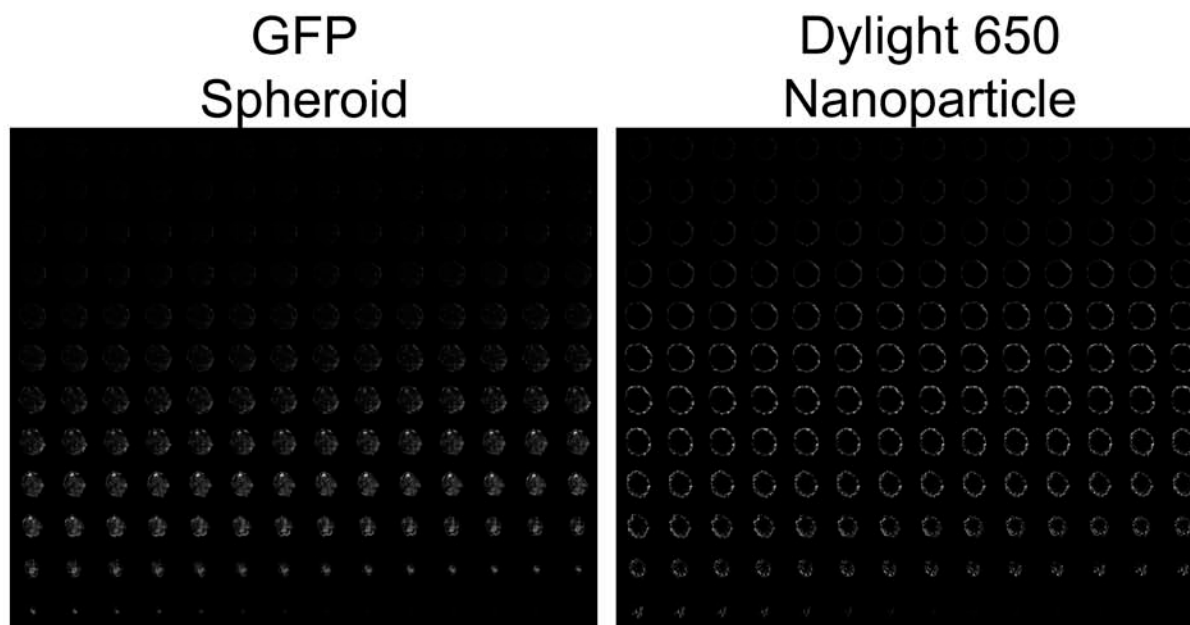


**Figure 2.4 Confocal imaging of Ewing Sarcoma spheroids**

Confocal images of a spheroid dosed with fluorescently labeled hydrogel nanoparticles. The images are a Z-stack of a representative spheroid.

## 2.7 REFERENCES

1. Erkizan HV, Uversky VN, Toretsky JA (2010) Oncogenic Partnerships: EWS-FLI1 Protein Interactions Initiate Key Pathways of Ewing's Sarcoma. *Clinical Cancer Research* 16: 4077-4083.
2. Janknecht R (2005) EWS-ETS oncoproteins: The linchpins of Ewing tumors. *Gene* 363: 1-14.
3. Lin PP, Wang Y, Lozano G (2011) Mesenchymal Stem Cells and the Origin of Ewing's Sarcoma. *Sarcoma* 2011: 1-8.
4. Kovar H AD, Jug G, Henockl C, Schemper M,, Delattre O TG, and Gadner H (1996) EWS-FLI1 antagonists induce growth inhibition of Ewing tumor cells in vitro. *Cell Growth & Differentiation* 7: 429-437.
5. Tanaka K IT, Harimaya K, Sato H, and Iwamoto Y (1997) EWS-FLI1 antisense oligodeoxynucleotide inhibits proliferation of Human Ewing's Sarcoma and primitive neuroectodermal tumor cells. *Journal of Clinical Investigation* 99: 239-247.
6. Chansky HA, Barahmand-pour F, Mei Q, Kahn-Farooqi W, Zielinska-Kwiatkowska A, et al. (2004) Targeting of EWS/FLI-1 by RNA interference attenuates the tumor phenotype of Ewing's sarcoma cells in vitro. *Journal of Orthopaedic Research* 22: 910-917.
7. Dohjima T (2003) Small interfering RNAs expressed from a Pol III promoter suppress the EWS/Fli-1 transcript in an Ewing sarcoma cell line. *Molecular Therapy* 7: 811-816.
8. Erkizan HV, Kong Y, Merchant M, Schlottmann S, Barber-Rotenberg JS, et al. (2009) A small molecule blocking oncogenic protein EWS-FLI1 interaction with RNA helicase A inhibits growth of Ewing's sarcoma. *Nature Medicine* 15: 750-756.
9. Smith R, Owen LA, Trem DJ, Wong JS, Whangbo JS, et al. (2006) Expression profiling of EWS/FLI identifies NKX2.2 as a critical target gene in Ewing's sarcoma. *Cancer Cell* 9: 405-416.
10. Alhaddad A, Adam M-P, Botsoa J, Dantelle G, Perruchas S, et al. (2011) Nanodiamond as a Vector for siRNA Delivery to Ewing Sarcoma Cells. *Small* 7: 3087-3095.
11. Hu-Lieskovan S, Heidel JD, Bartlett DW, Davis ME, Triche TJ (2005) Sequence-specific knockdown of EWS-FLI1 by targeted, nonviral delivery of small interfering RNA inhibits tumor growth in a murine model of metastatic Ewing's sarcoma. *Cancer Res* 65: 8984-8992.
12. Maksimenko A MC, Lambert G BJ, Fattal E MJ, and Couvreur P (2003) Oligonucleotides targeted against a junction oncogene are made efficient by nanotechnologies. *Pharmaceutical Research* 20: 1565-1567.

13. Lambert G, Bertrand JR, Fattal E, Subra F, Pinto-Alphandary H, et al. (2000) EWS Fli-1 Antisense Nanocapsules Inhibits Ewing Sarcoma-Related Tumor in Mice. *Biochemical and Biophysical Research Communications* 279: 401-406.
14. Takigami I, Ohno T, Kitade Y, Hara A, Nagano A, et al. (2011) Synthetic siRNA targeting the breakpoint of EWS/Fli-1 inhibits growth of Ewing sarcoma xenografts in a mouse model. *International Journal of Cancer* 128: 216-226.
15. Toub N, Bertrand J-R, Tamaddon A, Elhames H, Hillaireau H, et al. (2006) Efficacy of siRNA Nanocapsules Targeted Against the EWS–Fli1 Oncogene in Ewing Sarcoma. *Pharmaceutical Research* 23: 892-900.
16. Hasan W, Chu K, Gullapalli A, Dunn SS, Enlow EM, et al. (2012) Delivery of multiple siRNAs using lipid-coated PLGA nanoparticles for treatment of prostate cancer. *Nano Lett* 12: 287-292.
17. Dunn SS, Tian S, Blake S, Wang J, Galloway AL, et al. (2012) Reductively responsive siRNA-conjugated hydrogel nanoparticles for gene silencing. *J Am Chem Soc* 134: 7423-7430.
18. Carver K, Ming X, Juliano RL (2014) Multicellular Tumor Spheroids as a Model for Assessing Delivery of Oligonucleotides in Three Dimensions. *Molecular Therapy—Nucleic Acids* 3: e153.
19. Kunz-Schughart LA (1999) Multicellular tumor spheroids: intermediates between monolayer culture and in vivo tumor. *Cell Biol Int* 23: 157-161.
20. Hirschhaeuser F, Menne H, Dittfeld C, West J, Mueller-Klieser W, et al. (2010) Multicellular tumor spheroids: an underestimated tool is catching up again. *J Biotechnol* 148: 3-15.
21. Friedrich J, Ebner R, Kunz-Schughart LA (2007) Experimental anti-tumor therapy in 3-D: spheroids--old hat or new challenge? *Int J Radiat Biol* 83: 849-871.
22. Guzmán J, Iglesias MT, Riande E, Compañ V, Andrio A (1997) Synthesis and polymerization of acrylic monomers with hydrophilic long side groups. Oxygen transport through water swollen membranes prepared from these polymers. *Polymer* 38: 5227-5232.
23. Enlow EM, Luft JC, Napier ME, DeSimone JM (2011) Potent engineered PLGA nanoparticles by virtue of exceptionally high chemotherapeutic loadings. *Nano Lett* 11: 808-813.
24. Perry JL, Reuter KG, Kai MP, Herlihy KP, Jones SW, et al. (2012) PEGylated PRINT nanoparticles: the impact of PEG density on protein binding, macrophage association, biodistribution, and pharmacokinetics. *Nano Lett* 12: 5304-5310.



25. Carlsson J, Nilsson K, Westermark B, Ponten J, Sundstrom C, et al. (1983) Formation and growth of multicellular spheroids of human origin. *Int J Cancer* 31: 523-533.
26. Yuhas JM, Tarleton AE, Molzen KB (1978) Multicellular tumor spheroid formation by breast cancer cells isolated from different sites. *Cancer Res* 38: 2486-2491.
27. Gao LY, Liu XY, Chen CJ, Wang JC, Feng Q, et al. (2014) Core-shell type lipid/rPAA-Chol polymer hybrid nanoparticles for in vivo siRNA delivery. *Biomaterials* 35: 2066-2078.
28. Bexiga MG, Kelly C, Dawson KA, Simpson JC (2013) RNAi-mediated inhibition of apoptosis fails to prevent cationic nanoparticle-induced cell death in cultured cells. *Nanomedicine (Lond)*.
29. Pappalardo JS, Langelotti CA, Di Giacomo S, Olivera V, Quattrocchi V, et al. (2014) In vitro transfection of bone marrow-derived dendritic cells with TATp-liposomes. *Int J Nanomedicine* 9: 963-973.
30. Lin J, Alexander-Katz A (2013) Cell membranes open "doors" for cationic nanoparticles/biomolecules: insights into uptake kinetics. *ACS Nano* 7: 10799-10808.
31. Townson JL, Lin YS, Agola JO, Carnes EC, Leong HS, et al. (2013) Re-examining the size/charge paradigm: differing in vivo characteristics of size- and charge-matched mesoporous silica nanoparticles. *J Am Chem Soc* 135: 16030-16033.
32. Campbell RB, Fukumura D, Brown EB, Mazzola LM, Izumi Y, et al. (2002) Cationic charge determines the distribution of liposomes between the vascular and extravascular compartments of tumors. *Cancer Res* 62: 6831-6836.
33. Brown EB, Boucher Y, Nasser S, Jain RK (2004) Measurement of macromolecular diffusion coefficients in human tumors. *Microvasc Res* 67: 231-236.
34. Chauhan VP, Lanning RM, Diop-Frimpong B, Mok W, Brown EB, et al. (2009) Multiscale measurements distinguish cellular and interstitial hindrances to diffusion in vivo. *Biophys J* 97: 330-336.
35. Jain RK (2012) Delivery of molecular and cellular medicine to solid tumors. *Adv Drug Deliv Rev* 64: 353-365.
36. Budhu S, Wolchok J, Merghoub T (2013) The importance of animal models in tumor immunity and immunotherapy. *Curr Opin Genet Dev* 24C: 46-51.
37. Hanahan D, Weinberg RA (2011) Hallmarks of cancer: the next generation. *Cell* 144: 646-674.

38. Hanahan D, Weinberg RA (2000) The hallmarks of cancer. *Cell* 100: 57-70.

## **CHAPTER III: ANALYSIS OF PRINT NANOPARTICLE DISTRIBUTION WITHIN TUMORS REVEALS A CELL TYPE, SIZE, AND ROUTE OF ADMINISTRATION DEPENDENCY**

### **3.1 Overview**

Delivery of impermeable cargo for cancer therapy will most likely require cell type specific delivery. Thus, we determined the intratumoral fate PRINT nanoparticles by multi-color flow cytometry and quantified the overall accumulation of particles to the organ by radiolabeling. Despite dose-dependent accumulation of particles within the organ, particle association with cells became dose-independent at high doses. At the cellular level, cancer cells had a small fraction of particle-positive cells whereas macrophages showed the greatest amount of association both by population and per cell. However, the majority of the particles associating with cells were associating with cancer cells due to their relative abundance in the tumor. Reducing particle size or administering particles intratumorally increased cancer cell association and decreased macrophage association. This study demonstrates the importance of cell-lineage specific analysis of nanoparticle fate in vivo.

### **3.2 Introduction**

The importance of the Enhanced Permeation and Retention effect for nanocarrier-mediated drug delivery in oncology has resulted in a focus on the accumulation of particles in whole tumors.[1] Nanoparticle targeting to solid tumors is typically quantified by one of a variety of whole organ methods that determine the fraction of the injected dose of the carrier or cargo that accumulates in an organ or tumor.[2–13] However, tumors are composed of numerous cell types in addition to cancer cells, including fibroblasts, endothelial cells, macrophages and neutrophils.[14–17] Whole organ approaches are unable to discriminate between accumulation in these cell types or in the extracellular space. For cargo with an intracellular mechanism of action, such as nucleic acids and proteins, the delivery to specific cell types is crucial to characterizing nanoparticle efficacy and optimizing targeting.

Methods for the identification of intratumoral distribution include microscopy or flow cytometry. Confocal microscopy has been used to determine particle internalization *in vivo* by analyzing multiple sections of an organ.[18] However, meaningful quantification can be challenging. Flow cytometry permits concurrent cellular identification and nanoparticle quantification. Previous studies that have used flow cytometry to examine nanoparticle targeting to organs have not addressed the effects of particle characteristics (composition, shape, etc.) or dose on the accumulation in specific cells and do not correlate their findings with the whole organ.[19–21] Studies of nanoparticle targeting in tumors have focused exclusively on individual cell populations and, similarly to organ-based studies, have not explored the effects of particle properties or dose.[14,22–25] Studies that take into account nanocarrier properties together with intra-organ or intra-tumor distribution will best inform nanoparticle optimization.

One advantage of using the PRINT fabrication method is that the particles are of monodisperse size. Using this top-down fabrication strategy using a mold confers the advantage of reproducible production of these monodisperse particles. If the particles had a large variation in size (i.e. PDI) it is entirely possible that the size of the particle may cause preferential association with one cell population over another, confounding the results. This makes our results easier to interpret and analyze for the influence of particle characteristics on association with cells. PRINT also affords homogeneity in the composition of the particles and flexibility of choice in the desired nanoparticle material, bestowing a unique advantage among the other nanoparticle fabrication strategies.

Using a fluorescent mouse melanoma model and highly consistent PRINT nanoparticles, we found that a low fraction of cancer cells associate with particles. Moreover, on a per cell basis, macrophages associate with a greater amount of particles per cell. We also observe that particle size plays a significant role by increasing association with cancer cells.

### **3.3 Experimental Methods**

#### **3.3.1 Materials**

Poly(ethylene glycol) diacrylate (Mw 700) (PEG700DA), 2-aminoethyl methacrylate hydrochloride (AEM), diphenyl (2,4,6-trimethylbenzoyl)-phosphine oxide (TPO), and sucrose were purchased from Sigma-Aldrich. Thermo Scientific Dylight 488 maleimide, dimethylformamide (DMF), triethylamine (TEA),

pyridine, borate buffer (pH 8.6), acetic anhydride, and methanol were obtained from Fisher Scientific. Conventional filters (2  $\mu\text{m}$ ) were purchased from Agilent and polyvinyl alcohol (Mw 2000) (PVOH) was purchased from Acros Organics. PRINT molds (80 nm x 80 nm x 320 nm) were obtained from Liquidia Technologies. Tetraethylene glycolmonoacrylate (HP4A) was synthesized in-house as previously described[26]. Methoxy-PEG(5k)-succinimidyl carboxy methyl ester (mPEG5k-SCM) was purchased from Creative PEGWorks. Trypsin, DPBS, and cell culture media were purchased from Gibco. Fetal bovine serum was purchased from Cellgro.

### 3.3.2 PRINT Nanoparticle Fabrication

The PRINT particle fabrication technique has been described previously in detail[27,28]. The preparticle solution was prepared by dissolving 3.5 wt% of the various reactive monomers in methanol. The reactive monomers included: an oligomeric PEG with a nominal molar mass of 700 g/mol terminally functionalized on both end groups with an acryloxy functionality (PEG700DA); a 4 repeat PEG chain with a hydroxyl and acrylate functionalities (HP4A); an amine containing monomer (AEM) which served to provide the amine functionality used to conjugate PEG onto the surface of the PRINT particles; and in some cases a polymerizable fluorescent tag. In all cases a photoinitiator, TPO, was also added. The preparticle solution was comprised of 67.75 wt% HP4A, 20 wt% AEM, 10 wt% PEG700DA, 1 wt% TPO and 1.25 wt% Dylight 488 maleimide. Using a # 3 Mayer rod (R.D. Specialties), a thin film of the pre-particles solution was drawn onto a roll of freshly corona treated PET, using a custom-made roll-to-roll lab line (Liquidia Technologies) running at 12 ft/min. The solvent was evaporated from this delivery sheet by exposing the film to a hot air dam derived from heat guns. The delivery sheet was laminated (80 PSI, 12 ft/min) to the patterned side of the mold, followed by delamination at the nip. Particles were cured by passing the filled mold through a UV-LED (Phoseon, 395 nm, 3 SCFM N<sub>2</sub>, 12 ft/min). A PVOH harvesting sheet was hot laminated to the filled mold (140°C, 80 PSI, 12 ft/min). Upon cooling to room temperature, particles were removed from the mold by splitting the PVOH harvesting sheet from the mold. Particles were then harvested by dissolving the PVOH in a bead of water (1 mL of water per 3 ft of harvesting sheet). The particle suspension was passed through a 2 $\mu\text{m}$  filter (Agilent) to remove any large particulates. To remove the excess PVOH, particles were centrifuged (Eppendorf Centrifuge 5417R) at

ca. 21,000 g for 15 min, the supernatant was removed and the particles were re-suspended in sterile water. This purification process was repeated 4 times.

### **3.3.3 Nanoparticle Characterization**

Stock particle concentrations were determined by thermogravimetric analysis (TGA) using a TA Instruments Q5000 TGA. TGA analysis was conducted by pipetting 20 $\mu$ L of the stock nanoparticle solution into a tared aluminum sample pan. Samples suspended in water were heated at 30  $^{\circ}$ C/min to 130  $^{\circ}$ C, followed by a 10 minute isotherm at 130 $^{\circ}$ C. Samples suspended in DMF were heated at 30  $^{\circ}$ C/min to 170  $^{\circ}$ C, followed by a 10 minute isotherm at 170  $^{\circ}$ C. All samples were then cooled at 30  $^{\circ}$ C/min to 30  $^{\circ}$ C, followed by a 2 minute isotherm at 30  $^{\circ}$ C. TGA was also performed on a 20 $\mu$ L aliquot of supernatant from a centrifuged sample of the stock nanoparticle solution to account for the mass of any stabilizer remaining in each sample. The concentration of stabilizer was subtracted from the concentration of stock particle solution to determine the actual particle concentration. Particles were visualized by scanning electron microscopy (SEM) using a Hitachi S-4700 SEM. Prior to imaging, SEM samples were coated with 1.5 nm of gold-palladium alloy using a Cressington 108 auto sputter coater. Particle size and zeta potential were measured by dynamic light scattering (DLS) on a Zetasizer Nano ZS (Malvern Instruments, Ltd.).

### **3.3.4 PEGylation and Acetylation for in vitro and in vivo studies**

After purification, the particles were reconstituted in DMF following the centrifugation technique outlined above and the concentration of particles in DMF was determined by TGA. The particles fabricated contain free primary amine groups which were used as functional handles to react with mPEG5k-SCM. The particles (1 mg NPs in 1 mL DMF) were reacted with TEA (100  $\mu$ L) for 10 min at room temperature on a shaker plate (Eppendorf, 1400 rpm). The mPEG5k-SCM was dissolved in DMF(48mg/mL) and added to the reaction mixture (14 mg per mg NPs). The reaction mixture was shaken overnight and then quenched with borate buffer (100  $\mu$ L). The nanoparticle solution was then washed 3 times with DMF via centrifugation. Following PEGylation, particles were acetylated with acetic anhydride to quench any unreacted amines and to yield a negative zeta potential. For acetylation, nanoparticles (1

mg NP in 1 mL DMF) were reacted with an excess (10 $\mu$ l) of pyridine and acetic anhydride (7 $\mu$ l). The reaction was carried out in a sonicator bath (Branson Ultrasonic Cleaner 1.4 A, 160 W) for 15 min, after which a second addition of acetic anhydride (7 $\mu$ l) was added and the suspension was sonicated for another 15 min. Following acetylation, the particles were washed by centrifugation one time in DMF, followed by a borate buffer wash to neutralize any acetic acid side product, and then 3 washes with sterile water. Post-acetylation, particles were analyzed by TGA, DLS and SEM and stored at 4°C.

### **3.3.5 Cells, cell culture, and spheroid injections**

LKB498 cells were cultured as previously described[29] in high glucose DMEM (Gibco) with 10% FBS (Gemini Bio-products) and 1% Penicillin/Streptomycin (Gibco). Hanging droplet spheroids were generated by trypsinization of the cells and resuspension to 20x10<sup>5</sup> cells/mL. Twenty microliters of the cell suspension was pipetted into a Nunc 60-well minitray (ThermoFisher scientific). The minitray was inverted and placed in a 150mm dish containing three 35mm dishes filled with water(without lid) to provide local humidity and prevent evaporation of the liquid in the minitray. Cells were incubated at 37°C and 5% CO<sub>2</sub> for 4-6 days to allow spheroid formation. Individual spheroids were harvested and placed into 80  $\mu$ L media in a 0.5 mL microcentrifuge tube. Single spheroids in the tube were verified visually under a brightfield microscope and were placed on ice until time of injection. Athymic nude mice were anesthetized by inhalation with 2% isoflurane. A 14-mL conical tube was taped onto a heating pad next to the isoflurane nose cone under an Olympus MVX10 Macroview macroscope. The MVX10 is equipped with a MVPLAPO 1x objective, total mag 6.3–63x, NA 0.25, W.D. 65 mm. The mouse ear was affixed onto the conical tube with double-sided tape. The tumor spheroid, which was visible to the unaided eye in the tube, was drawn into a 10- $\mu$ L glass syringe (Hamilton) with a custom 1-inch 27G needle in a total volume of 2–3  $\mu$ L media. The glass syringe was held vertically for 1 min to allow the tumor spheroid to settle into the needle. While observing the ear through the macroscope, the needle (bevel facing up) was pierced into the dermis of the mouse ear and the spheroid in media was injected, which resulted in a transient visible bump under the surface of the skin. Successful spheroid injection was verified immediately by epifluorescence imaging with the MVX10 Texas Red filter.

### 3.3.6 Mice and Particle Injections

All animals were handled according to the NIH Guide for the Care and Use of Laboratory Animals. All procedures were approved by the University of North Carolina-Chapel Hill Institutional Animal Care and Use Committee (IACUC), protocol #11-154.0. All tumor spheroid injections were performed under inhalable isofluorane anesthesia and all efforts made to minimize animal discomfort as described previously[29]. All intravenous injections were done in concert with the UNC Animal Services Core. Suspensions of nanoparticles were made in isotonic 9.25% Sucrose and a maximum of 300 $\mu$ l per animal was injected via the tail vein for systemic administration. All animals herein are 4-8 week old, male Foxn1<sup>nu</sup> (athymic; C57BL/6J background) nude mice purchased from the UNC Animal Services Core. Tumors were of equal volumes between groups and ranged from 100-300mm<sup>3</sup>, as determined using caliper measurements and the equation  $V = (L/2) \times (W/2) \times (H/2) \times (4/3 \times \pi)$ . For the dose experiment, particles were resuspended at different concentrations (1.45, 4.65, 14.65mg/mL) to give similar injection volumes around 300 $\mu$ l.

### 3.3.7 Tumor Dissociation and Flow Cytometry

Tumors were harvested following animal sacrifice and placed in a 15mL conical tube containing a solution of 4.5mL DMEM with 10% FBS on ice. The conical tube was placed in a sterile tissue culture hood where 0.5 mL of a 3000U/mL Collagenase, 1000U/mL Hyaluronidase, 1000mg/L D-Glucose DMEM solution ("10x Collagenase/Hyaluronidase", StemCell Technologies, cat#07912) was added, with the conical tube then being placed in a 37°C incubator. Every 30 minutes for 1.5 hours the tubes were inverted to mix the solutions. After 1.5 hours, a plastic pipette was used to gently break up clumps of tissue. The conical tube was then placed back in the incubator for 1.5 hours, with inversion mixing every 30 minutes. Samples were then centrifuged at 600g for 5 minutes. Supernatant was discarded and samples were resuspended with a 1:4 mixture of HBSS+2%FBS (HF):0.8% NH<sub>4</sub>Cl and 0.1mM EDTA in water ("RBC lysis buffer", Stem Cell Technology, cat#07850). Samples were centrifuged at 450g for 5 minutes and resuspended in RBC lysis buffer. After a 5 minute centrifugation at 450g, samples were resuspended in 5mL of 0.05% Trypsin 0.53mM EDTA solution (Gibco) and incubated for 5 minutes at 37°C. The Trypsinization was stopped with 10mL of HF. Following centrifugation at 600g for 5 minutes,



samples were resuspended in 4.5 mL of 1U/mL Dispase in DMEF-12 (Stem Cell Technologies, cat#07923) and 0.5mL of a 1mg/mL Bovine Pancreas DNase I-PBS solution (Stem Cell Technologies, cat#07900). This mixture was incubated for 30 minutes at 37°C when 10 mL of HF was added to the sample. The sample was then filtered using a 40µm cell strainer (Fisher scientific, cat#22-363-547) and centrifuged at 450g for 5 minutes. Cells were resuspended in HF, placed on ice, and counted with a hemocytometer. Cells were then washed with PBS and resuspended to a concentration of  $2 \times 10^6$  cells/mL in PBS, with 1mL of cells being transferred to a 1.5mL eppendorf tube. Live-Dead Fixable Blue (Invitrogen, cat#L-23105) was then added at a concentration of 1ul/ $4 \times 10^6$  cells in 1mL PBS and incubated on ice for 15 minutes, protected from light. Cells were washed with PBS and resuspended in 100µl PBS. Fc Block (BD Biosciences cat#553142) was incubated at a concentration of 2ul/ $10^6$  cells for 5 minutes on ice, protected from light. PE-Cy7 CD31 (Clone 390, cat#102418), APC F4/80 (Clone BM8, cat#123116), Alexa 700 Ly6G (Clone 1A8, cat#127622), and Pacific Blue CD45 (Clone 30-F11, cat#103126) antibodies (Biolegend) were added to the cells and incubated for 1 hour on ice. Cells were then washed with PBS and resuspended in 500µl of 4% paraformaldehyde. After a 15 minute incubation at room temperature, cells were washed twice with FACS buffer (2%FBS in PBS), then resuspended in a final volume of 500µl of FACS Buffer and stored at 4°C until data acquisition on the BD LSRII using FACSDiva. Data analysis of FCS3 files was performed using FlowJo version 10.6. All surface markers were compared to their fluorescence minus one (FMO) controls to set appropriate gates. Particle association was determined by comparison to sucrose injected animals to determine appropriate gating.

### **3.3.8 Calculating the relative intratumoral distribution of particles by fluorescence**

The percentage of particle-positive cells was multiplied by their relative proportion in the sample. (e.g. 6% particle-positive cancer cells x 90% of the sample). This value was then multiplied by the mean fluorescence intensity of those particle positive cells to give a relative fluorescence value. Addition of all resulting fluorescence values gave a sum of total fluorescence. Dividing the value for each sub-population by the total gave a percentage of particles within that cellular compartment.

### 3.3.9 Radiation

High specific activity  $^{64}\text{Cu}$  ( $14000 \pm 7600$  Ci/mmol or  $518 \pm 28$  TBq/mmol) was obtained from the Washington University School of Medicine (St. Louis, MO, USA).  $^{64}\text{Cu}$  was produced on a CS-15 biomedical cyclotron by the  $^{64}\text{Ni}(p,n)^{64}\text{Cu}$  nuclear reaction using previously established methods[30], with a half-life of 12.7 hours. Particles were PEGylated as described above. Following PEGylation, particles were characterized as described above by TGA and reacted in 0.1 M  $\text{Na}_2\text{CO}_3$  buffer (pH 9) with 2-(4-isothiocyanatobenzyl) 1,4,7,10-tetraazacyclododecane-1,4,7,10-tetraacetic acid (p-SCN-Bn-DOTA) at 5 mg/mL (2:1 DOTA:AEM molar ratio). A conversion from positive to negative zeta potential indicated that the reaction went to completion. Particles were then incubated with  $^{64}\text{CuCl}_2$  for 30 minutes at 65 °C in 0.1 M ammonium acetate, washed 3 times by centrifugation with deionized water, and resuspended for injection in 9.25% sucrose.

### 3.3.10 Two-photon Microscopy

Tumor-bearing animals with tumors between  $10\text{--}30\text{mm}^3$  were imaged as previously described. Animals were anesthetized with isoflurane, and tumors were imaged before and after administration of particles. All imaging was performed at 910nm with an Olympus FV1000MPE mounted on an upright BX-61WI microscope, using a 25x, 1.05 N.A. (2 mm W.D.) water immersion objective to capture images. Software and microscope settings were consistent for all acquired images (the laser power was at 14% and each channel's PMT voltage was 580, 635, and 600, respectively). The laser unit is a MaiTai DeepSee tunable from 690–1040 nm with a pulse width < 100 fs. There were 3 Channel Non-descan Detectors used, Ch1 (420–460 nm) BFP, Ch2 (495–540nm) GFP, Ch3 (575–630 nm) RFP.

### 3.3.11 Statistics

All plotted data, unless otherwise noted, were analyzed using a one-way ANOVA and Tukey's post-hoc analysis. Mean Fluorescence data was analyzed using a two-way ANOVA and Tukey's post-hoc analysis.

### **3.4 Results**

#### **3.4.1 PRINT fabrication**

To explore the influence of particle characteristics on nanoparticle association, we used an established mouse melanoma model in which LKB498 cancer cells stably express the red fluorescent protein Td Tomato.[29] Tumor cells were inoculated intradermally and allowed to grow to a size of 100mm<sup>3</sup>. Nanoparticles were fabricated using the Particle Replication in Non-Wetting Templates (PRINT) technique.[27,28,31]. This method generates nanoparticles of highly consistent and precise size, shape, and composition. The PRINT nanoparticles were composed of a covalently cross-linked hydrogel matrix. Particles of 80 nm x 80 nm x 320 nm were fabricated and PEGylated as previously described.[27] Depending on the assay, fluorescent moieties were incorporated or copper-64 (<sup>64</sup>Cu) was chelated to the particles. Particles were characterized by DLS and SEM and demonstrated a similar negative zeta potential and narrow size distribution (Figure 3.1).

#### **3.4.2 Accumulation of particles in whole organ**

To determine nanoparticle accumulation using a whole-organ based approach, we injected <sup>64</sup>Cu radiolabeled PRINT nanoparticles at several doses into tumor bearing mice. Eighteen hours following particle administration animals were sacrificed, organs were harvested and gamma emission was measured. There was a wide distribution in the fractional association across organs ranging from ~45% of particles associating with the liver to ~0.2% of particles associating with the heart. These data are consistent with other types of nanoparticles. The fraction of the injected dose detected in each organ was consistent across the 3 doses (Figure 3.2a) indicating that the relative accumulation is independent of the dose administered. The total amount of particles contained within the tumor as well as in each organ increases in a dose-dependent manner (Figure 3.2b, c).

#### **3.4.3 Sub-organ Particle Accumulation by Flow Cytometry and the Effect of Dose**

We then examined the cellular composition of our tumor model. Tumors were enzymatically dissociated to create a single cell suspension and analyzed using multi-color flow cytometry (Figure 3.3). After gating on live cells, cancer cells (as distinguished from tumor cells which represents the mixture of

all cells in the tumor) were identified by Td Tomato fluorescence. The remaining non-cancer cells were separated into immune cells by CD45 expression (leukocyte marker). CD45<sup>+</sup> cells were further analyzed for the expression of F4/80 which marks mouse macrophages or Ly6G which marks neutrophils. CD45<sup>+</sup>F4/80<sup>-</sup>Ly6G<sup>-</sup> cells were classified as “other leukocytes” representing a mixture of cells that includes natural killer cells, dendritic cells, and B cells. CD31 surface expression in the CD45<sup>-</sup> cell population identified endothelial cells, with the remaining CD45<sup>-</sup> CD31<sup>-</sup> classified as fibroblast/other. Surface markers were compared to their fluorescence minus one (FMO) controls to ensure appropriate population gating. The tumor cell suspension reproducibly contained 89.9% cancer cells, 3.2% neutrophils, 1.1% macrophages, 0.64% other leukocytes, 0.49% endothelial cells, and 3.3% fibroblast/other cells (Figure 3.4). This strategy accounts for virtually every cell (98.6%) present in the tumor.

Mice were injected with fluorescent 80 x 80 x 320 nanoparticles at several doses (or with a sucrose control) as before. 18 hours after treatment tumors were dissected from mice, dissociated and analyzed by flow cytometry as described. Cancer cells demonstrated a dose-dependent association at doses between 12.5 to 40 mg/kg yielding 1.5% or 5.2% particle positive cells, respectively (Figure 3.5a). At the 125 mg/kg dose level, however, 6.2% association was observed. These data indicate a dose dependent increase in fractional association that seems to plateau at higher doses. Non-cancer cell populations showed a greater percentage of particle association. Roughly 60-80% of macrophages (Figure 3.5b) and 20-60% of neutrophils and other leukocytes (Figure 3.5c,d) were associated with PRINT particles. Approximately 15-35% of endothelial cells were positive for particle association (Figure 3.5e) with fibroblast/other cells having the lowest fractional association of 5-20% (Figure 3.5f). Strikingly, whereas macrophages and cells in the other leukocyte class demonstrate a sustained dose-dependent increase in nanoparticle association, cancer cells as well as endothelial cells and cells in the fibroblast/other class show no increase in fractional association above the 40 mg/kg dose.

In contrast to the fractional uptake described above which represents association across the population of cells, we also quantified fluorescence for individual cells. Among the cells analyzed, macrophages demonstrated the greatest mean fluorescence intensity (MFI) (Figure 3.6). MFI for macrophages was approximately 3.5 fold greater than that of the cancer cells, indicating that macrophages associate with a greater number of particles per cell. Like fractional association,

fluorescence signal per cell increased in a dose-dependent fashion at the low doses for cancer cells as well as immune cells. However, signal in cancer cells plateaued despite a three-fold increased dose. These data suggest that there is a limited fraction of cells that are able to associate with particles and that these cells have a biological limitation on the amount of nanoparticles they are able to take up. Using fluorescence, we also sought to quantify how much of the dose of particles were going to each cell type. Multiplying the mean fluorescence intensity by the percentage of particle-positive live cells for each cell type, we reasoned that this number represented the fraction of particle dose within the tumor associating with a given cell type. Adding this number to similar quantifications for other cell types, it was expressed as a percentage of particles associating with cells (Figure 3.7). This quantification suggests that particle-positive cancer cells represent 50% of the dose of particles associating with cells. Particle-positive macrophages represent 20-40% of the dose, with neutrophils representing 15-30%. Other leukocytes, endothelial cells, and fibroblast/other cells all account for 1-2% each.

#### **3.4.4 Effect of Particle Size on Association**

We then examined the influence of particle size on intratumoral cellular association. 55 x 70 nm particles were fabricated and functionalized as before (Figure 3.8). 55 x 70 nm and 80 x 320 nm particles were dosed at 25 mg/kg. Compared with the 80 x 320 nm particles, the 55 x 70 nm particles resulted in nearly twice the association with cancer cells (4.5 % vs 2.5%) as well as increased macrophage association (65% vs 37%) (Figure 3.9a,b). In contrast, neutrophils, other leukocytes, endothelial cells, and fibroblast/other cells exhibited similar fractional association (Figure 3.9c-f). These data suggest that the 55 x 70 nm particles associate with more cancer cells than 80 x 320 nm particles of similar chemical composition. The mean fluorescence intensity of the particle-positive cells was roughly similar across particle sizes (Figure 3.10) indicating that the cells associate with a similar particle mass. Quantification of the percentage of associating particle dose suggests that the dose associating with cancer cells doubles when 55 x 70 nm particles are used as compared to 80 x 320 nm particles (Figure 3.11). All other cell populations remain relatively constant in the fraction of associating particle dose.

### **3.4.5 Effect of Route of Administration on Association**

Intravenous administration of particles must overcome several hurdles in order to reach the cells of interest. Intratumoral administration therefore may be a useful mode of administration and was examined for its performance. Using 80 x 320 nm particles as above, a 25mg/kg dose was administered intravenously or intratumorally. The fraction of cancer cells associating with particles increased two-fold as compared to intravenous administration (Figure 3.12a). Endothelial cells and fibroblast association was unchanged (Figure 3.12b, c). In contrast, neutrophil, macrophage, and other leukocyte cell association was slightly decreased (Figure 3.12d, e, f). Mean fluorescence intensity demonstrated a 3-fold increase in the amount of fluorescence per cancer cell, with most other cell types showing no difference (Figure 3.13). The fraction of dose associating with cancer cells more than doubles when particles are administered IT (Figure 3.14). Macrophages, neutrophils, and other leukocytes are all observed to have less fractional dose associating with those cell types. Endothelial cells and fibroblast/other are relatively similar.

### **3.4.6 In vivo two photon microscopy**

Flow cytometry is a powerful tool, but is unable to give a definitive picture of how the particles are interacting with the 3-dimensional architecture of the tumor. For that, in vivo two-photon microscopy was used to visualize fluorescent particle distribution within LKB498 tumors. To collect baseline information, the contralateral ear of a tumor-bearing mouse was used. Using 80 x 320 nm particles as before and a 40mg/kg dose, particles were injected intravenously. Images were taken of the normal ear both before and 18 hours after injection of particles. This data suggests that in normal dermis, particle diffusion is quite limited to the area in or immediately around blood vessels (Figure 3.15). Particles can be seen contained in veins and aggregating in capillaries. From this baseline information, tumored ears were serially imaged following particle injection. Images were collected pre- and post-injection. This data reveals that particles are visible within the tumor as early as 10 minutes after injection (Figure 3.16a). Particle signal shows weak colocalization with cancer cells and strong colocalization with host cells, presumably immune or macrophage cells. (Figure 3.16a, b) Over time, nanoparticle fluorescence fades from the cancer cells and seems to stay constant in the host cells. (Figure 3.16a)

### 3.5 Discussion

To understand intratumoral distribution of nanoparticles we compared single-cell analysis to whole-organ accumulation using highly uniform PRINT nanoparticles. We observed a striking discordance between whole-tumor and individual cell analysis. Whole-organ quantification demonstrated dose-dependent accumulation. In contrast, single-cell based analysis revealed that delivery to cells becomes dose-independent at higher doses for cancer cells. Flow cytometry also enabled us to examine individual populations of cells within the tumor. We observed that macrophages associate with more particles per cell as compared to cancer cells. In vivo imaging reinforces the idea that host immune cells colocalize with significant amounts of particles. Moreover, that diffusion of the particles from blood vessels is quite pronounced in the tumor as compared to normal dermis. Particle properties also influenced intratumoral particle distribution as reduced particle size increased cancer cell association.

Single-cell assessment permits lineage-specific quantification of nanoparticle association. Biologically active membrane-impermeable cargo requires cell-specific delivery. The discrepancy between whole organ and single cell assessment limits the way accumulation experiments can be interpreted. A possible reason for this is that at higher doses, particle accumulation is predominantly in the extracellular space. A plausible explanation for this is that cells near blood vessels have a limit to their capacity to associate with particles. Thus, particles at higher doses continue to be deposited into the extracellular space. Secondly, despite the low abundance of macrophages within the tumor, the fraction of dose going to the macrophages may be disproportionate due the high per cell association of macrophages. This fact was visually supported by the in vivo two-photon imaging as Td Tomato expressing cells had low colocalization of particles, whereas host cells, presumably macrophages had the brightest fluorescence. This could be due to macrophages being near the available blood vessels or diffusion into the tumor itself. The declining or disappearing of particle signal in the cancer cells could be attributable to multiple processes: particle degradation, cancer cell mitosis, or cancer cell death. The particles have covalent carbon-carbon bonds making degradation of the particle a slow process and an unlikely culprit. Cancer cell death is also unlikely due to the numerous in vitro studies showing negligible cytotoxicity of this particle type across many cancer types. Thus, it is most likely cancer cell mitosis that causes a dilution effect of the particle fluorescence.

Use of PRINT nanoparticles allows us to carefully examine the influence of particle properties on cell association. One factor we examined was particle size. Reduction in particle size had a seemingly specific effect on increasing cancer cell association. Since an equivalent dose (by mass) of a smaller particle will yield greater numbers of particles, it is possible that the increased number of particles will augment delivery of the particles beyond the capillary bed of the tumor. Smaller sized particles may also penetrate the tumor more efficiently, coming in contact with more cancer cells. Nonetheless, this study supports our hypothesis that particle-specific features will influence intratumoral distribution and these features could be manipulated to target cell populations in tumors and organs. Mean fluorescence intensity was similar for both sized particles indicating that a similar mass of particles is contained in each cell. For a given mass, there are roughly 9.6 times as many 55 x 70 nm particles as compared to 80 x 320 nm particles. Hence, for the mean fluorescence data it seems to indicate that each cell contains a similar mass of particles, though roughly 9.6 times greater number of 55 x 70 nm particles in each cell than 80 x 320 nm particles. The role that particle number plays in cell association is unclear from these studies. Moreover, the role that particle number plays in efficacious delivery of therapeutics is quite opaque. Greater numbers of particles may provide greater diffusive force into the tumor. It is possible that large numbers of particles may decrease the clearance of particles from the blood, allowing greater contact with cancer cells. Clearly, from the 80 x 320 data there is a limit to the influence that particle number has on cell association. What contribution particle number has on increased association in addition to particle size is difficult to discern from the experiments here. That the greater number of 55 x 70 nm particles present at a given mass is solely responsible for the increase in association seems unlikely, but may play a role for the difference in association observed here.

Route of administration also seemed to play a role in the relative association of the various cell types. Intratumoral administration was observed to shift particle distribution to cancer cells and away from phagocytic cell types like macrophages, neutrophils, and other leukocytes. Most of the animals in the intratumoral group were unable to contain the full volume of particles administered. That the data shows a significant shift despite this experimental issue is compelling and suggests that the actual benefit may be greater than observed here.



### **3.6 Conclusions**

In conclusion, we have developed an approach to quantify specific nanoparticle uptake across the cellular compartments that constitute a tumor. Moreover, we demonstrated that particle characteristics can influence the association with these compartments. While flow cytometry is a powerful technique, in this application it is unable to discriminate whether the particles are surface bound or internalized in cells. The analysis of nanoparticle accumulation on a cellular level using two photon in vivo imaging supports the conclusions made by flow cytometry. Importantly, these experiments demonstrate that organ-level analysis of accumulation does not completely correlate with particle association with cells. We suspect that the difference results from deposition or retention of nanoparticles in the extracellular space. Cellular-level quantification is particularly relevant when delivering cargo that depends on an intracellular mechanism.



**Figure 3.1 SEM and DLS of 80x320nm Hydrogel particles conjugated with DOTA**

SEM image of 80x320nm particles, with resulting DLS values in the top left corner.

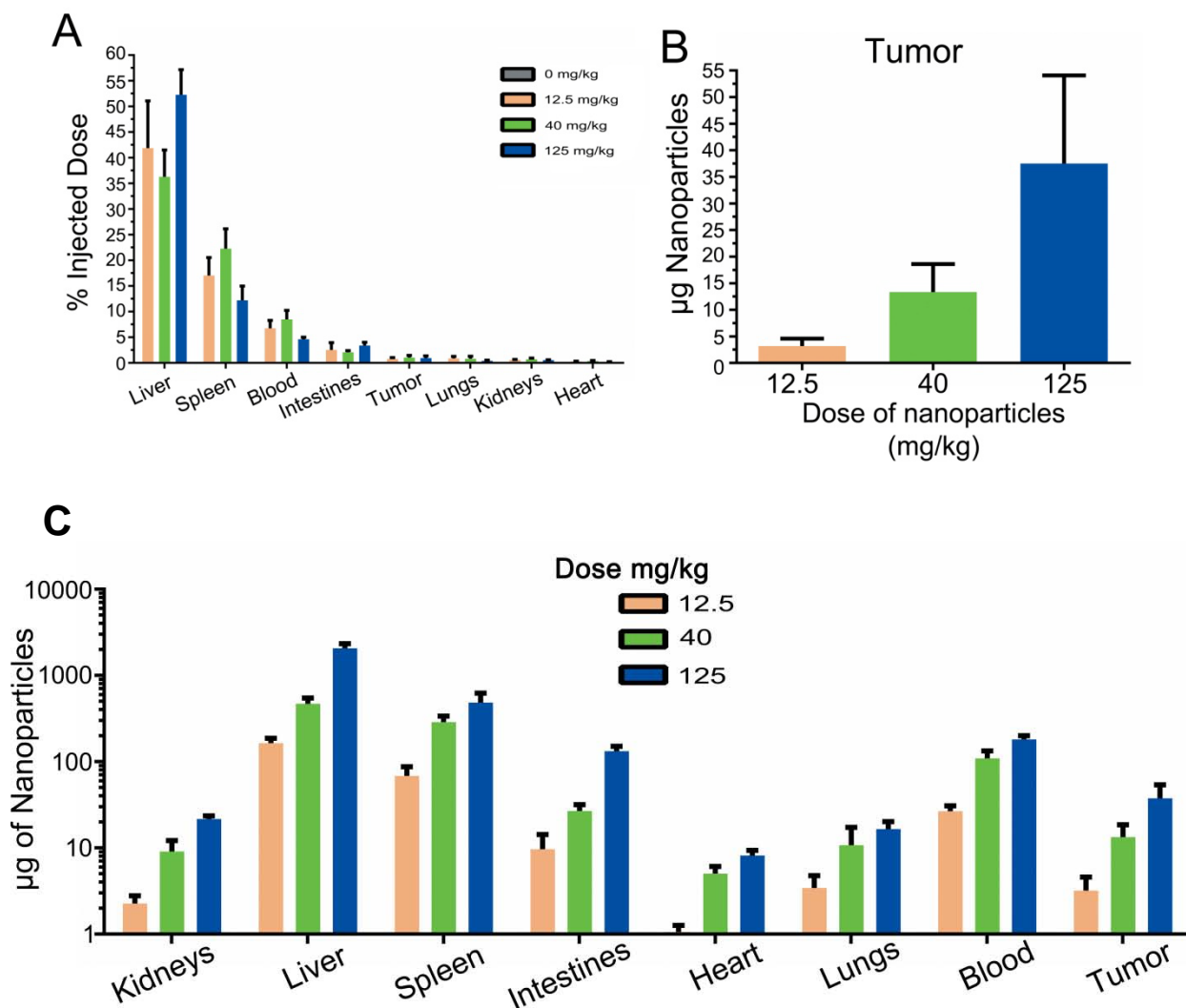


**Figure 3.2 Accumulation of particles in tumors as measured by  $^{64}\text{Cu}$  radioactivity**

A) Calculated percent injected dose for each organ. B) Calculated amount of nanoparticles contained within the tumor for each dose administered. C) Calculated amount of nanoparticles contained within all organs for each dose administered. All error shown is  $\pm$  SD (N=4).

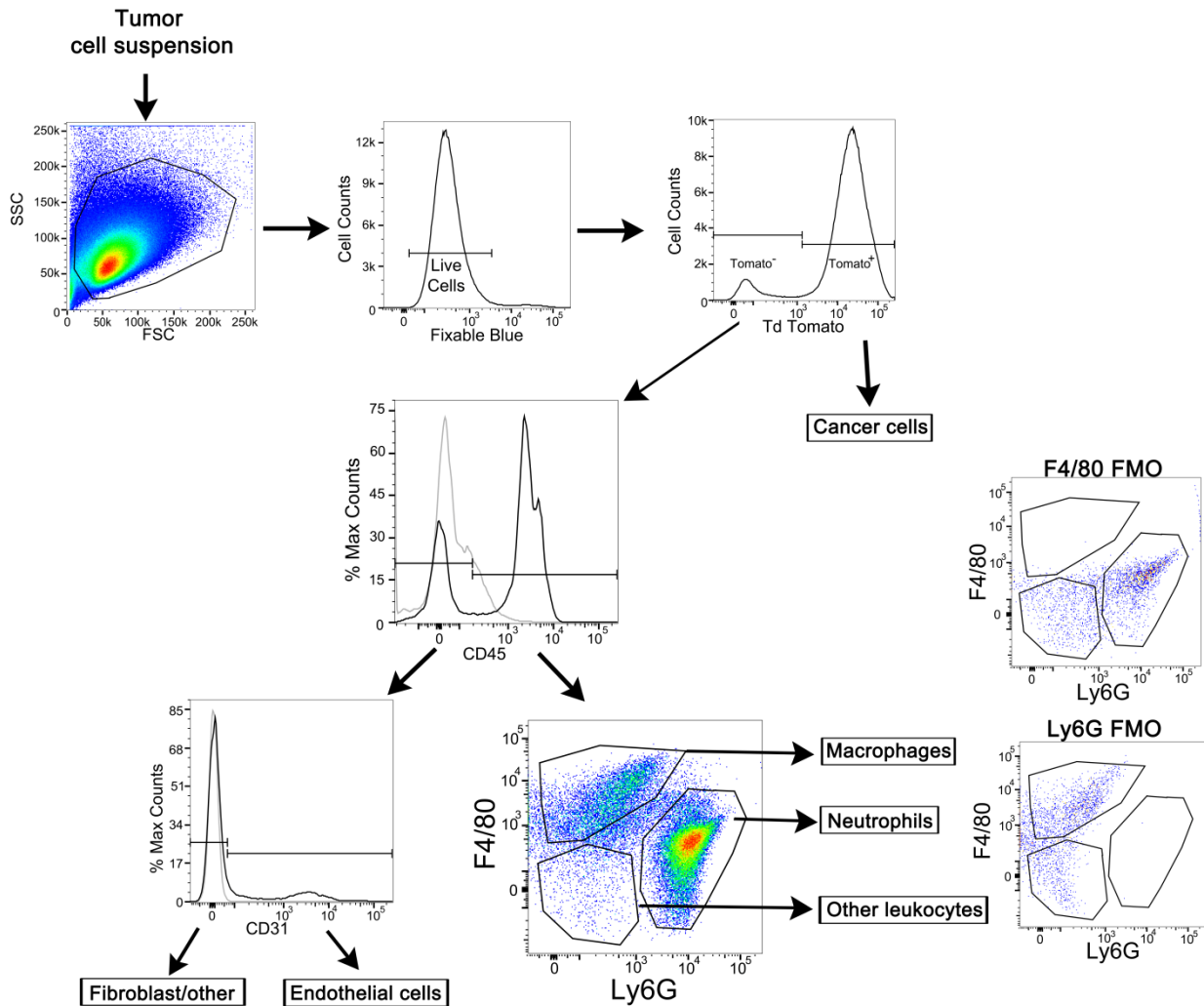


**Figure 3.3 Flow cytometry gating scheme for analysis**

Pictorial representation of flow cytometry gating scheme for cell population identification. Representative histograms are shown for helpful reference. In single color histograms, the grey line is the FMO control, with the black line representing a sample.

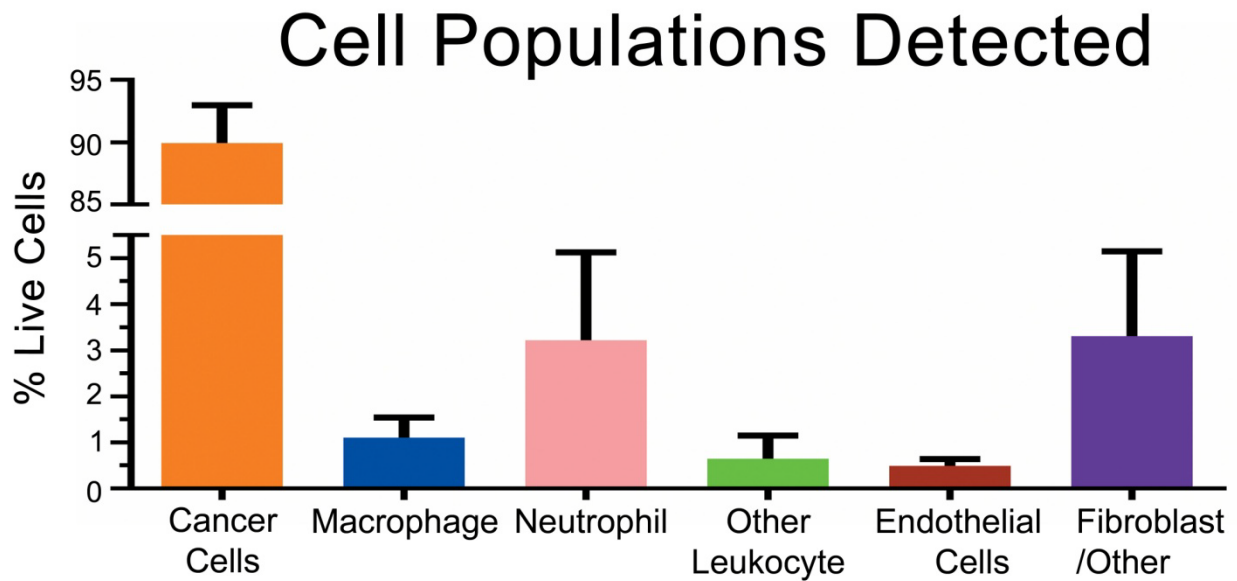


**Figure 3.4 Resulting proportion of cell populations detected from gating scheme**

After gating, the percentage of each cell population was expressed as percentage of all gated live cells.

This data represents two experiments, encompassing particle and non-particle dosed animals, with the combined data shown here. The error is  $\pm$ SD (N = 32).

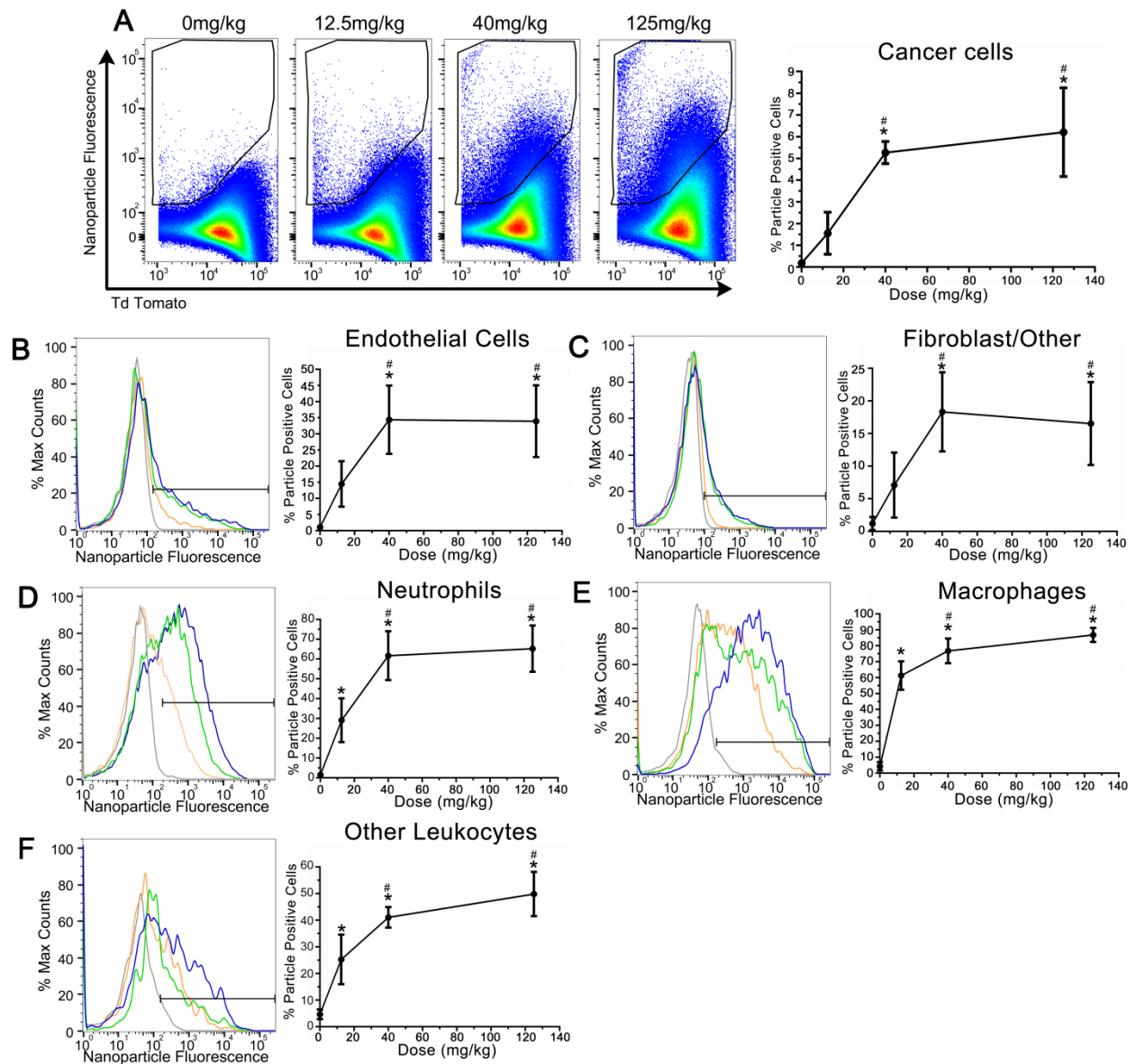


**Figure 3.5 Particle association as a function of dose**

Particle association for each sub-population was determined across the 4 dose groups and quantified using the sucrose administered animals as the particle FMO. Association is expressed as the percentage of particle positive cells for each sub-population. A representative histogram is shown to the left of the quantitation. Error shown is  $\pm$ SD (N=4 per dose group). The \* symbol represents  $p < 0.05$  vs 0mg/kg and # represents  $p < 0.05$  vs 12.5mg/kg dose.

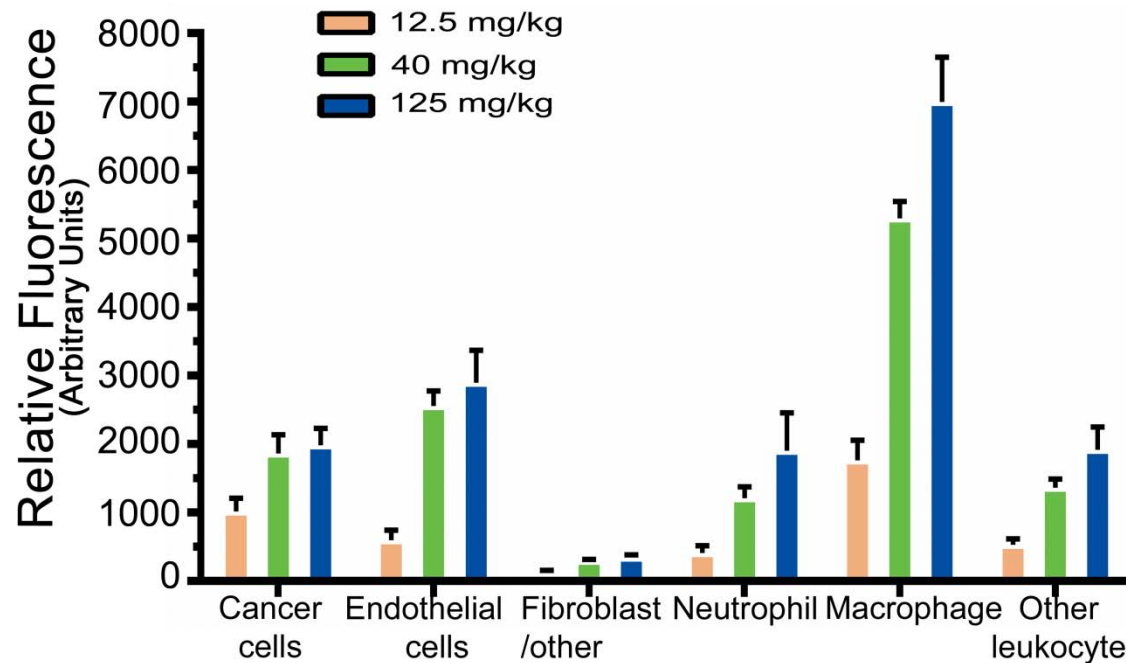


**Figure 3.6 Mean fluorescence intensity when different particle doses are administered**

Quantification of the relative fluorescence in each particle-positive population as gated and quantified in Figure 3.5.

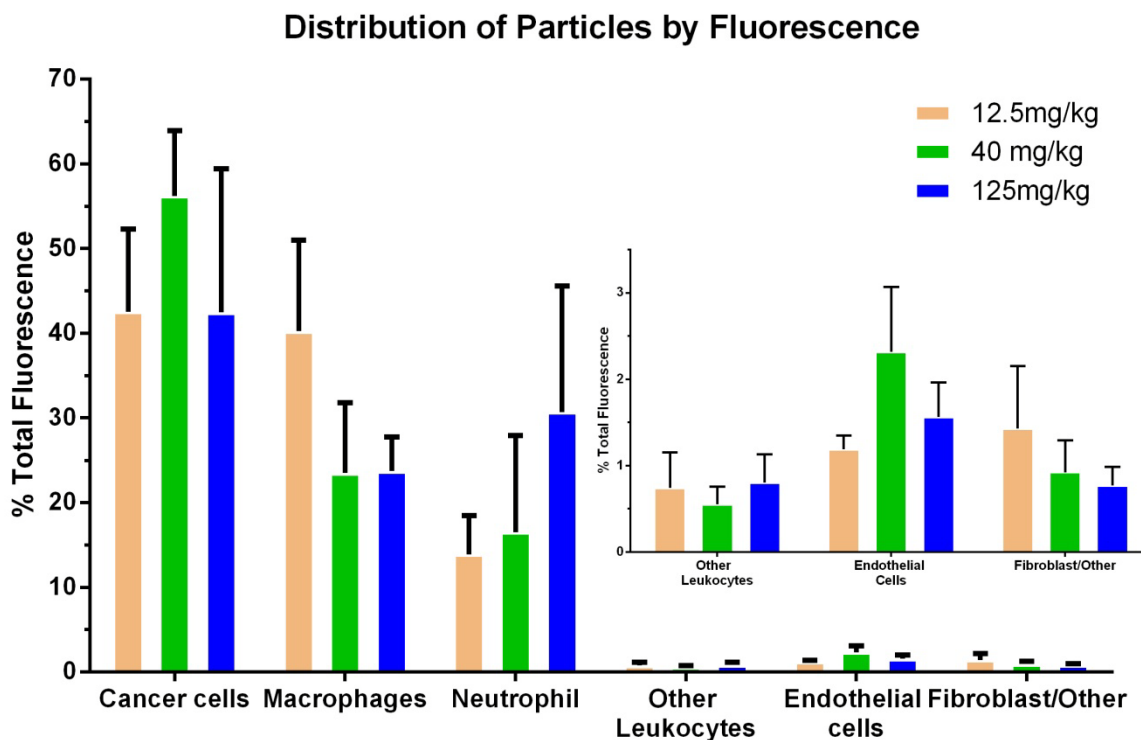


**Figure 3.7 Distribution of cell-associated particles as a function of particle dose**

Using the same dataset generated in Figure 3.5, the percentage of total fluorescence in each population relative to the whole sample is shown here. This gives a relative measure of the percent of cell-associated particles contained within each population. The error is  $\pm$ SD (N = 4 per dose).



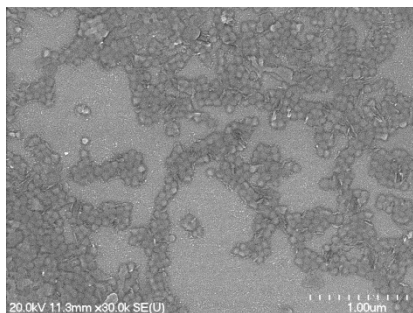


**Figure 3.8 SEM of 55x70nm particles**

SEM images were taken of the 55x70nm particles used in subsequent experiments.

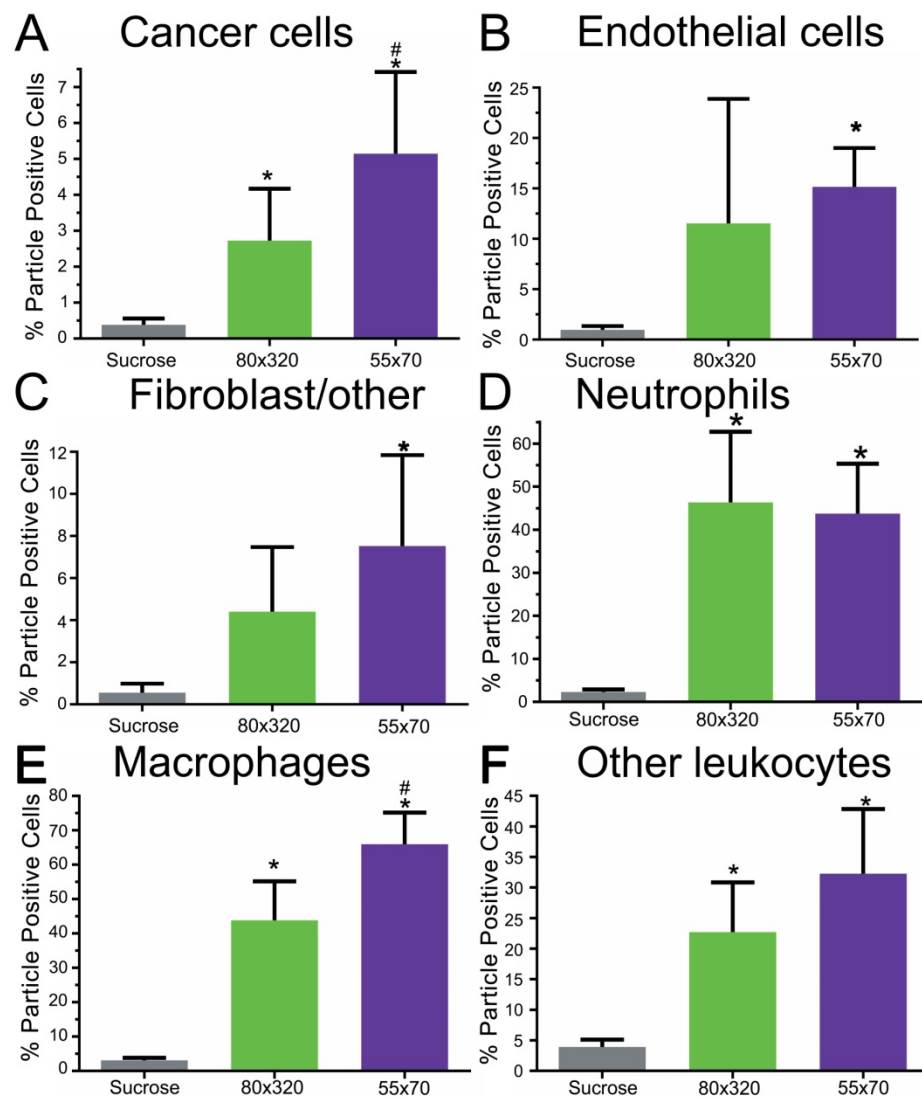


**Figure 3.9 Quantification of the particle association for differently sized particles**

Animals were administered either 80x320nm or 55x70nm particles. Gating and quantification of association was performed as shown in previous figures. Error shown is  $\pm$ SD (N=6 per group). The \* symbol represents  $p < 0.05$  vs Sucrose and # represents  $p < 0.05$  vs 80 x 320 nm particles.

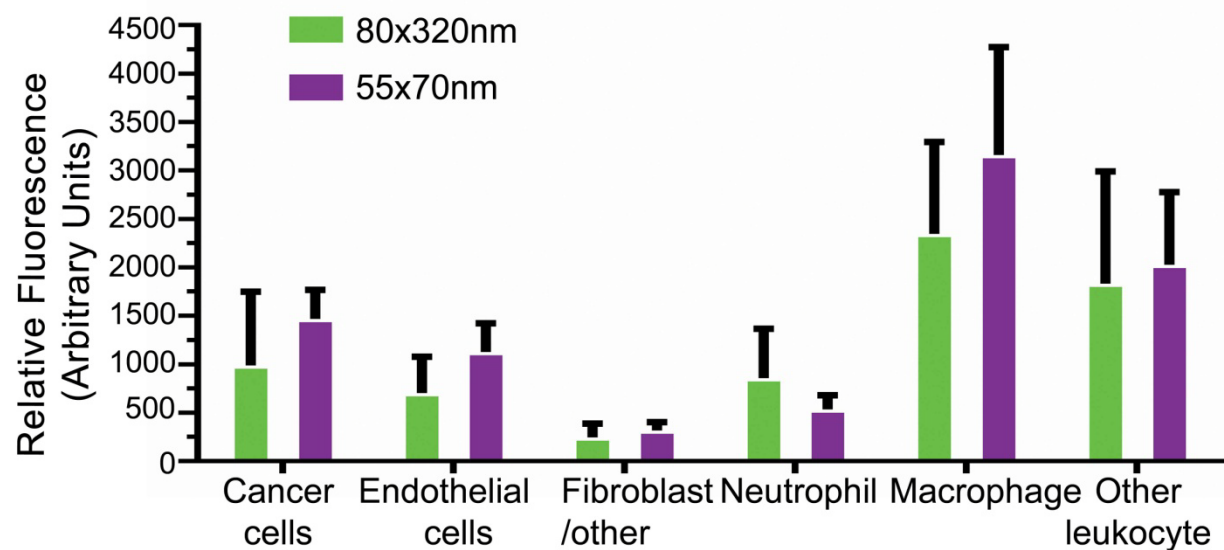


**Figure 3.10 Mean fluorescence intensity when administering differently sized particles**

Quantification of the mean fluorescence of the particle positive cells as determined in figure 3.9. Error shown is  $\pm$ SD (N=6 per group).

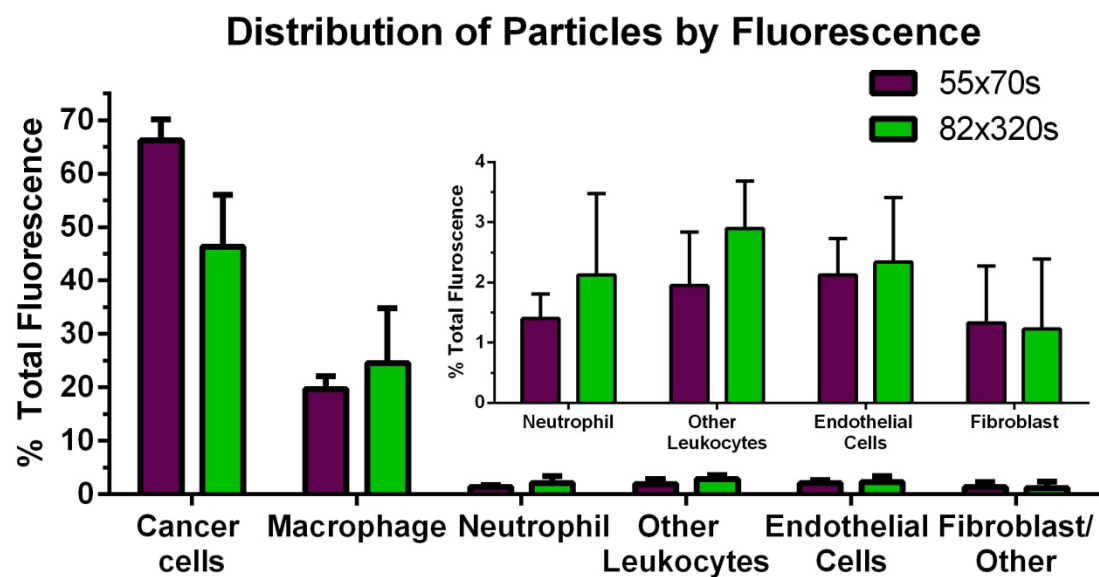


**Figure 3.11 Distribution of cell-associated particles as a function of particle size**

Using the same dataset generated in Figure 3.9, the percentage of cell-associated particles contained within each sub-population, as measured by fluorescence, as a function of particle size. Error shown is  $\pm$ SD (N=6).

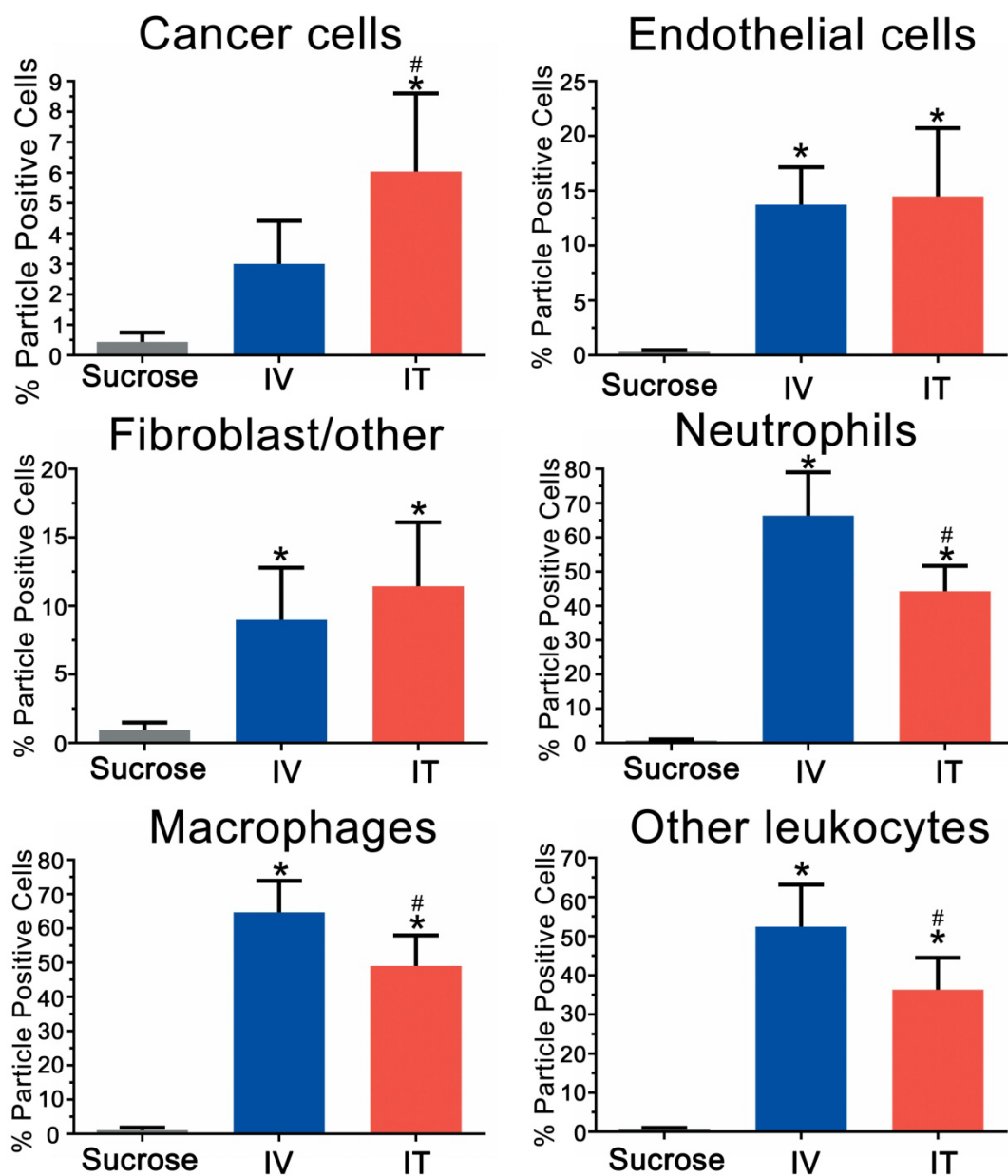


**Figure 3.12 Particle association as a function of route of administration**

Intravenous injection (blue bars) and intratumoral injection (red bars) was compared. The percent of particle association was calculated as previously stated. Error shown is  $\pm$ SD (N=6). The \* symbol represents  $p < 0.05$  vs Sucrose and # represents  $p < 0.05$  vs the IV dose.

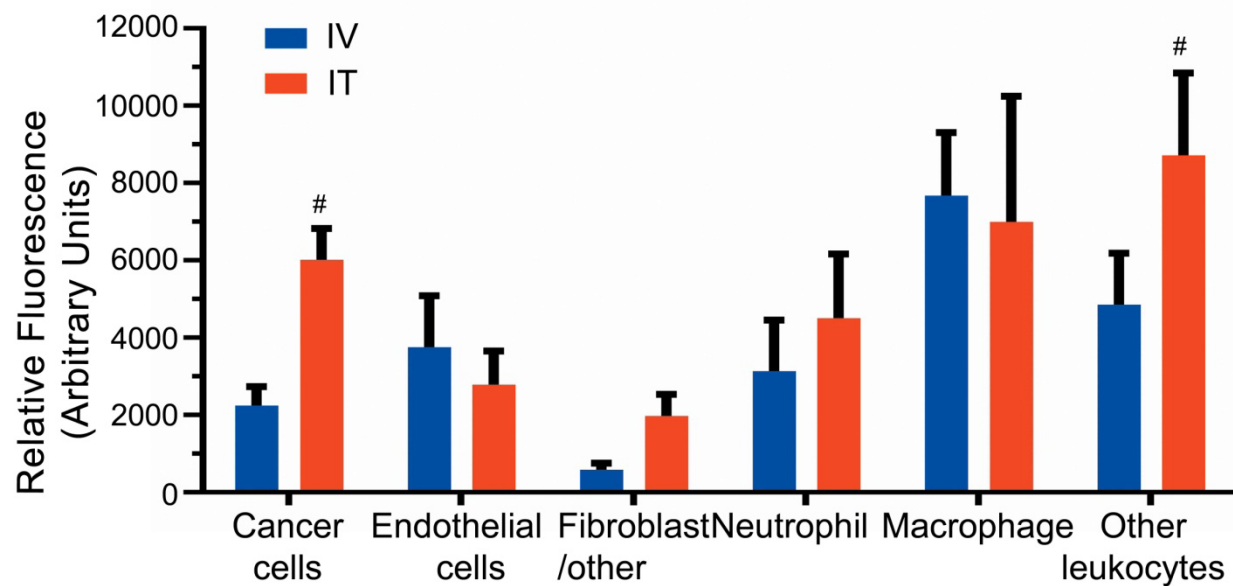


**Figure 3.13 Mean fluorescence in each sub-population as a function of route of administration**

The mean fluorescence of the particle-positive population was calculated as described previously. Error shown is  $\pm$ SD (N=6). The # represents  $p < 0.05$  vs the IV dose.

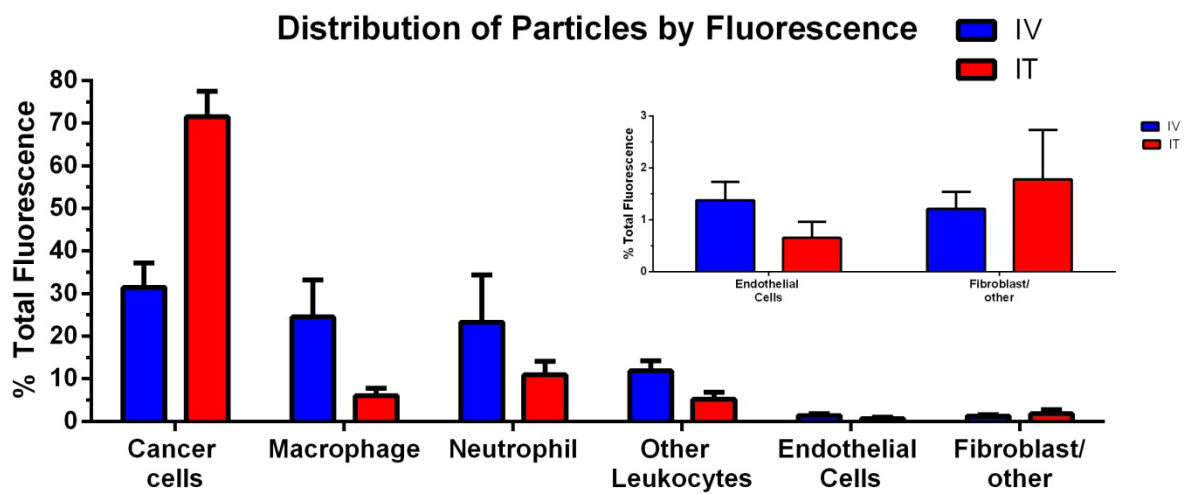


**Figure 3.14 Distribution of cell-associated particles as a function of route of administration**

Using the same dataset generated in 3.12, the percentage of cell-associated particles contained within each sub-population, as measured by fluorescence, as a function of route of administration. Error shown is  $\pm$ SD (N=6).

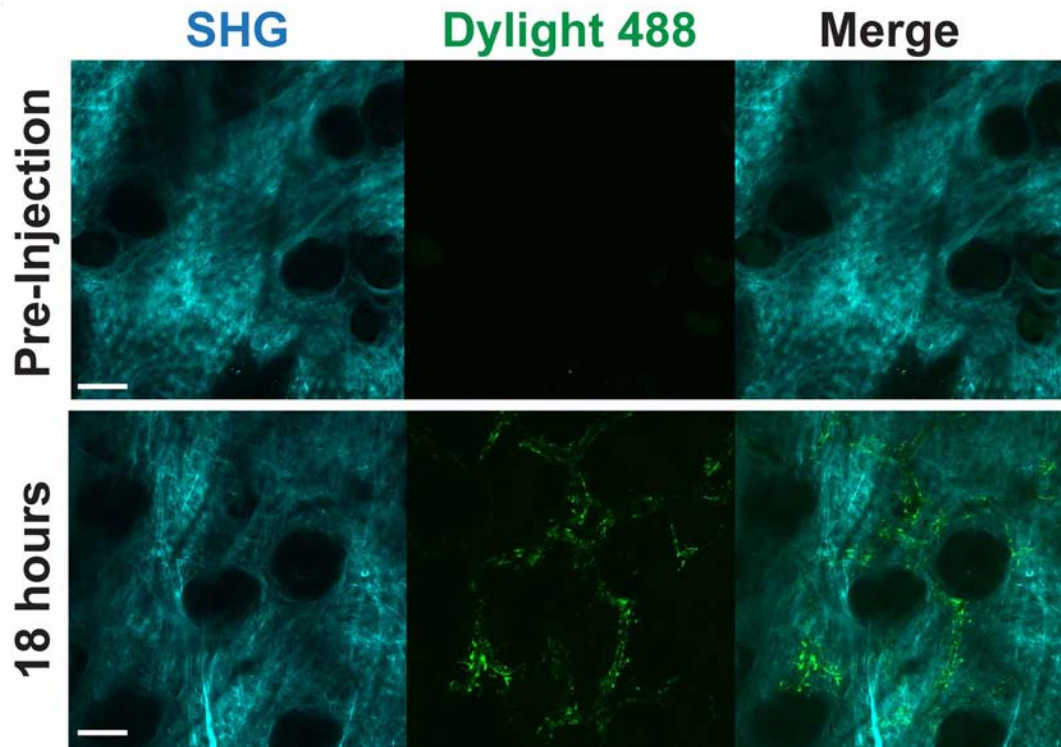


**Figure 3.15 Two photon imaging of normal mouse dermis**

Tumor-bearing nude mice were injected with 40mg/kg 80 x 320 nm particles. Images were taken before and 18 hours post-injection. Secondary harmonics show the collagen fibers with Dylight 488 representing the particle fluorescence. Images are from a 25x objective, with a maximum intensity projection image (all images in the z-stack are shown as a single 2D image), and scale bars representing 50 $\mu$ m.



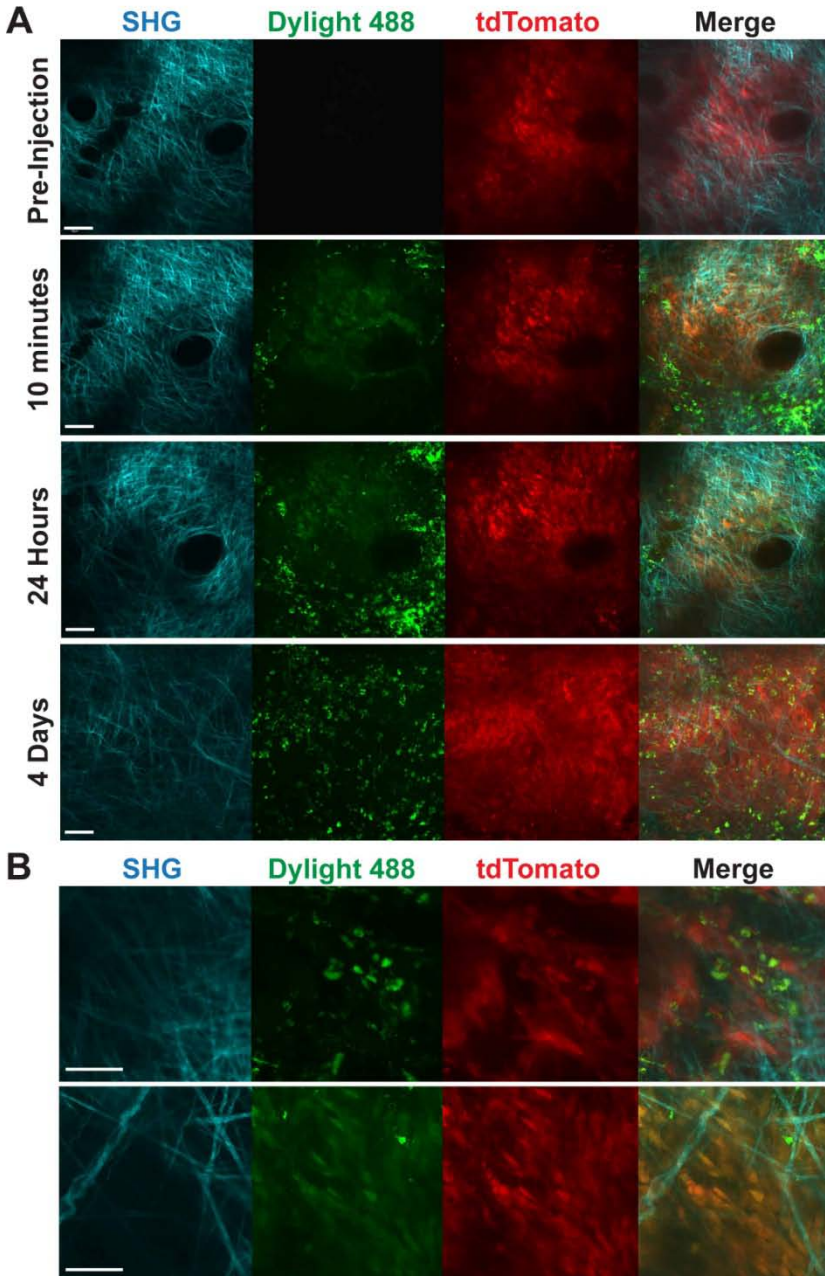


**Figure 3.16 Two photon imaging of tumors**

Secondary harmonics are the collagen fibers, Dylight 488 is particle fluorescence, and tdTomato is expressed by the cancer cells. A) Tumors were imaged before, and 10 minutes, 24 hours, and 4 days post injection. In B) at 24 hours, 3x zoomed in images of two separate fields of view (top, bottom) show particle colocalization with cancer and host cells. Images are collected using a 25x objective. The images shown are maximum intensity projection images where all images in a z-stack are shown as a single 2D

image, with a 3 $\mu$ m space between each slice. The scale bars represent 50 $\mu$ m. These are representative images from a small cohort (N = 2-3) animals using the same laser power and instrument settings between animals and time points.

### 3.7 REFERENCES

1. Matsumura Y, Maeda H, Smanes A. A New Concept for Macromolecular Therapeutics in Cancer Chemotherapy : Mechanism of Tumoritropic Accumulation of Proteins and the Antitumor Agent Smanes A New Concept for Macromolecular Therapeutics in Cancer Chemotherapy : Mechanism of Tumoritropic Accum. *Cancer Res.* 1986;46(12):6387–6392.
2. Poon Z, Lee JB, Morton SW, Hammond PT. Controlling in Vivo Stability and Biodistribution in Electrostatically. *Nano Lett.* 2011;11(5):2096–2103.
3. Liu Y, Tseng Y-C, Huang L. Biodistribution Studies of Nanoparticles Using Fluorescence Imaging: A Qualitative or Quantitative Method? *Pharm Res.* 2012;29(12):3273–3277.
4. Crayton SH, Elias DR, Al Zaki A, Cheng Z, Tsourkas A. ICP-MS analysis of lanthanide-doped nanoparticles as a non-radiative, multiplex approach to quantify biodistribution and blood clearance. *Biomaterials.* 2012;33(5):1509–19.
5. Van de Ven AL, Kim P, Haley O, et al. Rapid tumoritropic accumulation of systemically injected plateloid particles and their biodistribution. *J Control Release.* 2012;158(1):148–55.
6. Psimadas D, Georgoulas P, Valotassiou V, Loudos G. Molecular Nanomedicine Towards Cancer : *J Pharm Sci.* 2012;101(7):2271–2280.
7. Chu KS, Hasan W, Rawal S, et al. Plasma, tumor and tissue pharmacokinetics of Docetaxel delivered via nanoparticles of different sizes and shapes in mice bearing SKOV-3 human ovarian carcinoma xenograft. *Nanomedicine.* 2013;9(5):686–93.
8. Lo C-L, Chou M-H, Lu P-L, et al. The effect of PEG-5K grafting level and particle size on tumor accumulation and cellular uptake. *Int J Pharm.* 2013;456(2):424–431.
9. Ueno T, Dutta P, Keliher E, et al. Nanoparticle PET-CT detects rejection and immunomodulation in cardiac allografts. *Circ Cardiovasc Imaging.* 2013;6(4):568–73.
10. Clark DP, Ghaghada K, Moding EJ, Kirsch DG, Badea CT. In vivo characterization of tumor vasculature using iodine and gold nanoparticles and dual energy micro-CT. *Phys Med Biol.* 2013;58(6):1683–704.
11. Ernsting MJ, Murakami M, Roy A, Li S-D. Factors controlling the pharmacokinetics, biodistribution and intratumoral penetration of nanoparticles. *J Control Release.* 2013;172(3):782–794.
12. Ganesh S, Iyer AK, Gattacceca F, Morrissey D V, Amiji MM. In vivo biodistribution of siRNA and cisplatin administered using CD44-targeted hyaluronic acid nanoparticles. *J Control Release.* 2013;172(3):699–706.
13. Toita R, Nakao K, Mahara A, Yamaoka T, Akashi M. Biodistribution of vaccines comprised of hydrophobically-modified poly( $\gamma$ -glutamic acid) nanoparticles and antigen proteins using fluorescence imaging. *Bioorg Med Chem.* 2013;21(21):6608–15.

14. Movahedi K, Laoui D, Gysemans C, et al. Different tumor microenvironments contain functionally distinct subsets of macrophages derived from Ly6C(high) monocytes. *Cancer Res.* 2010;70(14):5728–39.
15. Li R, Hu H, Ma H, et al. The anti-tumor effect and increased tregs infiltration mediated by rAAV-SLC vector. *Mol Biol Rep.* 2013.
16. Zhao G, Rodriguez BL. Molecular targeting of liposomal nanoparticles to tumor microenvironment. *Int J Nanomedicine.* 2013;8:61–71.
17. Junttila MR, de Sauvage FJ. Influence of tumour micro-environment heterogeneity on therapeutic response. *Nature.* 2013;501(7467):346–54.
18. Xiao K, Li Y, Luo J, et al. The effect of surface charge on in vivo biodistribution of PEG-oligocholeic acid based micellar nanoparticles. *Biomaterials.* 2011;32(13):3435–46.
19. Almeida JPM, Lin AY, Langsner RJ, Eckels P, Foster AE, Drezek RA. In Vivo Immune Cell Distribution of Gold Nanoparticles in Naïve and Tumor Bearing Mice. *Small.* 2013:1–8.
20. Blank F, Stumbles PA, Seydoux E, et al. Size-Dependent Uptake of Particles by Pulmonary Antigen-Presenting Cell Populations and Trafficking to Regional Lymph Nodes. *Am J Respir Cell Mol Biol.* 2013;49(1):67–77.
21. Zheng M, Librizzi D, Kılıç A, et al. Enhancing in vivo circulation and siRNA delivery with biodegradable polyethylenimine-graft-polycaprolactone-block-poly(ethylene glycol) copolymers. *Biomaterials.* 2012;33(27):6551–8.
22. Manolova V, Flace A, Bauer M, Schwarz K, Saudan P, Bachmann MF. Nanoparticles target distinct dendritic cell populations according to their size. *Eur J Immunol.* 2008;38(5):1404–13.
23. Kourtis IC, Hirose S, de Titta A, et al. Peripherally administered nanoparticles target monocytic myeloid cells, secondary lymphoid organs and tumors in mice. *PLoS One.* 2013;8(4):e61646.
24. VanHandel M, Alizadeh D, Zhang L, et al. Selective uptake of multi-walled carbon nanotubes by tumor macrophages in a murine glioma model. *J Neuroimmunol.* 2009;208(1-2):3–9.
25. Kirpotin DB, Drummond DC, Shao Y, et al. Antibody targeting of long-circulating lipidic nanoparticles does not increase tumor localization but does increase internalization in animal models. *Cancer Res.* 2006;66(13):6732–40.
26. Guzmán J, Iglesias MT, Riande E, Compañ V, Andrio a. Synthesis and polymerization of acrylic monomers with hydrophilic long side groups. Oxygen transport through water swollen membranes prepared from these polymers. *Polymer (Guildf).* 1997;38(20):5227–5232.
27. Perry JL, Reuter KG, Kai MP, et al. PEGylated PRINT Nanoparticles: The Impact of PEG Density on Protein Binding, Macrophage Association, Biodistribution, and Pharmacokinetics. *Nano Lett.* 2012;12(10):5304–10.
28. Enlow EM, Luft JC, Napier ME, DeSimone JM. Potent engineered PLGA nanoparticles by virtue of exceptionally high chemotherapeutic loadings. *Nano Lett.* 2011;11(2):808–13.

29. Chan KT, Jones SW, Brighton HE, et al. Intravital imaging of a spheroid-based orthotopic model of melanoma in the mouse ear skin. *Intravital*. 2013;2(2):1–8.
30. Kume M, Carey PC, Gaehle G, et al. A semi-automated system for the routine production of copper-64. *Appl Radiat Isot*. 2012;70(8):1803–6.
31. Chu KS, Schorzman AN, Finniss MC, et al. Nanoparticle drug loading as a design parameter to improve docetaxel pharmacokinetics and efficacy. *Biomaterials*. 2013;34(33):8424–9.

## CHAPTER IV: CONCLUSIONS AND FUTURE DIRECTIONS

In the present collection of studies, we sought to elucidate the cellular distribution of 80 x 320 nm PRINT hydrogel particles within the tumor itself. These data show that certain cell types such as macrophages preferentially associate with more particles than all other cell types and contain the highest percentage of particle-positive cells. In contrast, cancer cells represent 90% of all cells within the tumor and have a small fraction of cells associating with particles. Though only a small fraction of cancer cells are particle-positive cancer cells are the large majority of particle-positive cells. Moreover, dose-dependent association is seen at lower doses of particles (12.5, 40 mg/kg), but at higher doses (125mg/kg) the association shows a dose-independent plateau. Coincidentally, the amount of particles in each particle-positive macrophage increases dramatically. This suggests that as the cancer cells become saturated in their ability to associate with particles, macrophages increasingly become a sink for particles.

Radioactive studies of the whole organ suggest that at these three doses, particle accumulation of the tumor stays constant at around 1% of the injected dose. This demonstrates that accumulation in the organ is linear. Contrasted with the flow cytometry data, it suggests that the particles are accumulating in non-cell compartments such as the extracellular matrix.

These data also reveal that smaller particle size enhances the cancer cell association two-fold. Whether this is due to the physical ability of the particles to diffuse to other cells or a greater ability of the cells to associate with the particles is unclear. Route of administration also seemed to play a significant role in particle cell association. Injection of particles intratumorally increased cancer cell association and decreased macrophage, neutrophil, and other leukocyte association. Moreover, the cancer cells association with particles from the intratumorally injected animals showed a 2-3 fold increase in the mean fluorescence intensity, suggesting that the particles per cell was greatly enhanced. This experiment suggests that there is some sort of physical barrier such as diffusion between cells or the porosity of the blood vessels that is preventing 80 x 320 nm particles from reaching the maximum potential association.

Several questions arise from this research. What percentage of the detected macrophages within the tumor are monocytes that have associated with a particle while in blood and come to the tumor to differentiate? This is an intriguing question as it may lend credence to the hypothesis that macrophages are trafficking particles to the tumor as opposed to particles accumulating there as posited by the EPR effect. A similar type of effect has been seen with the blood-brain barrier[1,2]. The addition of multi-color flow cytometry to this set of experiments could begin to answer fundamental questions about the trafficking of nanoparticles to specific sites, be it brain or tumor. Specifically, by fluorescently labeling the macrophages or using GFP-expressing macrophages, and incubating with fluorescently labeled nanoparticles (fluorophore A), this would allow for determination of not only whether those nanoparticles are being delivered to cells, but also a rough estimation of just how much of the nanoparticles are left in the macrophages itself as it would be possible to run a sample of the loaded macrophages when analyzing the experimental samples. Moreover, using the labeled/GFP-expressing macrophages would also quantify of the fraction of macrophages present in the tissue that are the injected/labeled ones, providing information on the effectiveness of your delivery strategy. Additionally, should any other cells in the body take up those fluorescently labeled particles, it would suggest that the macrophages are either making physical contact or ejecting the nanoparticles from the cell, indicating successful delivery of the nanoparticles.

Furthermore, if one were to intravenously inject a second, differently fluorescently labeled nanoparticle (fluorophore B), one could compare the ratio of the fluorophore A to fluorophore B and determine the efficiency of intravenously injected nanoparticles as compared with macrophage-delivered particles.

Additional questions include what effect does particle number have on cell association? Would greater numbers of smaller particles be better for delivery than lesser amounts of larger particles? This is a highly difficult question to discern as any changes in particle numbers is confounded by particle size or physical amounts. And given downstream applications would be focused on efficacy and treatment, this leads to fundamental questions about particle-mediated delivery. Would it be better to deliver more, smaller amounts of cargo contained in particles or minimal, large amounts of cargo contained in large

particles? These questions directly impact nanoparticle efficacy and pharmacokinetics, which can be directly related to nanoparticle drug loading and dosing schedule[3,4]

One intriguing question strikes at the heart of flow cytometry assays using nanoparticles: what particle fluorescence is needed to discriminate between the cell that is without particles and the cell that contains a single particle? i.e. what's the signal to noise or how many particles does it take to be considered particle-positive? Clearly in this data, the particle fluorescence is unable to discriminate to such an extent, but would play a large influence in accurate quantitation of the amount of association.

Obviously, there is still much work to be done. I have only used one type of enzymatic method in order to dissociate my tumors. There are a variety of enzymatic and physical methods with which to accomplish the same task. It may be interesting to compare and contrast the resulting cell populations and association as a function of the method used.

There are many other factors of particles not included in these studies which would be of interest and benefit. A basic particle characteristic like shape may reveal interesting observations. Certainly Mitragotri and other others have shown shape to impact the clearance and circulation time of particles[5-12], however, specific and controlled insight into how that may affect delivery and interact with cells is less well understood. Other characteristics like charge, composition, or a broader range of sizes may also reveal important biological insights, particularly size. In comparing size it is important to note the role that the inherent brightness of the particle will play in detection of the particles by fluorescence. It is common to dope the particle by wt% and for different sizes, this gives a different physical amount of fluorophore per particle. More careful analysis of this parameter may be required to cleanly test nanoparticle hypothesis comparing size using fluorescence. Though it would be difficult to control for particle brightness, for a given size, determining the dose at which cell association reaches a maximum and whether that maximum changes in comparison to other sizes may give particular fundamental biological insight into tumor pore size and diffusability of the particles. This kind of sub-organ cellular analysis may also help elucidate whether the prevailing hypothesis about targeted particles is correct. The prevailing wisdom is that targeted particles only assist in having cells endocytose particles as opposed to accumulating within the organ. Flow cytometry would be able to more directly answer this question in vivo. In addition, if something fluorescent and detectable by another sensitive method (i.e. quantum dot



loaded particles or fluorophore + drug loaded particles) were used, it may be possible to flow sort the particle-positive cells from each cell type and then directly quantify the amount of particle per cell using the cargo as a surrogate measure. Though it would be nearly impossible to calculate a percent injected dose due to not knowing the maximal number of cells in a tumor, this method would allow for a direct quantitative comparison of amount of particles per cell. Alternatively, if the particles were large enough, it would be possible to simply run a volume of particles directly on the flow cytometry and quantify the average fluorescence. In this way, a particle number and average fluorescence could be determined with mass being constant. The DeSimone lab has had difficulty analyzing individual 80 x 320 nm particles on a flow cytometry (data not shown), but it may be possible for larger particles. The less attractive alternative would be flow sort and calculate the amount of particles per cell using a standard curve of particles spiked into cells from an uninjected animal. This approach may be labor-intensive, but would be the only way to determine how much particles were contained in each cell for smaller, unloaded particles.

It may also be beneficial to extend all this approach to other models, especially to answer more fundamental questions about the EPR effect and nanoparticle delivery. One experiment that was conducted was to examine what the effect of circulation time on particle association would be. Circulation time is presumed to influence the EPR effect and thereby accumulation within tumors. Liposomal encapsulated Clodronate (Clodrosome<sup>TM</sup>) has been previously found to selectively kill circulating macrophages, thereby creating long-circulating nanoparticles[13-16]. For this experiment, Clodronate was injected into the peritoneum daily for three days before administering particles. Interestingly, when Clodrosome<sup>TM</sup> was administered, the percentage of cells associating with particles decreased (data not shown). The most likely explanation is that the cancer cells that normally take up particles also took up the Clodrosome<sup>TM</sup> and subsequently died. Optimization of a dosing protocol may allow this experiment to be successful. Alternatively, dosing anti-monocyte antibodies or siRNA targeted natural uptake receptors present on their surface, though expensive, may also help answer this question.

Cellular level analysis may be beneficial to understanding where and how to best control the application of nanomedicine for the treatment of solid tumors. Our data show a distinct profile of the distribution of particles within an organ. It is hoped that these data will provide a basic understanding that will enhance delivery of therapeutic-loaded particles to obtain a therapeutic effect. Furthermore, this

approach can serve as a template for a standard type of analysis performed by other nanomedicine scientists. One day, regular clinical use of nanomedicines may be standard practice, but ensuring a solid grasp of the fundamentals will be key.

#### 4.1 REFERENCES

1. Klyachko NL, Haney MJ, Zhao Y, Manickam DS, Mahajan V, et al. (2013) Macrophages offer a paradigm switch for CNS delivery of therapeutic proteins. *Nanomedicine (Lond)*.
2. Haney MJ, Zhao Y, Harrison EB, Mahajan V, Ahmed S, et al. (2013) Specific transfection of inflamed brain by macrophages: a new therapeutic strategy for neurodegenerative diseases. *PLoS ONE* 8: e61852.
3. Gharpure KM, Chu KS, Bowerman CJ, Miyake T, Pradeep S, et al. (2014) Metronomic Docetaxel in PRINT Nanoparticles and EZH2 Silencing Have Synergistic Antitumor Effect in Ovarian Cancer. *Mol Cancer Ther* 13: 1750-1757.
4. Chu KS, Schorzman AN, Finniss MC, Bowerman CJ, Peng L, et al. (2013) Nanoparticle drug loading as a design parameter to improve docetaxel pharmacokinetics and efficacy. *Biomaterials* 34: 8424-8429.
5. Pino CJ, Gutterman JU, Vonwil D, Mitragotri S, Shastri VP (2012) Glycosylation facilitates transdermal transport of macromolecules. *Proc Natl Acad Sci U S A* 109: 21283-21288.
6. Yoo JW, Doshi N, Mitragotri S (2010) Endocytosis and Intracellular Distribution of PLGA Particles in Endothelial Cells: Effect of Particle Geometry. *Macromol Rapid Commun* 31: 142-148.
7. Yoo JW, Chambers E, Mitragotri S (2010) Factors that control the circulation time of nanoparticles in blood: challenges, solutions and future prospects. *Curr Pharm Des* 16: 2298-2307.
8. Kolhar P, Anselmo AC, Gupta V, Pant K, Prabhakarapandian B, et al. (2013) Using shape effects to target antibody-coated nanoparticles to lung and brain endothelium. *Proc Natl Acad Sci U S A* 110: 10753-10758.
9. Barua S, Yoo JW, Kolhar P, Wakankar A, Gokarn YR, et al. (2013) Particle shape enhances specificity of antibody-displaying nanoparticles. *Proc Natl Acad Sci U S A* 110: 3270-3275.
10. Rodriguez PL, Harada T, Christian DA, Pantano DA, Tsai RK, et al. (2013) Minimal "Self" peptides that inhibit phagocytic clearance and enhance delivery of nanoparticles. *Science* 339: 971-975.
11. Loverde SM, Klein ML, Discher DE (2012) Nanoparticle shape improves delivery: rational coarse grain molecular dynamics (rCG-MD) of taxol in worm-like PEG-PCL micelles. *Adv Mater* 24: 3823-3830.
12. Jones SW, Roberts RA, Robbins GR, Perry JL, Kai MP, et al. (2013) Nanoparticle clearance is governed by Th1/Th2 immunity and strain background. *Journal of Clinical Investigation* 123: 3061-3073.

13. Yamamoto T, Naito M, Moriyama H, Umezu H, Matsuo H, et al. (1996) Repopulation of murine Kupffer cells after intravenous administration of liposome-encapsulated dichloromethylene diphosphonate. *Am J Pathol* 149: 1271-1286.
14. Naito M, Nagai H, Kawano S, Umezu H, Zhu H, et al. (1996) Liposome-encapsulated dichloromethylene diphosphonate induces macrophage apoptosis in vivo and in vitro. *J Leukoc Biol* 60: 337-344.
15. Simberg D, Duza T, Park JH, Essler M, Pilch J, et al. (2007) Biomimetic amplification of nanoparticle homing to tumors. *Proc Natl Acad Sci U S A* 104: 932-936.
16. Simberg D, Park JH, Karmali PP, Zhang WM, Merkulov S, et al. (2009) Differential proteomics analysis of the surface heterogeneity of dextran iron oxide nanoparticles and the implications for their in vivo clearance. *Biomaterials* 30: 3926-3933.